STRUCTURED RANDOM LIGHT

by

Xiaofei Li

Submitted in partial fulfillment of the requirements
for the degree of Doctor of Philosophy

at

Dalhousie University
Halifax, Nova Scotia
August 2024

© Copyright by Xiaofei Li, 2024

Table of Contents

List of Figures . . . . . **iv**

Abstract . . . . . **viii**

List of Abbreviations . . . . . **ix**

Acknowledgements . . . . . **xi**

Chapter 1 Introduction **1**

1.1 Overview 1

1.2 Thesis Motivations and Objectives 9

1.3 Thesis Outline 10

Chapter 2 Deep learning and random light structuring ensure robust free-space communications **13**

2.1 Introduction 13

2.2 Image transmission employing source correlation structure 16

2.3 Image transmission utilizing source coherence radius 23

2.4 Conclusion 26

2.5 Acknowledgement 27

Chapter 3 Perfect correlation vortices **28**

3.1 Introduction 28

3.2 Theory and numerical simulations 29

3.3 Conclusion 37

3.4 Acknowledgement 37

Chapter 4 Multi-function vortex array radar **38**

4.1 Introduction 38

4.2 Imaging and positioning process for 2D target 40

4.3 Topography profiling process 46
4.4 Conclusion 48
4.5 Acknowledgement 48

Chapter 5 Prime number factorization with light beams carrying orbital angular momentum 49

5.1 Introduction 49
5.2 Theory and simulation analysis 51
5.3 Experimental implementation 53
5.4 Conclusion 57
5.5 Acknowledgement 58

Chapter 6 Conclusion 60

6.1 Discussion and Conclusion Remarks 60
6.2 Future work 62

Appendix 64

Appendix A Deep learning and random light structuring ensure robust free-space communications 64
Appendix B Derivation of PCV evolution in free space 70
Appendix C Copyright Permissions 72

Bibliography 75

List of Figures

2.1 Schematics of our encoding/decoding protocol with LG correlated beams. 17

2.2 Decoding process and the architecture of ResNet 34 classifier. 18

2.3 Experimental verification of our protocol. (a) Experimental setup. NDF: neutral density filter; L: thin lens; RGGD: rotating ground glass disk; GAF: Gaussian amplitude filter; SLM: spatial light modulator; RM: reflected mirror; and CCD: charge coupled device. (b) Qualitative juxtaposition of transmitted and received images. (c) Quantitative measure of the state detection fidelity as a conditional probability $P_{s_r|s_t}$ of finding a transmitted state s_t in state s_r , where $s_r(s_t)$ is represented in the quaternary basis (0, 1, 2, 3). 20

2.4 Recorded intensity profiles of LG-correlated versus fully coherent LG beams transmitted through either a single or two optical diffusers. 21

2.5 Schematics of the image transfer protocol employing the source coherence radius for information encoding. (a) Illustrating control of the transverse coherence radius of the source with a focusing hologram. (b) The image transmission protocol involving the spatial coherence radius DoF. 23

2.6 Schematics of the image transfer protocol employing an array of LG-correlated beams. (a) Schematic representation of the array generation. (b) The position of each intensity pattern in a 2×2 array. (c) The encoding/decoding sequence of 256 grey levels and 256 array states. 25

2.7 Qualitative (visual) and quantitative (fidelity) comparison between transmitted and received images. The color bar shows normalized fidelity with unity corresponding to 100%. 26

3.1 Intensity distribution (a) and its evolution on free space propagation (b) for PCVs of variable TC m. The parameters of the source are $w_0 = 10$ cm, $\sigma_c = 1$ mm, and $\lambda_0 = 532$ nm. 30

3.2 Evolution of the magnitude and phase (hue) of the DOC of a PCV, given by Eq. (3.14), with the propagation distance. The source parameters are $w_0 = 10$ cm, $\sigma_c = 1$ mm, $r_0 = 2$ cm, and $\lambda_0 = 532$ nm. 33

3.3 Comparing the magnitude of DOC evolution obtained from the exact expression, Eq. (3.14) and the corresponding Gaussian approximation, Eq. (3.15) with z over a kilometer-long stretch of free space. The source parameters are $w_0 = 10$ cm, $\sigma_c = 1$ mm, $r_0 = 2$ cm, and $\lambda_0 = 532$ nm. 34

3.4 Comparison of the widths of an ideal PCV ring δ with that determined from the rms width of the exact DOC profile Δ_m. Left: Δ_m and δ as functions of m at $z = 500$ m. Right: δ and Δ_m as functions of the propagation distance z for $m = 5$. . . 35

3.5 Evolution of the magnitude of PCV DOC through a 150 m long stretch of the turbulence atmosphere with the structure constant C_n, $C_n^2 = 10^{-13}$ m$^{-2/3}$. The source parameters are $w_0 = 10$ cm, $\sigma_c = 1$ mm, and $\lambda_0 = 532$ nm. The reference point corresponds to $r_0 = 2$ cm and $\phi_0 = 0$. 36

4.1 Concept (a) and protocol schematics (b) of vortex MFR. . . . 40

4.2 Geometry of the vortex array (a) and recovered images (b). . 41

4.3 Target acquisition of the proposed vortex MFR (a) with variable azimuth (b) and relative radial position of the array and target centers (b). 43

4.4 Recovered image and the corresponding transverse power flow distributions for a variable azimuth. 44

4.5 Recovered images and the corresponding transverse power flow distributions for a variable array-target separation distance 9.5 m, 12.7 m, 16.2 m in directions corresponding to the angles 0 (a)-(c) and $2\pi/3$ (d)-(f). Power curves versus the separation distance r for azimuthal directions 0 (g) and $2\pi/3$ (h), respectively. 45

4.6 3D and 2D views of the schematics of the terrain profiling process. 47

5.1 Schematic illustration of the principle of prime number factorization with OAM beams. (a) The phase distribution of an OAM beam twisted as a spiral staircase during propagation exhibits azimuthal periodicity with the period $\varphi_T = 2\pi/l$. (b) Prime number sieve examples marked with color dots. (c) Implementing prime number factorization with OAM beams. Hue and brightness of plots in (a) and (b) refer to the phase and intensity, respectively. 51

5.2 Numerical simulation of prime number factorization with the OAM beam with l=1×53 (a), l=2×3×5×7 (b) and l=17×19 (c). The blue squares (red dots) mark theoretical results obtained from the incomplete Gauss sum (simulation results obtained with the aid of Matlab). 54

5.3 Experimental setup for prime number factorization with OAM beams. DPSS, Diode-Pumped Solid-State laser; HP, half-wave plate; BE, beam expander; SLM, reflective phase-only liquid crystal spatial light modulator; DMD, Digital Micromirror Device. (a) Computer-generated hologram of a Laguerre-Gauss beam with topological charge l=30 and $w_0 = 0.8$ mm. (b) Complex amplitude of an experimentally reproduced Laguerre-Gaussian beam at the front surface of the DMD. The image size is 9.6 mm ×9.6 mm, and hue and brightness refer to the phase and intensity, respectively. (c) An example mask of prime number sieve T_p with M=7, $d = 0.15$ mm and $r_0 = 3$ mm. . . 55

5.4 Numerical (a) and experimental (b) results for the normalized intensity patterns of an OAM beam modulated by prime number sieves. The topological charge is $l = 30$ and the trial factor p is given by 4, 5, 10 from left to right. The size of each pattern is 375μm×375μm, and the optical axis is labelled by the cross symbol. 56

5.5 Experimental implementation of prime number factorization with OAM beams. The number to be factorized is given by $l = 30$ (a) and $l = 53$(b). The vertical lengths of error bars characterize an absolute value of the difference between the experimental and simulation results. 57

5.6 (a) Fluctuating and ensemble average phases of the field of a noisy OAM beam. (b) Time evolution of two phases at the same locations within the phase distribution marked by the purple dots (p_1 and p_2) in (a). The radius of the purple dashed circles in (a) corresponds to the coherence width of the beam. 58

6.1 Residual building block diagram of ResNet 34 with n representing a number of convolution kernels. 64

6.2 Experimental setup of grey image (a) transmitting in atmospheric turbulence and (b) suffering obstructing particles. OD: optical diffuser; SSOO: sector-shaped opaque obstacle, others are same with Fig. 2.3. 66

6.3 Recorded intensity profiles of LG-correlated versus fully coherent LG beams obstructed by a sector-shape obstacle situated in the beam path. 67

6.4 Normalized intensity of an LG-correlated beam (LG_{04}) at the receiver generated by a source of variable coherence radius. . 67

6.5 Confusion matrix and transmission fidelity of an illustrative example. 68

6.6 Qualitative (visual) and quantitative (fidelity) comparison between transmitted and received images. (a), & (b) correspond to the protocol utilizing the source correlation structure, while (c) corresponds to that using the source coherence length for image encoding. The color bar shows normalized fidelity with unity corresponding to 100%. 69

Abstract

In the quest to enhance the capacity and quality of information networks, structured random light has emerged as a promising option. The study of the structured random light and its application in advancing new-generation information networks is reported. First, we establish a robust high-capacity communication system for information transport using structured random light and deep learning algorithm. Second, to enhance the transmission distance in above structured random light communication links, we introduce "perfect" correlation vortices which can maintain their structure even during slow diffraction in free space and remain stable in strong atmospheric turbulence. Third, we propose a multi-function radar incorporating the vortex structure. It effectively manages limited resources to acquire a large amount of information and possesses a high level of versatility to accomplish multiple functions. Finally, we reveal the connection between statistical optics and number theory, which can be utilized for information storage and bolster information security.

List of Abbreviations

AI	Artificial intelligence
AM	Amplitude modulation
BE	Beam expander
CCD	Charge coupled device
CNN	Convolutional neural network
CSD	Cross-spectral density
DAD	Dark or antidark
DMD	Digital micro-mirror device
DOC	Degree of coherence
DoF	Degree of freedom
FSO	Free-space optical
GAF	Gaussian amplitude filter
GSM	Gaussian Schell-model
HP	Half-wave plate
IIoT	Industrial internet of things
LG	Laguerre-Gaussian
MFR	Multi-function radar
NDF	Neutral density filter
NFC	Near field communications
OAM	Orbital angular momentum
OD	Optical diffuser
OV	Optical vortices
PCV	Perfect correlation vortices
PDM	Polarization division multiplexing
QPM	Quadrature phase modulation
QPSK	Quadrature phase shift keying
ReLU	Rectied linear unit activation function
ResNet	Residual network

RGGD	Rotating ground glass disk
RM	Reflected mirror
SDM	Space division multiplexing
SLM	Spatial light modulator
SNR	Signal-to-noise ratio
SSOO	Sector-shaped opaque obstacle
TC	Topological charge
WDM	Wavelength division multiplexing
2D	2-dimensional
3D	3-dimensional

Acknowledgements

I would like to express my heartfelt appreciation to my supervisor, Dr. Sergey A. Ponomarenko, for his invaluable guidance, unwavering support, and insightful feedback throughout the entire process of researching my project and writing this thesis.

I would like to express my sincere gratitude to my co-supervisor, Dr. Yangjian Cai, and committee members Dr. Yuan Ma and Dr. Zhanghua Han, for their expertise, guidance, and encouragement throughout the research and writing of this thesis.

I am also grateful to Electrical and Computer Engineering Department at Dalhousie University for providing the necessary resources and environment conducive to research.

Furthermore, I extend my appreciation to all goup members who have assisted and supported me during this thesis journey.

Special thanks are extended to my family and friends for their patience, understanding, and encouragement during this journey.

Lastly, I extend my appreciation to all individuals who contributed in any form to the completion of this thesis.

Chapter 1

Introduction

1.1 Overview

Nowadays, the rapid pace of innovations in information transfer and related emerging applications causes unprecedented growth in data traffic, which results in great demand for efficient information networks. The latter refer to systems of interconnected devices that facilitate the exchange and dissemination of information. These networks play a fundamental role in the modern society where people have the opportunity to connect with each other anytime and anywhere with high-quality and high-capacity data transfer, all while ensuring robust information security [1, 2, 3]. These demands trigger ever increasing interest in optical techniques because of their wider bandwidth compared to the radio frequency technology [4]. The integration of optical technology with a new-generation information technology not only brings more innovation and possibilities to information networks but also expands the application scenarios of optical technology, particularly for information acquisition and transport.

One of the widely used and important optical technologies for information acquisition is a laser radar (Radio Detection and Ranging) technology [5]. According to their purposes and applications, laser radars can be classified into several main types: indoor radars, outdoor radars, and biometric radars [6]. The indoor radars are mainly used for indoor environment monitoring, distance measurement, and positioning. They are typically designed with smaller size and low power consumption in mind to adapt to indoor space limitations and low power requirements [7, 8, 9]. The outdoor radars are employed for monitoring, tracking, navigation, and detection in outdoor environments, which include automotive systems, airspace surveillance, and weather forecasting [10, 11, 12, 13]. Biometric radars can be implanted into living organisms to detect their health status, facilitate medical diagnosis and realize wildlife tracking[14, 15, 16].

Optical information transport is accomplished by a communication process. An

optical communication is a form of communication that uses light as a carrier for information transmission. Specifically, depending on different application scenarios, optical communications can be divided into fiber optical communications, underwater communications, short-range wireless communications, and free-space optical (FSO) communications. In fiber optical communications, optical fibers are employed as the transmission medium to carry out end-to-end information transfer, which is currently the main means for inter-city communications [17]. Underwater communications primarily involve deploying sensors on the seabed to monitor and transmit underwater information to prevent disasters [18]. Short-range wireless communication applications include local and industrial communications like Bluetooth, Wi-Fi, NFC (near-field communications), on-chip communications, and IIoT (industrial internet of things), where high-density fiber deployment is not feasible, yet high-speed information exchange remains imperative [19]. FSO communications are the designation for optical wireless techniques that utilize wavelengths in the range of 1300 nm-1600 nm. In FSO communications, light is utilized as the information carrier to transmit data accurately and securely through free space between different stations [20]. Today, FSO communications can achieve transmission distances on a kilometer scale. They attract attention across various industries because they provide an excellent solution in situations where the cost of installing fiber or the harsh installation environment makes fiber optic communications ill-advised [20, 21].

Notably, information security cannot be overlooked throughout the above applications. Efficient information networks rely heavily on robust information security measures to safeguard data integrity, confidentiality, and availability. Cryptography provides safety mechanisms to securely transfer and store the acquired informtion, ensuring that only authorized recipients can access and manage it. Deployed encryption measures can be classified into two categories: conventional encryption and lightweight encryption [22]. Conventional encryption is well-established and widely used to address potential threats involving eavesdropping, data breaches, and denial-of-service attacks [23]. However, it is only suitable for high-security and high-resource scenarios and does not adapt well to constrained application scenarios, such as embedded systems and sensor networks. Lightweight encryption fills the gap in scenarios with restricted computational power and resources, involving constrained physical

size, processing requirements, and memory limitations [22]. Both categories are based on highly complex mathematical problems. As computing power increases, solving these mathematical problems becomes easier, bringing severe challenges to these encryption techniques. Subsequently, quantum encryption, as a powerful remedial technology, is developed to address these challenges [24]. Quantum encryption utilizes quantum states as information carriers for transmitting data [25]. Due to its reliance on quantum properties, quantum encryption offers a high level of security, ensuring robust security throughout the optical communication process [26].

These advancements originate from the solid theoretical foundation of structured light. Structured light refers to optical fields with a multitude of controlled degrees of freedom (DoFs), including amplitude, phase, polarization, frequency, space and time [27]. With the increasing demand for high-capacity information networks, structured light offers a promising solution. Multiplexing the light field structure with numerous DoFs boosts the capacity of various kinds of information networks, catering to operations for high-capacity data. In order to effectively acquire and transmit large-capacity data, various technologies for encoding, multiplexing, and modulation are typically used [28, 29, 30], such as amplitude encoding [31], polarization encoding [32], space division multiplexing (SDM) [33], polarization division multiplexing (PDM) [34], wavelength division multiplexing (WDM) [35], amplitude modulation (AM) [36], quadrature phase modulation (QPM) [37], and quadrature phase shift keying (QPSK) [38].

One successful case of structured light providing premium service in high-capacity information networks is the utilization of a helical phase structure $exp(il\phi)$, linked with the orbital angular momentum (OAM) of $l\hbar$ per photon. The radar system using OAM-modulated signals can collect a great amount of information about targets [39, 40]. Vortex-multiplexed and -encoded communication networks can significantly enhance data transmission capacity without resorting to additional bandwidth usage [41, 42, 43]. Simultaneously, the security of these advanced networks is supported by OAM-based encryption approaches [44, 45], which leverage mathematical foundations of prime decomposition in number theory. Prime decomposition involves factorizing a composite number into its prime factors, which is essential for developing secure encryption mechanisms [46]. Various approaches have been proposed to realize

efficient prime number decomposition, including quantum algorithms [47], variational algorithms [48], and classical protocols involving Gauss sums [49, 50, 51, 52, 53]. Consequently, applying efficient prime factorization algorithms helps secure data integrity and availability of OAM-based high-capacity information networks.

Although improving data capacity is crucial for storing and processing large-scale information, ensuring the quality of this data is equally important. Data quality directly impacts the accuracy and reliability of information networks. Regardless of how high the data capacity is, its value diminishes significantly if the quality is poor. Particularly for outdoor information networks, which typically cover extensive areas in free space, data quality is paramount for effective analysis and decision-making. However, maintaining high quality in the outdoor scenario faces three major challenges from atmospheric turbulence, random scatterers and misalignment [43, 21]. Light is sensitive to atmospheric turbulence and relies heavily on line-of-sight propagation, making it susceptible to random light scatterers. On the other hand, an incoming light beam and a receiver aperture are easily misaligned. Unfortunately, coherent structured light fields are easily distorted by these factors. Consequently, additional technologies have to be supplemented to improve the transmission quality. To address the issue of atmospheric turbulence, pre-compensation and post-compensation adaptive optics technologies are utilized [43]. Meanwhile, some novel strategies are being rapidly explored, such as the use of anti-turbulence beams as information carriers [54], the application of scattering matrices to retrieve transmitted signals [55], and the deployment of artificial neural networks to distinguish intermodal coupling patterns [56]. As for the challenge of random obstacles, novel light with self-healing and self-bending abilities has been introduced, such as Bessel beams and Airy beams [57, 58]. To tackle the problem of misalignment, electrical digital signal processing technologies are employed, such as MIMO [59]. Regrettably, integrating all these techniques will cause a high-cost setup and enormously complicated process, contradicting the real-time and high-speed requirements of the communication process. Therefore, the research into tailoring light fields to improve communication quality and capacity has been ongoing.

In addition to the traditional DoFs, the degree of spatial and/or temporal coherence of light, which has not hitherto been explored in connection with free-space

information networks, has recently piqued researches' curiosity [60]. The coherence of light refers to the degree of optcial field correlations between pairs of points in space and time. Laser beams with infinite transvers coherence scales are usually regarded as fully coherent because they maintain their phase over both space and time. Unlike laser light, sunlight is generally considered to be incoherent, with the coherence scale being nearly zero. Therefore, the light fields whose coherence scale is between 0 and infinity, fall into the category of partially coherent light. In the space-frequency domain, the cross-spectral density (CSD) of a partially coherent light field is an autocorrelation function of the fields at a pair of spatial points at frequency ω [60, 61],

$$W\left(\mathbf{r}_1, \mathbf{r}_2, \omega\right) = \left\langle E^*\left(\mathbf{r}_1, \omega\right) E\left(\mathbf{r}_2, \omega\right)\right\rangle, \tag{1.1}$$

where $E(\mathbf{r}, \omega)$ is a scalar field at a position $\mathbf{r}$ at frequency ω, and the angular brackets denote an ensemble average. It is also the Fourier transform of the mutual coherence function $\Gamma\left(\mathbf{r}_1, \mathbf{r}_2, \tau\right)$ with respect to the time delay τ in the space-time domain [62]. Further, a degree of coherence (DOC) of the field is defined as [60, 63],

$$\mu\left(\mathbf{r}_1, \mathbf{r}_2, \omega\right) = \frac{W(\mathbf{r}_1, \mathbf{r}_2, \omega)}{\sqrt{W(\mathbf{r}_1, \mathbf{r}_1, \omega)}\sqrt{W(\mathbf{r}_2, \mathbf{r}_2, \omega)}}, \tag{1.2}$$

where $0 < |\mu| < 1$. By arbitrarily tailoring coherence, novel light sources that generate structured random light can be designed. During past several decades, remarkable progress has been made in designing structured random light fields. This has been a multi-stage process.

In the first stage, the studies mainly focused on the beam generation and coherence detection both in theory and experiment [64, 65, 66, 67]. The practical realization begins with the generation of a Collett-Wolf source, which is as highly directional as a fully coherent laser source.[64, 65]. This type of source is nearly spatially incoherent, as a limiting case of quasi-homogeneous sources. [68] Subsequently, it extends to a general case, known as Gaussian Schell-model (GSM) beams, whose far-field intensity distribution and DoC are both Gaussians, just as those at the source[66, 69]. General Schell-model sources are statistically homogeneous [66]. In parallel, various modal representations in the temporal/spectral domain have been proposed. For example, the elementary-field approach specifies that the CSD of any partially coherent source can be represented as a continuous, incoherent linear superposition of mutually

independent (but same) coherent elementary fields f, with the weight function s [70]

$$W(\mathbf{r}_1, \mathbf{r}_2) = \int s(\mathbf{r}') f^*(\mathbf{r}_1 - \mathbf{r}') f(\mathbf{r}_2 - \mathbf{r}') \, d\mathbf{r}'. \tag{1.3}$$

Utilizing a complex Gaussian representation [71], the CSD of any partially coherent source can be expanded into a complete set of pseudo-modes as [72, 73]

$$W(\mathbf{r}_1, \mathbf{r}_2) = \int p(\boldsymbol{\alpha}) \varphi_{\boldsymbol{\alpha}}^*(\mathbf{r}_1) \varphi_{\boldsymbol{\alpha}}(\mathbf{r}_2) \, d^4\boldsymbol{\alpha}, \tag{1.4}$$

where the complex Gaussian function is

$$\varphi_{\boldsymbol{\alpha}}(\mathbf{r}) = \frac{e^{-(\mathrm{Im}\boldsymbol{\alpha})^2}}{\pi^{1/2}} \exp\left[-\frac{\left(\mathbf{r} - \sqrt{2}\boldsymbol{\alpha}\right)^2}{2}\right]. \tag{1.5}$$

Here $\boldsymbol{\alpha}$ denotes a complex vector specifying displacement, and a nonnegative function p is associated with coherence properties of the source. An important advantage of the complex Gaussian representation over the competition is that, in principle, given the CSD of the source, any source can be represented this way because there exists an explicit integral representation for p in terms of W. On the flip side, though, an explicit expression for p might be very complicated, involving multiple folded integrals.

These representations efficiently reduce the computational complexity of partially coherent sources, opening up avenues for the arbitrary design of structured random light. In 2007, a general procedure to design any bona fide (that is non-negative definite) structured random light field was advanced [74]. It follows that the cross-spectral density of any genuine random source must have the form

$$W(\mathbf{r}_1, \mathbf{r}_2) = \int p(\mathbf{v}) H^*(\mathbf{r}_1, \mathbf{v}) H(\mathbf{r}_2, \mathbf{v}) \, d\mathbf{v}, \tag{1.6}$$

where $p(\mathbf{v})$ is a real, non-negative function, and $H(\mathbf{r}, \mathbf{v})$ can be an arbitrary complex function. Within these constraints, by adjusting functions p and H, specific spatial correlated structures can be constructed. Thus, the structured random light is generated. For example, let $H(\mathbf{r}, \mathbf{v}) = \tau(\mathbf{r}) \exp(-2\pi i \mathbf{v} \cdot \mathbf{r})$ and substitute it back into Eq. (1.6), we can represent the CSD of any statistically homogeneous, or Schell-model source as

$$W(\mathbf{r}_1, \mathbf{r}_2) = \tau^*(\mathbf{r}_1) \tau(\mathbf{r}_2) \tilde{p}(\mathbf{r}_1 - \mathbf{r}_2). \tag{1.7}$$

It follows that the degree of coherence $\mu(\mathbf{r}_1, \mathbf{r}_2)$ of any Schell-model source is a Fourier transform of p, denoted as $\tilde{p}\,(\mathbf{r}_1 - \mathbf{r}_2)$.

Alternatively, CSDs of bona-fide sources can be expressed in terms of coherent modes as [75]

$$W\,(\mathbf{r}_1, \mathbf{r}_2) = \sum_n \lambda_n \psi_n^*\,(\mathbf{r}_1)\,\psi_n\,(\mathbf{r}_2), \tag{1.8}$$

where the weight $\lambda_n \geq 0$ yields a power carried by the nth mode.

Meanwhile the studies on experimental generation and detection methods have also proceeded vigorously. The explored experimental methods can be divided into three categories, each characterized by their principles and optical components with its own advantages and drawbacks. The earliest generation method involves utilizing dynamic scatterers to reduce DOC of lasers, allowing for real-time generation of Schell-model sources [76]. Later, with the advances in light wave-front manipulation, digital generation methods based on phase-only spatial light modulators (SLM) were developed [77, 78]. These approaches provide greater flexibility in generating a wider range of sources. Additionally, there exists another holographic method for generating random fields which can be expanded as a series of coherent modes, where each hologram represents one coherent mode [79]. Although the SLM and holographic methods are more advanced than the dynamic scatterer based ones, longer computation times are required. In parallel, the corresponding detection methods have been advanced that stem from Hanbury Brown and Twiss type experiments, such as intensity-intensity correlation measurements and intensity cross-correlation of fluctuating fields [80, 81].

In the second stage, the focus was on exploring physical phenomena arising from partially coherent field propagation. Various correlated structures exhibit different propagation properties, making them suitable for diverse applications. By customizing $p(\mathbf{v})$, such sources exhibit desired self-shaping far-field patterns, which can be advantageous for various optical applications [82]. For example, Laguerre-Gaussian (LG) correlated Schell-model sources [83], whose correlation function stems from $p(\mathbf{v}) \propto (\mathbf{v}^2\sigma_c^2/2)^{|l|}\left[L_p^{|l|}(\mathbf{v}^2\sigma_c^2/2)\right]^2 e^{-\mathbf{v}^2\sigma_c^2/2}$, evolve into ring-shaped spatial patterns on propagation in free space. Decreasing their initial coherence width can shape the far-field patterns into Gaussian profiles. This feature can be useful for particle trapping [84]. Multi-Gaussian correlated Schell-model beams have far-field flat-top

intensity profiles, making them suitable for applications in laser processing and medical therapy [85]. Partially coherent beams with spatially varying correlations exhibit a self-focusing effect on propagation in free space, which can be beneficial for improving the resolution of biomedical imaging [86]. Spatial optical coherence lattices exhibit periodicity reciprocity between the DOC at the source and their far-field intensity distributions: the periodic DOC at the source transfers its periodicity to the intensity distribution during free-space paraxial propagation [72, 87]. This unique property quickly propels their development into a lattice family, encompassing partially coherent Bessel beam arrays, plasmonic coherence lattices, and perfect optical coherence lattices [88, 89, 90]. Experimental results related to this family expose their potential for image transmission and optical encryption [91].

Besides, all the correlated sources share one common feature: they effectively resist the deleterious effects caused by atmospheric turbulence over a given stretch in the medium [92, 93]. Furthermore, to enhance their resistance to turbulence and achieve kilometer scale propagation, partially coherent diffraction-free beams, have been proposed. The CSD of any such beam must have the form [94].

$$W(\mathbf{r}, \mathbf{R}) = \Phi(\mathbf{r}) + \Psi(\mathbf{R}), \tag{1.9}$$

where $\mathbf{r}$ and $\mathbf{R}$ are the new variables to replace $\mathbf{r}_1$ and $\mathbf{r}_2$ by the relationships $\mathbf{r} = \mathbf{r}_1 - \mathbf{r}_2$ and $\mathbf{R} = (\mathbf{r}_1 + \mathbf{r}_2)/2$. The arbitrary function Φ and Ψ should follow the constraints to satisfy the Hermiticity of CSD,

$$\Phi^*(-\mathbf{r}) = \Phi(\mathbf{r}), \Psi^*(-\mathbf{R}) = \Psi(\mathbf{R}). \tag{1.10}$$

As a result, one can model a variety of partially coherent diffraction-free beams. For example, dark or antidark (DAD) beams on incoherent background, $W(\mathbf{r}_1, \mathbf{r}_2) = J_0(\beta|\mathbf{r}_2 - \mathbf{r}_1|) + \alpha J_0(\beta|\mathbf{r}_2 + \mathbf{r}_1|)$, are extremely robust to fluctuations when propagating through the turbulent atmosphere, making them structurally stable for FSO communications [95].

On the other hand, a large number of experiments show that the structured random light with a short transverse coherence length can self-heal after encountering obstacles [96]. Research on the physical mechanism of self-healing and fundamental properties mentioned above has laid the foundation for numerous follow-up applications of structured random light [97].

In the third stage, with the support of advanced modulation technologies, new applications emerged. The integration of coherence with other traditional DoFs is evolving for more diversified applications and efficient optical functionalities, such as the joint modulation of coherence with polarization, vortex phase, and twist phase [98, 99, 100]. For example, the detailed information about a semi-rough target can be detected by comparing the beam scale and coherence radius of the incident and reflected beams [101]. Furthermore, structured random light has been applied to high-resolution imaging, trapping micro particles with different refractive indices, and encrypted image transmission [102, 103, 104]. These studies underscore the significant potential of structured random light in the field of new-generation information networks.

1.2 Thesis Motivations and Objectives

With the maturity of modulation techniques, the time has come for structured random light to facilitate major breakthroughs toward a new generation of information carrying networks, especially in the outdoor wireless information acquisition and transport [105, 106]. Why do we have confidence in the potential of the structured random light for information networks? This is because such light meets the demands of new-generation information networks to establish smart, low-cost, and efficient information systems with high-capacity and improved-quality data transfer.

Since structured random light possesses the additional DoF, coherence, it shows outstanding robustness against turbulence and can also self-heal when partially blocked by obstacles, ensuring that optical signals remain intact. Therefore, such light utilized in communication systems, can maintain stable transmission and ensure the robustness and reliability of a communication link, even in noisy outdoor environments. Furthermore, structured random light has infinite mutually orthogonal coherent modes as a reward; these states are mutually uncorrelated relative to each other and can work as separate data channels. As a structured random light beam is multiplexed with traditional DoFs, the capacity of optical systems can be significantly enhanced. Consequently, this unique DoF makes it adept to improve communication quality and capacity. Hence, it is reasonable to expect that structured random light

carries immense promise for new-generation information networks. The natural question then is: How can one incorporate structured random light into a noisy wireless information network? This thesis aims to address this question.

New-generation communication systems are anticipated to offer high capacity and improved quality of service, fully supported by artificial intelligence (AI). Therefore, we seek to establish a robust high-capacity communication system for FSO information transport using the integration of structured random light and deep learning algorithms. Furthermore, in terms of high-capacity data and long-haul transmission in noisy environment, we plan to employ a powerful alliance between structured random light and appealing vortex-based communication techniques. To achieve this goal, we intend to develop a vortex-correlated structured light source generating light beams resilient to diffraction and turbulence, serving as an optimal candidate for enhancing communication capabilities in challenging environments.

On the other hand, to address increasingly complex information networks, an advanced detection protocol on the new-generation miniaturized hardware is crucial to improve the overall network efficiency. Regarding this, we propose a multi-function radar system that incorporates an appealing structure–the vortex phase, to ensure optimal performance in terms of versatility and adaptability.

At the same time, available and secure information storage is essential to maintain confidentiality and integrity of vast amounts of received information. Some number factorization related applications, like OAM holographic encryption scheme, can further enhance the security of information [107, 108]. Therefore, we introduce a protocol involving OAM carrying beams and a carefully engineered prime number sieve for simple and effective factorization of prime numbers, thereby enhancing information security and effectively maintaining the integrity of information throughtout the communication process.

1.3 Thesis Outline

This thesis is based on papers published or submitted for publication by the author. Each chapter is dedicated to a single paper while the introduction to each and every chapter identifies and summarizes the author's original contribution.

In Chapter 2, we advance theoretically and realize experimentally a potentially

high-capacity FSO protocol that enables high-fidelity transfer of an image, or set of images through a complex environment. In our protocol, we complement random light structuring at the transmitter with a deep learning image classification platform at the receiver. Multiplexing novel, independent, mutually orthogonal degrees of freedom available to structured random light can potentially significantly boost the channel communication capacity of our protocol without introducing any deleterious crosstalk. Specifically, we show how one can multiplex the degrees of freedom associated with the source coherence radius and a spatial position of a beamlet within an array of structured random beams to greatly enhance the capacity of our communication link. The superb resilience of structured random light to environmental noise, as well as extreme efficiency of deep learning networks at classifying images guarantees high-fidelity image transfer within the framework of our protocol.

In Chapter 3, we introduce a class of random optical vortices that possess two distinct features. First, their two-point spatial correlation structure is independent of their topological charge, hence the name perfect correlation vortices (PCV). Second, PCVs are nearly immune to diffraction in the low-coherence limit and maintain their perfect vortex structure in free space over any desired distance. Moreover, the vortex structure of a PCV is robust even against strong atmospheric turbulence over modest propagation distances. We derive a closed-form analytical expression for the degree of coherence of a PCV field and show it to be statistically homogeneous in any transverse plane. Incredible resilience of the discovered PCVs to diffraction and turbulence makes them ideal candidates for FSO communications and imaging through random media.

In Chapter 4, we theoretically propose a promising protocol that integrates efficient data processing methods with robust hardware for detecting, positioning and tracking moving targets in real-time. In our scheme, the emitted field is modulated by optical vortices, and the received field is processed in real-time, thereby synchronizing the functions of imaging, target positioning, and tracking. Moreover, the protocol extends its utility to serve as a topographic laser profiling system for geographic landscapes, highlighting its adaptability to varied scenarios. This adaptability and versatility position the proposed protocol to support a wide range of applications,

ranging from self-driving vehicles to aerial systems, underscoring its potential significance across diverse platforms.

In Chapter 5, we point out a link between OAM carrying light beams and number theory. The established link makes it possible to formulate and implement a simple and fast protocol for prime number factorization by employing OAM endowed beams that are modulated by a prime number sieve. We are able to differentiate factors from non-factors of a number by simply measuring the on-axis intensity of light in the rear focal plane of a thin lens focusing a source beam. The proposed protocol solely relies on the periodicity of the OAM phase distribution, and hence it is applicable to fully as well as partially coherent fields of any frequency and physical nature from optical, or x-ray to matter waves-endowed with OAM. Our experimental results are in excellent agreement with our theory. We anticipate our protocol to trigger new developments in optical cryptography and information processing with OAM beams.

Chapter 6 presents a brief discussion, concluding remarks, and offer the direction for future work.

Chapter 2

Deep learning and random light structuring ensure robust free-space communications

This chapter's work is published in the paper entitled "Deep learning and random light structuring ensure robust free-space communications", Applied Physics Letters 124 (21), 214103 (2024). The authors are Xiaofei Li, Yu Wang, Xin Liu, Yuan Ma, Yangjian Cai, Sergey A. Ponomarenko and Xianlong Liu. We propose a high-capacity FSO protocol that enables high-fidelity transfer of images through a complex environment, benefiting from the complement random light structuring at the transmitter with a deep learning image classification platform at the receiver.

My contribution to this work includes carrying out the experiments, performing formal analysis, analyzing methodology, and writing original draft.

2.1 Introduction

In the age of information explosion, there has been growing demand for high capacity communication systems due to relentless growth of traffic through any available communication channel [109]. To achieve high-capacity communications within the framework of free-space optics, it is essential that all available degrees of freedom of a light field be explored and engaged. To date, a number of approaches to boost the transmission capacity of free-space optical communications have been proposed [110, 111, 112], including a quadrature phase shift keying [38], wavelength division multiplexing [35], space division multiplexing [33], and polarization division multiplexing [34]. To further increase the channel capacity to overcome the existing bottle necks, the orbital angular momentum division multiplexing has lately been proposed [113, 43, 114] . Apart from the capacity limitations, though, free-space optical communications are hampered by the transmission quality degradation owning to the data crosstalk [115]. The latter is chiefly due to the challenge posed by a realistic transmission medium involving atmospheric turbulence and/or solid particles, such

as aerosols, in the light path from a source (transmitter) to a receiver [43]. Indeed, the refractive index of the atmosphere fluctuates due to the temperature and humidity variations, giving rise to turbulent effects. The atmospheric fluctuations distort the phase of a transmitted light beam, causing deleterious crosstalk among multiple independent degrees of freedom (DoF) of a free-space communication link [115]. As atmospheric turbulence seriously hinders further progress toward high-quality, high-capacity optical communications through a realistic complex environment, numerous strategies have been proposed to remedy the channel crosstalk [116, 117, 118, 119]. In addition to multiple adaptive optics techniques, which can be subdivided into two main groups, pre-compensation and post-compensation [43], there is a spatial polarization differential phase shift keying technology for vector light beams [54] and scattering-matrix-assisted retrieval protocol [55]. Unfortunately, virtually all these strategies require complicated, and often time-consuming, data processing and they invariably fail to lower crosstalk to an acceptable level. Further, to compensate for light scattering obstacles in the transmission path, self-healing coherent light sources, such as the ones generating Bessel beams, have been employed to help self-reconstruct transmitted image structure past opaque obstructions [57, 120].

At the same time, recent work has established extraordinary resistance of structured random beams to atmospheric turbulence and their outstanding self-healing ability upon encountering obstacles [92, 96, 97, 95]. In particular, the authors of [95] have demonstrated that there exist structured random beams maintaining their intensity profile structure in the turbulent atmosphere over a distance determined by the turbulence strength. In contrast to fully spatially coherent fields [121], structured random fields possess a new degree of freedom, the normalized autocorrelation function of the fields at a pair of points across the source, known as the degree of coherence of a source [60, 63]. This DoF has been explored to realize high-security optical data storage and retrieval. Moreover, various aspects of optical field correlations at the source, for example, their spatial structure, transverse coherence radius, or classical entanglement [100] provide access to numerous, untapped, mutually orthogonal DoFs that can be employed for high-capacity, high-fidelity optical communications through complex environments.

In this work, we combine structured random light engineering at the source to

encode an image into the novel DoFs of such light and deep learning framework at the receiver to propose theoretically and realize experimentally high-fidelity image transmission through a complex environment. In particular, we employ statistically homogeneous, Laguerre-Gaussian correlated sources which produce optical fields with ring correlation structure at the source and ring-like far-field intensity profiles. We demonstrate that such ring-like patterns can be utilized to encode image information. We also show how the source coherence radius can be used as another independent DoF for information encoding. Further, we demonstrate experimentally that supreme resilience of structured random light to atmospheric fluctuations and their excellent ability to self-heal upon encountering obstacles augurs well for the fidelity of image transfer, at least, over short free-space communication links. We reveal the multiplexing capabilities of novel DoFs of random light. For instance, we show how the source coherence radius can be multiplexed with the space position of any beamlet within an array of partially coherent beams carrying image information to the receiver. These multiplexing capabilities demonstrate the potential for significant enhancement of information capacity within our protocol.

Yet another novelty of our protocol is the use of deep learning network capabilities for pattern classification at the decoding stage. In recent years, deep learning has enjoyed immense success in computer science, making it possible to advance data-driven artificial intelligence technologies, such as computer vision [122], speech recognition [123], and decision making [124]. Recent applications of deep learning in photonics range from accurate prediction of resonance spectra [125] and inverse design of photonic devices [126] to high-resolution retrieval of orbital angular momentum states [127] and accurate phase prediction for anisotropic digital coding metasurfaces [128]. Although a deep convolutional neural network (CNN), which can be applied to classification tasks [129], is the most popular, recently proposed residual networks (ResNets), which can scale up to thousands of layers, have demonstrated excellent promise for classification tasks with low training errors [130]. For these reasons, we employ ResNet 34 for image decoding at the receiver end. The fusion of random light structuring at the transmitter and deep learning image classification at the receiver renders our protocol a promising candidate to realize high-fidelity optical

image transmission through a noisy link with a potential to attain high communication channel capacity via tapping into novel crosstalk-free DoFs available to random light sources. As an added bonus, our work will undoubtedly inform further research in the topical field of deep learning network applications to photonics.

2.2 Image transmission employing source correlation structure

Consider a structured random light field propagating along the z axis. In the space-frequency representation, we can describe the second-order correlations of the fields at a pair of points $\mathbf{r}_1$ and $\mathbf{r}_2$ in the transverse plane of the source in terms of a cross-spectral density of the source. We can express the cross-spectral density of any physically realizable statistical source as [131]

$$W_0(\mathbf{r}_1, \mathbf{r}_2) = \int d\mathbf{k}\, p(\mathbf{k}) H^*(\mathbf{r}_1, \mathbf{k}) H(\mathbf{r}_2, \mathbf{k}). \tag{2.1}$$

Here, $H(\mathbf{r}, \mathbf{k})$ is an arbitrary kernel at a temporal frequency ω and $p(\mathbf{k})$ is a nonnegative spectral distribution function in the reciprocal k-space; we will drop any explicit dependence on ω hereafter.

Let us now focus on statistically homogeneous light sources for which $H(\mathbf{r}, \mathbf{k}) = \sqrt{I(\mathbf{r})} e^{i\mathbf{k}\cdot\mathbf{r}}$, where $I(\mathbf{r})$ is a source intensity profile [131]. It then follows at once from Eq. (3.5) that the degree of coherence $\mu_0(\mathbf{r}_1 - \mathbf{r}_2)$ of such a source, defined as a normalized second-order correlation function $\mu_0(\mathbf{r}_1, \mathbf{r}_2) = W_0(\mathbf{r}_1, \mathbf{r}_2)/\sqrt{I(\mathbf{r}_1) I(\mathbf{r}_2)}$ [60, 121], is simply a Fourier transform of $p(\mathbf{k})$. Further, the far-field intensity profile of a low-coherence source has the same functional form as $p(\mathbf{k})$ [60]. Therefore, the spatial structure of source correlations, or equivalently, its spectral density distribution $p(\mathbf{k})$ can serve as an independent DoF for information encoding. We choose a Laguerre-Gaussian (LG) correlated Schell-model source as a representative example [83]. The spectral density of such a source reads

$$p(\mathbf{k}) \propto (\mathbf{k}^2 \sigma_c^2/2)^{|l|} \left[L_p^{|l|}(\mathbf{k}^2 \sigma_c^2/2)\right]^2 e^{-\mathbf{k}^2 \sigma_c^2/2}. \tag{2.2}$$

Here σ_c is a coherence radius of the source, $L_p^{|l|}$ stands for an associated Laguerre polynomial of azimuthal l and radial p indices, respectively. We can then generate a multitude of LG-correlated sources by varying p and l. Further, one can easily verify

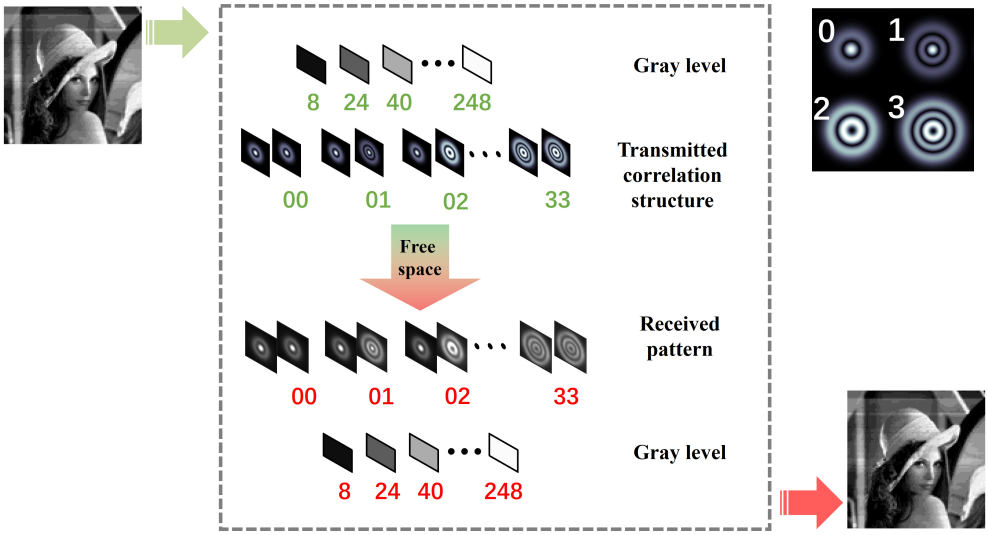

Figure 2.1: Schematics of our encoding/decoding protocol with LG correlated beams.

that a Fourier transform of the spectral density of the LG-correlated source yields yet another LG-like spatial pattern.

We are now in a position to describe our strategy to encode a desired image into an ensemble of light beams generated by an LG-correlated source. We sketch the schematics of our protocol in Fig. 2.1. We exhibit 4 LG profile patterns, which we refer to as states hereafter, as an illustrative example of image encoding into LG spatial correlations of a source. The source produces an ensemble of LG correlated beams of spot size $w = 0.68$mm and coherence radius $\sigma_c = 0.1$mm, propagating from the source (transmitter) to a receiver. The ensemble contains LG states corresponding to four index parameters: LG_{10}, LG_{20}, LG_{12}, and LG_{22}. The transmitted information in our protocol is a 16-grey-level (8, 24, 40, 56, 72, 88, 104, 120, 136, 152, 168, 184, 200, 216, 232, and 248) image of Lena which has 100×100 pixel resolution. The grey level of the image is quantified by 2-digit quaternary numbers (00, 01, 02, 03... 32, 33). Here, every quaternary number corresponds to an LG correlated beam structure (0 is LG_{10}, 1 is LG_{20}, 2 is LG_{12}, and 3 is LG_{22}). Therefore, we can encode the grey level of each pixel at the transmitter and store it in 2 LG correlated beam structures. Next, we transmit the encoded information from the source to the receiver in free space, or realistically through a random medium, with the aid of an ensemble of LG correlated beams. In the case of free-space propagation, the intensity patterns at the receiver, situated in the far-zone of the source, are proportional to $p(\mathbf{k})$ which

is evaluated at **r**. Further, we record the intensity patterns of the received beam ensemble with a CCD camera and decode them into a set of quaternary numbers following the encoding rules. Finally, we collect a set of pixels of variable grey level encapsulating the transmitted image.

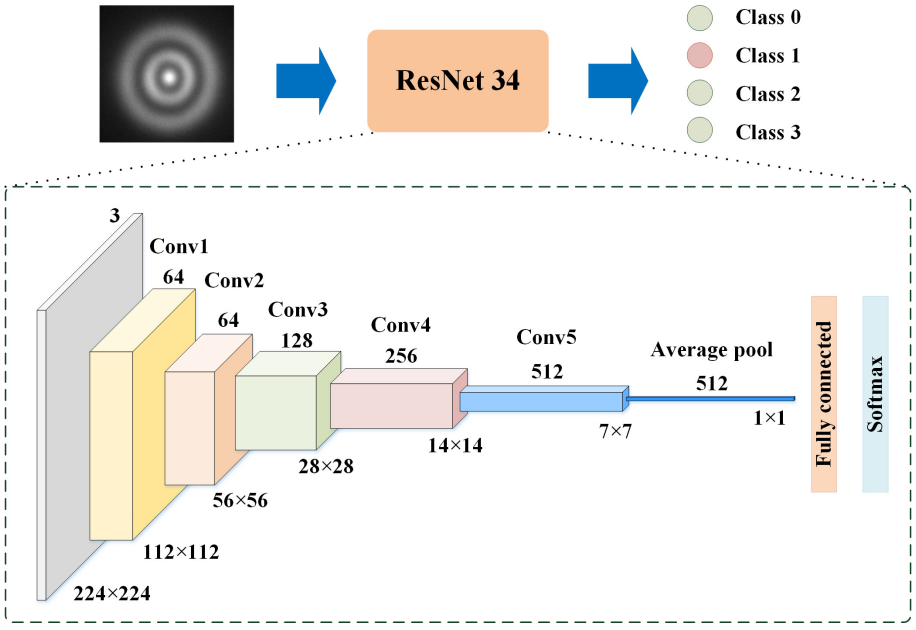

Figure 2.2: Decoding process and the architecture of ResNet 34 classifier.

We employ a deep residual learning ResNet architecture with 34 layers, known as ResNet 34 network. The network is only interested in the image of intensity patterns and these patterns are directly accessible to the computers. First, we order sequentially all members of an LG-correlated beam ensemble recorded by the camera. In the following step, we have the network classify the received images and map them into quaternary numbers for subsequent decoding. Thus, each intensity pattern can be converted into a set of digital numbers by the classifier network as shown in Fig. 2.2. We display the basic framework of ResNet 34 classifier in the dashed square of Fig. 2.2 and we discuss the details of the overall structure of the network in Section 1 of the Appendix A, see especially Tab. 6.1 and Fig. 6.1. We now outline how ResNet 34 works in a classifier mode. Inspired by the concept of transfer learning, we use the pre-trained parameters, which have been previously trained and tested on the ImageNet dataset[132], for initialization. We then fine-tune ResNet 34 with our images to suit a particular classification task. At the outset, we prepare 200 experimental images with

labels for each category and combine them into a training dataset. Next we resize all the training images to 224×224 to be served as input to the network. To obtain a robust classifier model, we divide the whole training dataset randomly into three non-overlapping subsets in proportion 70%, 20% and 10%, corresponding to the training, validation, and test sets, respectively. Specifically, to avoid any bias caused by class imbalance, we make sure that the number of different class samples is the same in each subset. We utilize the training set to learn the characteristics of the data and develop a model. The validation set is used to adjust the parameters and hyper-parameters of the model during the training process to improve the model performance. The test set should not be used in the training phase and is used to evaluate the performance and robustness of the model on unseen data[133]. Having taken these steps, we have established a robust ResNet 34 network ready to classify images. We then resize images to be tested and feed them into the established classification network, which realizes decoding in our protocol. Each tested image corresponds to the network output category, with the corresponding quaternary number specifying its grey level. Once the decimal grey value of each pixel is obtained, we can identify the whole image.

We employ a workstation with Ubuntu 18.04 OS, PyTorch platform, 32 GB RAM and NVIDIA Titan RTX for decoding. Due to the difference in the number of classes—while ImageNet has 1000 classes, we have only 4 classes—we only need to load the pre-trained parameters of the first 33 layers prior to training. The training is carried out by Adam optimizer[134] with an initial learning rate of 0.0001 and a batch size of 32. The overall training phase requires 20 epochs. The training is carried out in an end-to-end fashion.

We verify our protocol by carrying out proof-of-principle image transmission with an experimental setup sketched in Fig. 2.3(a). First, we produce a fully coherent Gaussian beam with the help of a continuous-wave-diode-pumped laser with the carrier wavelength $\lambda_0 = 532$ nm and transmit the beam through a neutral density filter (NDF). After having been expanded and collimated by a beam expander (BE) comprised of two lenses of different focal length, L_1 and L_2, the beam is reflected by a spatial light modulator (SLM), which displays a hologram dataset of LG patterns encapsulating the encoded information. The generated LG beams are then focused

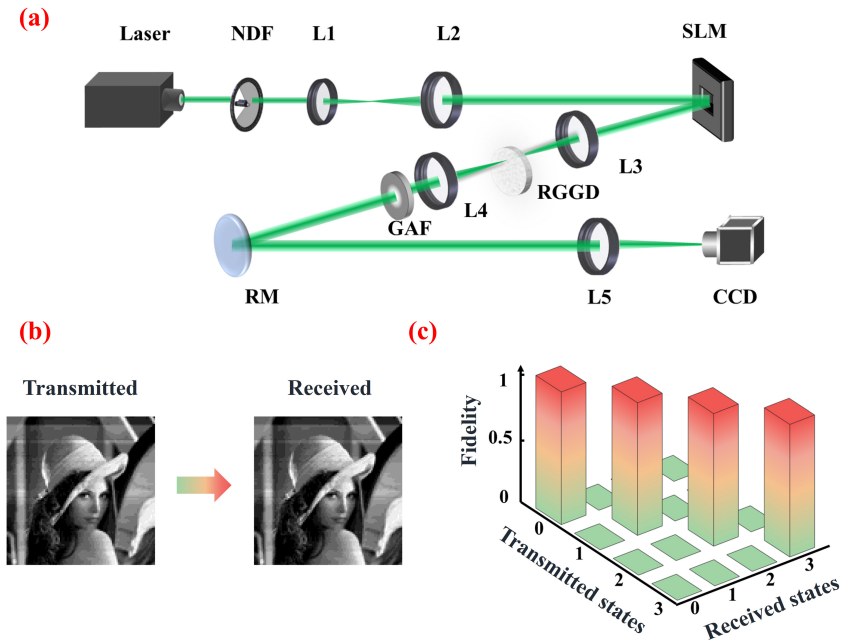

Figure 2.3: Experimental verification of our protocol. (a) Experimental setup. NDF: neutral density filter; L: thin lens; RGGD: rotating ground glass disk; GAF: Gaussian amplitude filter; SLM: spatial light modulator; RM: reflected mirror; and CCD: charge coupled device. (b) Qualitative juxtaposition of transmitted and received images. (c) Quantitative measure of the state detection fidelity as a conditional probability $P_{s_r|s_t}$ of finding a transmitted state s_t in state s_r , where $s_r(s_t)$ is represented in the quaternary basis (0, 1, 2, 3).

by a lens L_3 ($f = 250$mm) and projected onto a rotating ground glass disk (RGGD), which we place in the front focal plane of a collimating lens L_4. Next, an LG-correlated beam emerges past L_4 ($f = 150$mm) and a Gaussian amplitude Filter (GAF) and we encode the transmitted information into its spatial correlation structure. Having propagated a 1.92m stretch of free space, the beam is focused onto a charge coupled device (CCD) camera by a lens L_5 ($f = 150$mm). The camera serves as a receiver recording the intensity patterns of an LG-correlated beam ensemble.

We contrast the transmitted and received images of Lena in Fig. 2.3(b). We can readily infer from the figure that there is excellent qualitative resemblance between the transmitted and received images attesting to the viability of our protocol. We then quantify the fidelity of each state in terms of a conditional probability $P_{s_r|s_t}$ of finding a transmitted state s_t in state s_r . We summarize the results in Fig. 2.3(c). The multitude of $100 \times 100 \times 2 = 20000$ received states are recognized by the ResNet

34 network, and the attained fidelity of the image transfer, evaluated as a fraction of correctly received states versus the total number of transmitted states, exceeds 99.99%.

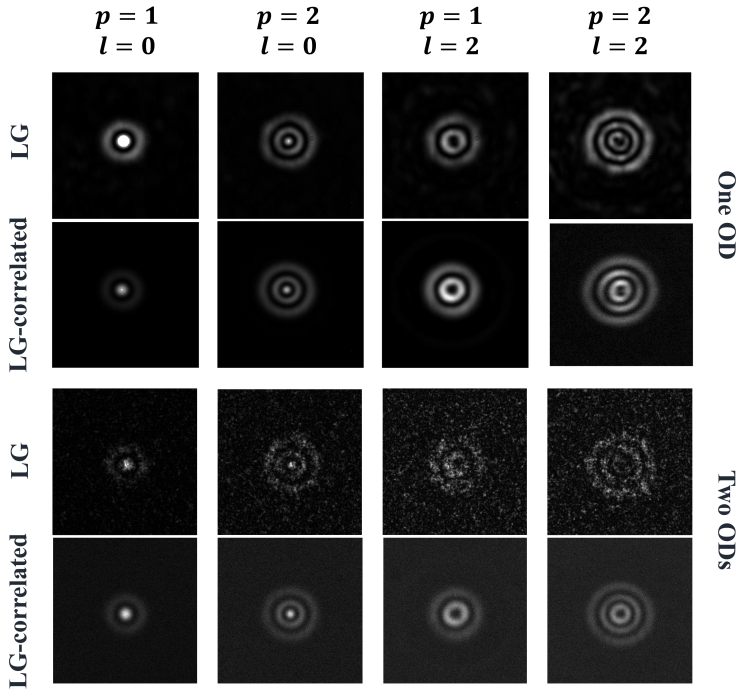

Figure 2.4: Recorded intensity profiles of LG-correlated versus fully coherent LG beams transmitted through either a single or two optical diffusers.

We now elucidate the role of noise due to either atmospheric turbulence or opaque obstacle scattering on image transmission quality within the framework of our protocol. There has been a growing body of evidence, see, for instance, [92] for a review that decreasing spatial coherence of a light source enhances the resilience of the beams generated by such a partially coherent source to random perturbations in a complex environment. In particular, it has been recently demonstrated [95] that there exists a class of structured random beams, the so-call dark and antidark beams on incoherent background [94] that maintain their intensity profile structure over certain propagation distances in the turbulent atmosphere, regardless of the turbulence strength. Instructively, the intensity profile of any such structurally stable beam has a ring structure, similar to that of the LG-correlated beams which we employ in our protocol. Therefore, we anticipate the latter to be fairly robust against atmospheric turbulence as well. To verify this conjecture, we record the intensity patterns of

LG-correlated beams propagating through a random medium mimicking atmospheric turbulence and compare them with those of fully coherent LG beams propagating through the same medium. We use optical diffusers (OD) to simulate turbulence, see the Appendix A for further information. We can infer from Fig. 2.4, that fully coherent LG beams are more distorted than their partially coherent cousins. This observation implies that image transmission through random medium and recovery of fully coherent LG beams are much more complicated and time consuming as well as far less accurate than those with LG correlated beams. Moreover, the situation exacerbates as the turbulence strength increases. We can model stronger turbulence with two ODs as opposed to weaker turbulence which can be modelled with just a single diffuser. By comparing the corresponding panels of Fig. 2.4, we observe that the advantage of reducing source coherence of the beam augments for stronger turbulence: We clearly distinguish a ring structure of the LG-correlated beam in stronger turbulence, while the intensity profile of a fully coherent LG beam swiftly turns into essentially a random speckle pattern.

To test our protocol in the more adverse situation, we repeat all protocol steps, except we include two ODs to model stronger turbulence as a propagation milieu. We transmit a 16-grey-level Lena image of 80×80 pixel resolution. We present an experimental setup schematics in Fig. 6.2 of the Appendix A. Our results show good tolerance of the protocol to medium turbulence and yield the fidelity of image retrieval of over 99.99%, which can be inferred upon comparison of the transmitted and received states in Fig. 2.2(b).

By the same token, random beams of sufficiently low coherence are known to self-heal upon encountering discrete obstacles such as suspended particles in free space [96]. In Fig. 6.3 of the Appendix A, we provide experimental evidence of LG-correlated beam self-healing capabilities by comparing its evolution with that of a fully coherent LG beam after the cross-section of either beam has been partly blocked by an opaque obstacle. We then repeat our protocol for a 16-grey-level Lena image of 86×86 pixel resolution and are able to accurately transmit the image through a medium containing obstructing particles to the fidelity of over 99.99%, see also Fig. 6.6. We remark that the extremely high fidelity of image transmission in free-space and turbulent or colloidal particle medium is achieved thanks to the superb job

that a deep learning network, such as ResNet 34, does to faithfully decode images.

2.3 Image transmission utilizing source coherence radius

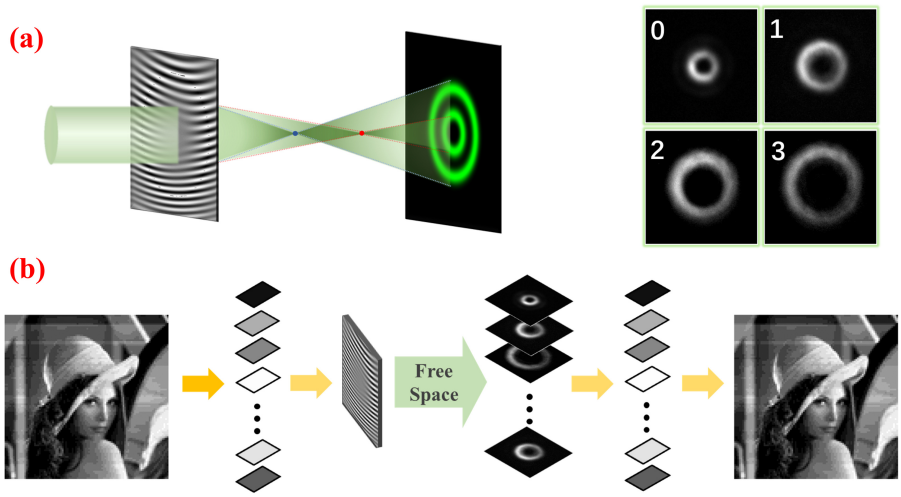

Figure 2.5: Schematics of the image transfer protocol employing the source coherence radius for information encoding. (a) Illustrating control of the transverse coherence radius of the source with a focusing hologram. (b) The image transmission protocol involving the spatial coherence radius DoF.

We now illustrate an alternative strategy of encoding image information into the transverse coherence radius of a light source which can be viewed as another independent degree of freedom for free-space optical communications. To be consistent, we employ an LG-correlated source as well, so that we can encode the Lena image into coherence radii of LG ring patterns. To this end, we select 4 distinct states of an LG-correlated beam with the ring structure corresponding to LG_{04} of the same spot size $w = 0.68$mm and the coherence radii at the source $\sigma_c = 0.02$mm, 0.025mm, 0.03mm, 0.05mm as an example. Notice that all four states have low coherence in the sense that $\sigma_c \ll w_0$. In the protocol described in Section 2, we impart a phase Φ_{LG} with a phase-only hologram to generate an LG-correlated source. The source coherence radius depends on the spot size of the coherent beam incident on the RGGD. The spot size is, in turn, controlled by adjusting the distance between L_3 and RGGD. In the alternative strategy, we should be able to control the coherence radius of the source without affecting the other parameters of the experimental setup. With this purpose, we employ a digital focusing hologram [135] to tune the

coherent beam spot size digitally without affecting any distances between optical elements. It follows that for a fixed distance between SLM and RGGD, the spot size is controlled by the focal length f of the hologram as we show in Fig 2.5(a). As a result, the coherence radius of the LG-correlated source can be modified. Thus, the source coherence can be modulated by refreshing holograms on SLM. The transfer function of the digital hologram is a combination of that of a focusing element, $t\left(x,y\right)=\exp[i\frac{k_0}{2f}(x^2+y^2)]$, where $k_0=2\pi/\lambda_0$ and the transfer function of a linear phase grating, $t_{\mathrm{g}}\left(x,y\right)=\exp[i2\pi\left(ux+vy\right)]$, where u and v are inverse grating periods along the x- and y-directions, respectively. Therefore, the hologram for image encoding into the source coherence radius modifies the phase of an input beam to

$$\Phi=\mathrm{mod}\left[\Phi_{LG}+\frac{k_0}{2f}(x^2+y^2)+2\pi\left(ux+vy\right),2\pi\right]. \tag{2.3}$$

In Fig. 2.5(b), we illustrate the principle of our alternative image transmission protocol. Specifically, we encode a 16 grey-level Lena image of 90×90 pixel resolution into 4 states, corresponding to the LG-correlated sources of different coherence radii: 0 is $\sigma_c=0.05$mm, 1 is $\sigma_c=0.03$mm, 2 is $\sigma_c=0.025$mm, 3 is $\sigma_c=0.02$mm. The grey level value of each pixel is thus encoded into the coherence radius of an LG-correlated beam generated by the corresponding source. Following this procedure, we generate an ensemble of LG-correlated beams propagating in free space from the source to the receiver. At the receiver, we capture and decode $90\times90\times2=16200$ intensity profile images with the aid of a CCD camera and ResNet 34 network. Finally, we collect the grey level values of all image pixels and recover the image of Lena. As is evidenced by Fig. 2.5(b), the received image bears excellent resemblance to the transmitted one, attesting to the viability of our protocol.

The two protocols that we have described in Sections 2.2 and 2.3 involve two independent DoFs for free-space optical communications: the spatial structure of the source degree of coherence and the coherence radius of the source. Each of these DoFs can be multiplexed with other optical field characteristics such as spatial, polarization, and spectral (wavelength) DoFs to boost communication capacity of the protocol.

We illustrate multiplexing the coherence radius and spatial location of a beamlet within a source array to illustrate but one among multiple perspectives. We encode information at the transmitter by generating an array of LG correlated beams with

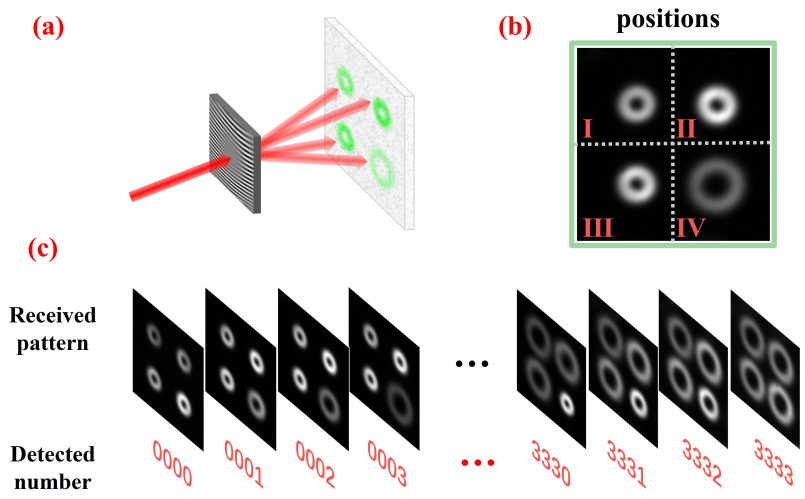

Figure 2.6: Schematics of the image transfer protocol employing an array of LG-correlated beams. (a) Schematic representation of the array generation. (b) The position of each intensity pattern in a 2×2 array. (c) The encoding/decoding sequence of 256 grey levels and 256 array states.

the RGGD. Conceptually, the idea of our multiplexing method stems from the spatial coherence radius modulation with the phase hologram realizing the transformation of Eq. (2.3). By adjusting the periods of the linear grating $t_{\mathrm{g}}(x, y)$, we can steer each beamlet of the array to a distinct spatial location as is visualized in Fig. 2.6(a). Thus, we are able to control the spatial coherence radius of any beamlet within the array. Inspired by [136], we can then jointly control the coherence radius and spatial location of the beamlet with the aid of a single hologram that performs a cumulative phase Φ_{M} transformation viz., $\Phi_M = \sum_{j=1}^{M} \Phi_j$, where Φ_j is given by Eq. (2.3) with f_j, u_j and v_j corresponding to the jth state. By introducing the space dimension into the encoding protocol, we greatly increase the number of available encoded states. Indeed, in the protocol sketched in Fig. 2.6, we engage 4 coherence state channels which correspond to four sources of variable coherence radius according to the rule: 0 is $\sigma_c = 0.05$mm, 1 is $\sigma_c = 0.03$mm, 2 is $\sigma_c = 0.025$mm, 3 is $\sigma_c = 0.02$mm. We multiplex each coherence state channel with 4 position channels (I, II, III, IV), yielding $4^4 = 256$ states (0000, 0001, 0002 ... 3332, 3333). The transmitted image is a large-scale, grey Lena image of 100×100 pixel resolution corresponding to 256 grey levels (0-255). In this experiment, the grey level value of each pixel is represented by a single array of LG-correlated beams. After having propagated over a stretch of free

space, the array intensity patterns are recorded by the CCD camera and mapped into the grey value diagram by ResNet 34. Finally, we compare the decoded and encoded grey-level information to ascertain the transmission fidelity to be 99.99%, see Fig. 2.7.

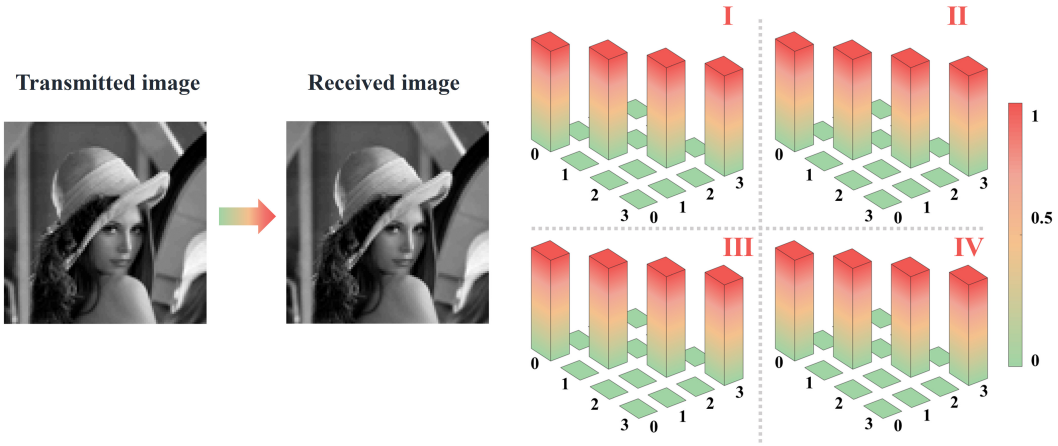

Figure 2.7: Qualitative (visual) and quantitative (fidelity) comparison between transmitted and received images. The color bar shows normalized fidelity with unity corresponding to 100%.

2.4 Conclusion

We have theoretically proposed and experimentally implemented a free-space optical communication protocol enabling high-fidelity transfer of a desired image or a set of images through, in general, a noisy communication channel. The key novelty of the proposed protocol is the fusion of random source structuring at the transmitter end and the employment of a deep learning network at the receiver end. The structuring of random source makes it possible to tap into multiple hitherto unexplored DoFs for image encoding, including the two that have been explicitly demonstrated to yield high-fidelity information transfer: the coherence structure of the source and the source coherence radius. In addition, using structured random light ensures resilience of the transmitted image to channel noise such as medium turbulence or the presence of solid obstacles in the light propagation path. The high-fidelity of our protocol is achieved due to two factors. First, the structured random light is robust against random perturbations in the medium. Second and most important, the deep learning

network, which we employ for image decoding, enables extremely accurate image recognition in a time efficient manner.

We have demonstrated the capability of our protocol for multiple DoF multiplexing to enhance communication capacity. In particular, we have shown how to multiplex the source coherence radius DoF with that of a spatial position of a beamlet within a random beam array carrying the image information. At the moment, our protocol is limited to relatively short propagation links in a noisy environment. We conjecture that the incorporation of dark/antidark beams on incoherent background, which are known to maintain the ring structure of their intensity profiles over tens of kilometers in weak, and hundreds of meters in strong atmospheric turbulence [95], into our protocol can significantly extend the operational range of the latter without compromising the fidelity of transmitted images.

2.5 Acknowledgement

This work was supported by National Key Research and Development Program of China (2022YFA1404800, 2019YFA0705000), National Natural Science Foundation of China (12192254, 92250304), China Scholarship Council (202108370219) and Natural Sciences and Engineering Research Council of Canada (RGPIN-2018-05497).

Chapter 3

Perfect correlation vortices

This chapter's work is published in the paper entitled "Perfect correlation vortices", Optics Letters 49(16), 4717-4720 (2024). The authors are Xiaofei Li, Sajjad Bashiri, Yuan Ma, Chuanhao Liang, Yangjian Cai, Sergey A. Ponomarenko and Zhiheng Xu. We introduce a class of random optical vortices, named perfect correlation vortices (PCV), with incredible resilience to strong atmospheric turbulence over modest propagation distances.

My contribution to this work includes performing the necessary analysis, and carrying out numerical simulations.

3.1 Introduction

A coherent optical vortex (OV) features a helical phase with the electromagnetic energy circulating around a vortex core which is a line of zero field intensity and indeterminate (singular) phase [137, 138]. The discovery of a fundamental link between any optical vortex and its orbital angular momentum [139] has triggered a flurry of research activity on OVs, culminating in numerous applications thereof to optical communications [140, 141], optical trapping and tweezing [142, 143], imaging [144], and even optical computing [145].

The phase singularity positions (intensity nulls) of a typical coherent OV strongly depend on the magnitude of the topological charge (TC) of the vortex [140, 146]. However, the so-called perfect vortex beams were introduced [147] and actively explored [148, 149] that alter this picture. The intensity profile of a realistic perfect vortex forms a thin ring of a radius nearly independent of the TC of the vortex [150]. Unfortunately, perfect vortices embedded into coherent optical fields quickly lose their vortex structure on free space propagation.

At the same time, random optical fields endowed with OVs have also been explored theoretically [151, 152, 153] and experimentally [154, 155]. As such partially coherent fields can carry OVs associated with their two-point spatial correlations [151, 152, 153], the term "coherence vortices" has been coined in Ref. [153]. Electromagnetic surface fields, such as random surface plasmon polaritons, can also be structured to possess correlation vortices [156]. In this context, reducing [157] or structuring [158] spatial coherence at the source was proposed to mitigate extreme susceptibility of perfect vortices to diffraction. Such perfect vortices wrapped into partially coherent fields remain intact over short propagation distances, but quickly succumb to diffraction afterwards. Thus, realizing prefect vortices that are resilient against diffraction over any desired propagation distance remains an open challenge.

In this part, we address this challenge by introducing a class of perfect correlation vortices (PCVs) that maintain their perfect vortex correlation rings on free space propagation. As a surprising bonus, the discovered PCVs are robust even against very strong atmospheric turbulence over moderate distances. In addition, the introduced PCVs are nearly immune to diffraction and are virtually statistically homogeneous in the low-coherence limit; their degree of coherence (DOC) is independent of the TC. All these remarkable features testify to the potential of such PCVs for free space optical communications which we will explore in due course.

3.2 Theory and numerical simulations

We start our search for PCVs by considering random sources endowed with OVs. The cross-spectral density of any bona-fide structured random source can be represented in the form [74]

$$W_0(\mathbf{r}_1, \mathbf{r}_2) = \int d\mathbf{k}\, p(\mathbf{k}) \Psi^*(\mathbf{r}_1, \mathbf{k}) \Psi(\mathbf{r}_2, \mathbf{k}). \tag{3.1}$$

Let us take the nonnegative power spectrum $p(\mathbf{k})$ to be a Gaussian

$$p(\mathbf{k}) = p(k) \propto e^{-k^2\sigma_c^2}, \qquad k \geq 0, \tag{3.2}$$

and examine an infinite set of vortex carrying modes of the form

$$\Psi(\mathbf{r}, \mathbf{k}) = \Psi_m^{(k)}(\mathbf{r}) = \sqrt{k} J_m(kr) e^{-r^2/2w_0^2} e^{im\phi}. \tag{3.3}$$

Here $J_m(x)$ is a Bessel function of the first kind and order m. It follows from Eqs. (3.1) through (3.3) by inspection with the aid of the table integral [159]

$$\int_0^\infty dx x J_m(ax) J_m(bx) e^{-cx^2} \propto \exp\left(-\frac{a^2+b^2}{4c}\right) I_m\left(\frac{ab}{2c}\right), \tag{3.4}$$

that the source cross-spectral density can be expressed, up to an irrelevant normalization constant, in a closed form as

$$\begin{aligned} W_0(\mathbf{r}_1, \mathbf{r}_2) &\propto e^{im(\phi_2-\phi_1)} \exp\left(-\frac{r_1^2+r_2^2}{2w_0^2}\right) \\ &\times \exp\left(-\frac{r_1^2+r_2^2}{4\sigma_c^2}\right) I_m\left(\frac{r_1 r_2}{2\sigma_c^2}\right). \end{aligned} \tag{3.5}$$

Here σ_c is related to the source coherence width as we will see shortly, and w_0 is a root mean square (rms) width of a Gaussian envelope. Further, $I_m(x)$ is a modified Bessel function of order m. We display the spatial intensity distribution $I(\mathbf{r}) = W(\mathbf{r}, \mathbf{r})$ of the source for variable m, which manifests intensity nulls on the optical axis for any $m \neq 0$, in Fig. 3.1(a). We choose the following parameters: $w_0 = 10$ cm, $\sigma_c = 1$ mm and the carrier wavelength $\lambda_0 = 532$ nm.

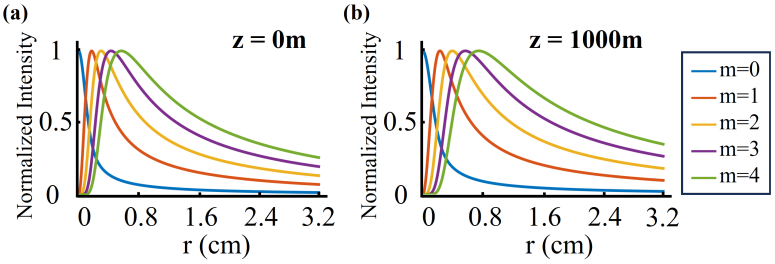

Figure 3.1: Intensity distribution (a) and its evolution on free space propagation (b) for PCVs of variable TC m. The parameters of the source are $w_0 = 10$ cm, $\sigma_c = 1$ mm, and $\lambda_0 = 532$ nm.

However, we are chiefly interested in the behavior of the DOC of the just presented source; the latter is defined as [60, 63]

$$\mu_0(\mathbf{r}_1, \mathbf{r}_2) = \frac{W_0(\mathbf{r}_1, \mathbf{r}_2)}{\sqrt{W_0(\mathbf{r}_1, \mathbf{r}_1) W_0(\mathbf{r}_2, \mathbf{r}_2)}}. \tag{3.6}$$

It follows at once from Eqs. (3.5) and 3.6) that

$$\mu_0(\mathbf{r}_1, \mathbf{r}_2) = e^{im(\phi_2-\phi_1)} \frac{I_m[r_1 r_2/(2\sigma_c^2)]}{\sqrt{I_m[r_1^2/(2\sigma_c^2)] I_m[r_2^2/(2\sigma_c^2)]}}. \tag{3.7}$$

The first glance at Eqs. (3.5) and (3.7) might lead to the conclusion that the introduced sources are closely related to the previously reported [151] modified-Bessel-correlated ones. Indeed, the cross-spectral densities and hence degrees of coherence of the two classes of sources have the same function form. Yet, careful inspection reveals that in the low-coherence regime, $\sigma_c \ll w_0$, the PCVs possess statistically homogeneous correlations of a perfect vortex type, while the modified-Bessel correlated sources are necessarily statistically inhomogeneous in any parameter regime. Mathematically, this fact is reflected in very different representations of PCVs and modified-Bessel-correlated sources in terms of Bessel and Laguerre-Gaussian modes, respectively.

To demonstrate that the DOC of Eq. (3.7) describes a PCV, we focus on a nearly incoherent limit, such that

$$\sigma_c \ll \sigma_{\text{eff}} \ll w_0, \quad \sigma_{\text{eff}} = \sqrt{\sigma_c w_0}. \tag{3.8}$$

Here σ_{eff} denotes a characteristic transverse spatial scale governing PCV diffraction, as we will see shortly. Next, introducing a dimensionless radial variable, $\overline{r} = r/\sigma_{\text{eff}}$, we can approximate $I_m(x) \simeq e^x$ in the incoherent limit (3.8). It then readily follows from Eq. (3.7) that relative to any reference point $\mathbf{r}_0$ the source correlations are homogeneous, given by

$$\mu_0(\overline{\mathbf{r}}, \overline{\mathbf{r}}_0) \simeq e^{im(\phi-\phi_0)} \exp\left[-\frac{(\overline{r}-\overline{r}_0)^2}{4\delta_0^2}\right], \tag{3.9}$$

where $\overline{r}_0 = r_0/\sigma_{\text{eff}}$ and $\delta_0 = \sqrt{\sigma_c/w_0} \ll 1$ is a very narrow width of source correlations in dimensionless variables; in other words, the two-point correlations of the source field endowed with a helical wavefront are only significant over a very narrow circular ring, regardless of the topologicals charge of the vortex. Therefore, Eq. (3.9) describes a perfect correlation vortex. Note that $\overline{r}$ in the $\sqrt{x}$ factor in the asymptotic expansion of $I_m(x)$ can be replaced with $\overline{r}_0$ because $\sqrt{x}$ does not appreciably change over the ring width compared to e^x.

Next, we examine free-space evolution of PCVs. Using the vortex modes of Eq. (3.3), we can write for the cross-spectral density in any transverse plane, $z = const \geq 0$,

$$W(\mathbf{r}_1, \mathbf{r}_2, z) = \int_0^\infty dk e^{-k^2\sigma_c^2} \Psi_m^{(k)*}(\mathbf{r}_1, z) \Psi_m^{(k)}(\mathbf{r}_2, z), \tag{3.10}$$

where the mode evolution is governed, in paraxial approximation, by the following Fresnel transform:

$$\Psi_m^{(k)}(\mathbf{r},z)=\left(\frac{k_0}{2\pi iz}\right)\int d\mathbf{r}'\Psi_m^{(k)}(\mathbf{r}',0)\exp\left[\frac{ik_0(\mathbf{r}-\mathbf{r}')^2}{2z}\right]. \tag{3.11}$$

Here $k_0=2\pi/\lambda_0$. On substituting from Eqs. (3.3) and (3.11) into (3.10), we obtain, after somewhat lengthy algebra employing the integral (3.4), for the cross-spectral density the expression (derived in Appendix B)

$$\begin{aligned}W(\mathbf{r}_1,\mathbf{r}_2,z)\propto&\frac{e^{im(\phi_2-\phi_1)}}{(1+z^2/L_d^2)}\exp\left[\frac{i(r_2^2-r_1^2)}{2(\sigma_c^2L_R/z+w_0^2z/L_R)}\right]\\&\times\exp\left[-\frac{(r_1^2+r_2^2)}{2w_0^2(1+z^2/L_R^2)(1+z^2/L_d^2)}\right]\\&\times\exp\left[-\frac{(r_1^2+r_2^2)}{4\sigma_c^2(1+z^2/L_d^2)}\right]I_m\left[\frac{r_1r_2}{2\sigma_c^2(1+z^2/L_d^2)}\right].\end{aligned} \tag{3.12}$$

Here $L_R=k_0w_0^2$ is a Rayleigh range associated with the envelope width w_0 and $L_d=k_0\sigma_cw_0$ is a characteristic diffraction length of a PCV, which justifies our interpretation of σ_{eff} immediately following Eq. (3.8). Notice that in the chosen parameter regime, $L_d\ll L_R$.

A few instructive observations are in order at this point. First, it follows from Eq. (3.12) that the PCV field structure is invariant on free-space propagation, making PCVs a subclass of a larger class of vortex preserving partially coherent fields whose general theory was developed in [160]. Second, the spatial intensity distribution of the PCV, which we display in Fig. 3.1(b), is nearly diffraction free in the chosen parameter regime. At first glance, one might find this result surprising as the cross-spectral density of Eq. (3.12) is not of the form of a bump/dip atop of a statistically uniform background which would guarantee propagation invariance in general [94]. However, we can show that provided $\sigma_c\ll w_0$, the source cross-spectral density can be approximated, apart from a helical phase factor, by a product of a very wide Gaussian envelope and a uniform Gaussian correlation function of width σ_c. It follows that over distances of the order of $L_d\sim 1$ km, the field generated by such a source outside of the vortex core region behaves as a partially coherent plane wave, which is essentially immune to diffraction. We note also that the dependence of the diffraction length of PCVs on the product of their coherence width and soft aperture size is typical of enveloped diffraction-free random beams [161].

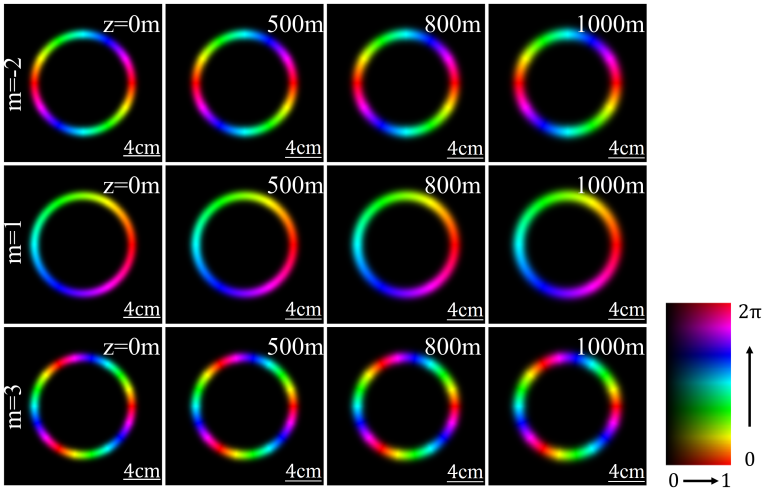

Figure 3.2: Evolution of the magnitude and phase (hue) of the DOC of a PCV, given by Eq. (3.14), with the propagation distance. The source parameters are $w_0 = 10$ cm, $\sigma_c = 1$ mm, $r_0 = 2$ cm, and $\lambda_0 = 532$ nm.

Next, the DOC of a PCV in any transverse plane is defined as

$$\mu(\mathbf{r}_1, \mathbf{r}_2, z) = \frac{W(\mathbf{r}_1, \mathbf{r}_2, z)}{\sqrt{W(\mathbf{r}_1, \mathbf{r}_1, z) W(\mathbf{r}_2, \mathbf{r}_2, z)}}. \tag{3.13}$$

It follows at once from Eqs. (3.12) and (3.13) that

$$\mu_{\text{exact}}(\mathbf{r}, \mathbf{r}_0, z) = \frac{I_m\left[\frac{r r_0}{2\sigma_c^2(1+z^2/L_d^2)}\right] e^{im(\phi-\phi_0)}}{\sqrt{I_m\left[\frac{r^2}{2\sigma_c^2(1+z^2/L_d^2)}\right] I_m\left[\frac{r_0^2}{2\sigma_c^2(1+z^2/L_d^2)}\right]}}. \tag{3.14}$$

We exhibit the DOC evolution, obeying Eq. (3.14), over a kilometer long distance in free space in Fig. 3.2; we show both the magnitude and phase evolution with z choosing the same parameters as before and the reference point to be at $r_0 = 2$ cm. We can infer from the figure that both the DOC magnitude and phase, shown with hue, remain nearly intact, thereby attesting to PCV robustness to diffraction.

We now derive a simple and elegant approximate expression for the PCV DOC, which is valid in any transverse plane $z \geq 0$, and demonstrate its accuracy. To this end, we infer from Eq. (3.12) that provided $z \lesssim L_d$, the vortex ring of the DOC remains narrow enough so that by approximating the modified Bessel function with an exponential, we obtain in dimensionless variables the expression

$$\mu(\overline{\mathbf{r}}, \overline{\mathbf{r}}_0, z) \simeq e^{im(\phi-\phi_0)} \exp\left[-\frac{(\overline{r}-\overline{r}_0)^2}{4\delta^2(z)}\right], \tag{3.15}$$

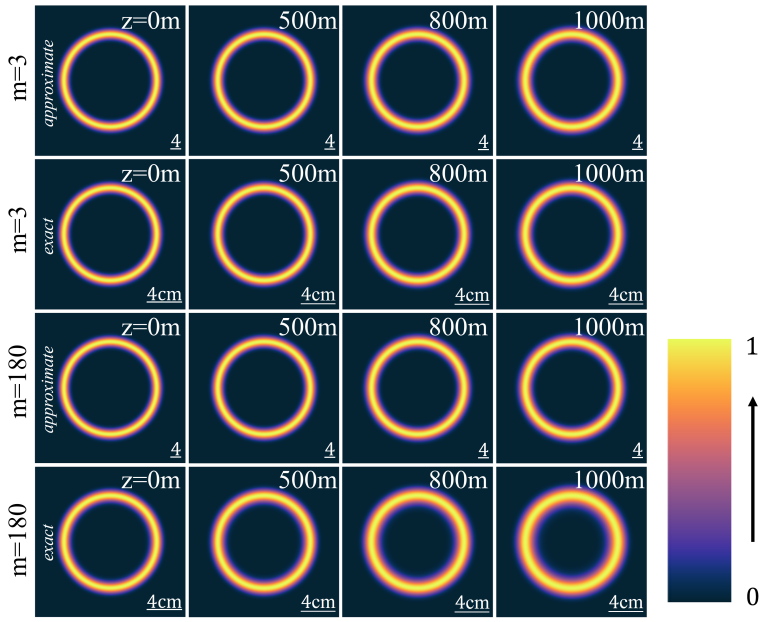

Figure 3.3: Comparing the magnitude of DOC evolution obtained from the exact expression, Eq. (3.14) and the corresponding Gaussian approximation, Eq. (3.15) with z over a kilometer-long stretch of free space. The source parameters are $w_0 = 10$ cm, $\sigma_c = 1$ mm, $r_0 = 2$ cm, and $\lambda_0 = 532$ nm.

where

$$\delta(z) = \delta_0 \sqrt{1 + z^2/L_d^2}, \tag{3.16}$$

is a width of the PCV ring at a distance z; Eq. (3.15) indicates that the PCV remains statistically homogeneous within the paraxial propagation regime. Eqs. (3.15) and (3.16) are the key result of this work; they provide a universal, as expressed in dimensionless variables, and application friendly description of field correlations of an ideal PCV. To verify the accuracy of this approximation, we display the magnitude of the DOC obtained with the aid of Eq. (3.14) and that given by the approximate equation, Eq. (3.15) in Fig. 3.3. The top two rows juxtapose the exact and approximate $|\mu|$ for a moderate value of the TC $m = 3$, while the bottom two rows do the same for large m, $m = 180$. We can readily infer from the figure that there is excellent agreement between the exact and approximate expressions for $|\mu|$ with moderate TCs. We also observe in the figure that as the magnitude of the TC increases, the ring radius, but not the circular shape, starts deviating from that of the ideal PCV; the deviation becomes progressively noticeable as the PCV propagates farther away

from the source.

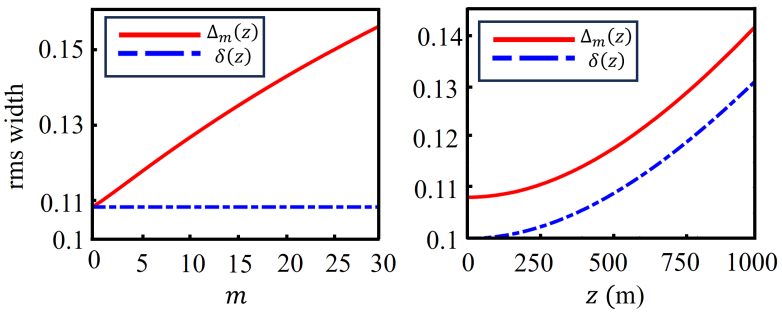

Figure 3.4: Comparison of the widths of an ideal PCV ring δ with that determined from the rms width of the exact DOC profile Δ_m. Left: Δ_m and δ as functions of m at $z = 500$ m. Right: δ and Δ_m as functions of the propagation distance z for $m = 5$.

To assess the discrepancy quantitatively, we evaluate the (dimensionless) rms width Δ_m of the PCV field correlations which we define by the expression

$$\Delta_m^2(z) = \frac{\int_0^\infty d\overline{r} \int_0^\infty d\overline{r}_0 |\mu_{\text{exact}}(\overline{r}, \overline{r}_0)|^2 (\overline{r} - \overline{r}_0)^2}{\int_0^\infty d\overline{r} \int_0^\infty d\overline{r}_0 |\mu_{\text{exact}}(\overline{r}, \overline{r}_0)|^2}, \tag{3.17}$$

where we employed the exact DOC given by Eq. (3.14) and expressed in dimensionless variables. In Fig. 3.4, we compare thus defined Δ_m with δ, evaluated at the source for variable topological charge m. We also display δ and Δ_m for $m = 5$ as functions of the propagation distance z. It follows from Fig. 3.4 (a) that the correlation width does increase with m and the ideal PCV expression, Eq. (3.16) yields an appreciable error, around 30% for m corresponding to a double digit number. At the same time, Fig. 3.4 (b) attests to the fact that the magnitudes of Δ_m and δ remain quite close over substantial distances as long as m is not too large.

Finally, we demonstrate that the vortex ring structure of the discovered PCVs can be robust even against strong atmospheric turbulence, at least, over relatively short distances. To this end, we display in Fig. 3.5 the results of our numerical simulations for the evolution of the magnitude of the DOC of PCV field through atmospheric turbulence with the structure constant such that $C_n^2 = 10^{-13}$ m$^{-2/3}$, which allows us to classify such turbulence as strong [162]. We employ a random phase screen method; the details of our numerical procedure can be found in [95]. We infer from the figure that, remarkably, the main correlation ring of the PCV with $m = 1, -2, 3$, which we have considered here, survives the turbulence rather well; similar results hold for

PCVs with other TCs. At the same time, the contrast between the dark areas inside and outside the vortex ring on the one hand, and the bright area within the ring on the other, diminishes due to turbulence. We note, though, that the additional pseudo-rings, visible in all panels, are an artefact of our using a Matlab random number generator. We also verified numerically that the orbital angular momentum spectrum of any PCV in Fig. 3.5 is sharply peaked around the corresponding topological charge over the entire propagation stretch. Finally, we notice that the axial symmetry of the magnitude of the source DOC breaks down on PCV propagation through atmospheric turbulence which becomes evident if we compare panels at $z = 0$ with those at $z = 75$ m, or $z = 150$ m. The resilience of the PCV ring to atmospheric turbulence is most consequential for the PCV potential for free-space optical communications.

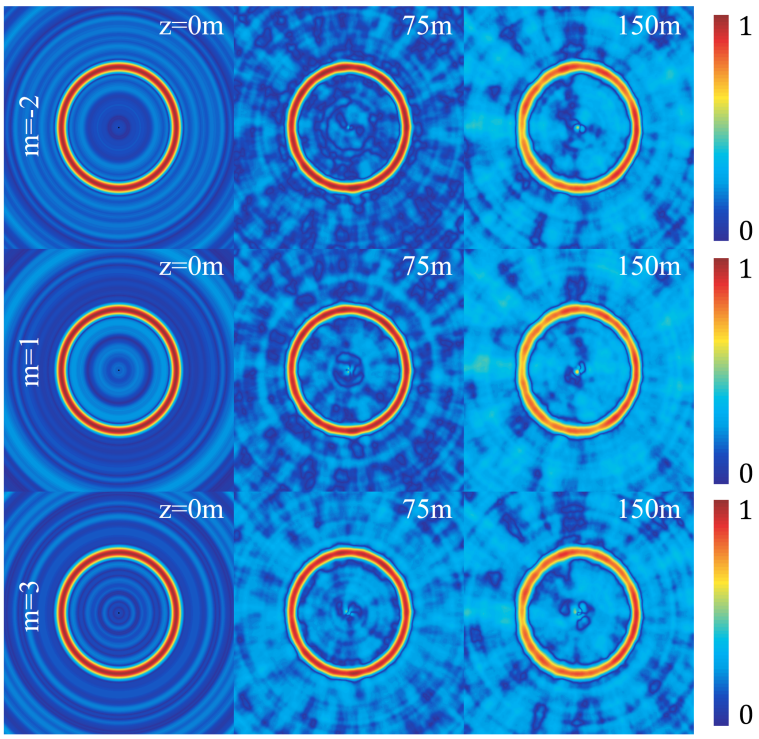

Figure 3.5: Evolution of the magnitude of PCV DOC through a 150 m long stretch of the turbulence atmosphere with the structure constant C_n, $C_n^2 = 10^{-13}$ m$^{-2/3}$. The source parameters are $w_0 = 10$ cm, $\sigma_c = 1$ mm, and $\lambda_0 = 532$ nm. The reference point corresponds to $r_0 = 2$ cm and $\phi_0 = 0$.

3.3 Conclusion

In conclusion, we have introduced a class of random vortices, perfect correlation vortices, with the DOC at the source manifesting a thin ring of the radius and thickness independent of the topological charge of the vortex. The discovered PCVs are nearly statistically homogeneous across the source and remain so on paraxial propagation in free space. Thus unlike their fully coherent counterparts, PCVs can maintain their vortex structure in free space essentially indefinitely. In addition, PCVs are resilient to even strong atmospheric turbulence, albeit over sufficiently short distances. We have derived an elegant, closed form analytical expression for the degree of coherence of a perfect correlation vortex in any transverse plane. We anticipate the discovered vortices to facilitate free space optical communications, among other potential applications.

3.4 Acknowledgement

This work is supported by National Key Research and Development Program of China (2022YFA1404800, 2019YFA0705000); National Natural Science Foundation of China (12192254, 92250304, 12374311); Natural Sciences & Engineering Research Council (NSERC) of Canada (RGPIN-2018-05497).

Chapter 4

Multi-function vortex array radar

This chapter's work has been submitted to Applied Physics Letters in the paper entitled "Multi-function vortex array radar". The authors are Xiaofei Li, Sajjad Bashiri, Vasilisa Ponomarenko, Yu Wang, Yangjian Cai and Sergey A. Ponomarenko. We propose a promising protocol that integrates efficient data processing methods with robust hardware for real-time detection, positioning, and tracking of moving targets, while extending its utility to serve as a topographic laser profiling system for geographic environments, highlighting its adaptability to varied scenarios.

My contribution to this work includes conceiving the idea, performing formal analysis, analyzing methodology, and writing original draft.

4.1 Introduction

Radar systems, with their ability to detect and track objects by transmitting electromagnetic waves and analyzing their reflections, play an important rolein various fields [163, 164], including weather monitoring [165, 166], autonomous navigation [167], and remote sensing [168]. However, the emerging applications demand radar system capable of simultaneously performing several tasks. For example, automation systems for self-driving vehicles rely heavily on abundant detected information. A reliable automation system should support real-time decisions and responses, necessitating the radar systems that can synchronize multiple missions, such as ranging, positioning, and speed estimation within a single imaging protocol. As a response to this challenge, the concept of multi-function radar (MFR) has emerged [169], which focuses on a primary mission while handling secondary tasks, thereby significantly enhancing the value of the obtained information.

To meet multiple requirements, the effective management of limited radar resources to accomplish multiple tasks of scheduling time, energy, and computational resources for each task presents the primary challenge in multi-function radar system

design [170]. Various resource management schemes have been explored to enhance the performance of MFR for different tasks. Hardware-based schemes can provide services for both aircraft and weather surveillance [171, 165], and can also perform single target tracking and classification [172]. Furthermore, protocols involving data processing algorithms can handle multiple target tracking [173], people counting and motion recognition [174], as well as the detection and tracking of pedestrians and vehicles [175]. Although hardware-based resource management demonstrates robust performance and efficiency, integrating new hardware components with the existing systems can be complex, time-consuming and costly [176]. On the other hand, signal processing methods optimize the use of resources and offer flexibility in various scenarios with crucial adaptability, particularly for the gradually integrating miniaturized radars [177]. Therefore, considering the balance of these aspects for innovative management, a compromise scheme that incorporates the benefits of both hardware-based and signal processing methods is required.

During this decade, advancements in radar technology have been primarily driven by a compromise technology, the signal modulation for subsequent detection. One remarkable development is the incorporation of Orbital Angular Momentum (OAM) of light into radar systems, where OAM arises due to a helical wavefront $exp(il\theta)$ of the optical field [139]. By using electromagnetic wave modulated by OAM, the radar system can significantly improve image resolution and collect more information about the target [39, 40], even in low signal-to-noise ratio (SNR) environments [178]. Additionally, research reports indicate that OAM carries great promise for estimating target velocities [179] and enabling 3D imaging [180]. Simultaneously, investigations into data processing algorithms for vortex radar are ongoing [181]. These advancements exemplify transformative potential of OAM in MFR systems.

In this work, we introduce a task management protocol for MFR by combining phase-array vortex modulation and laser radar technologies. We employ an optical vortex array for signal detection and an appropriate data processing approach to synchronize imaging, positioning, and velocity estimation. Our study presents a comprehensive imaging scheme for 2-dimensional (2D) targets, demonstrating how Poynting vector flow and power calculations of the total image field facilitate the determination of azimuth and radial position of the target. Furthermore, we extend

the proposed protocol to include topographic applications by developing an imaging scenario for 3-dimensional (3D) targets. These findings illustrate the capacity of our protocol for hardware-based management and data processing that widen the scope of MFR system applications.

4.2 Imaging and positioning process for 2D target

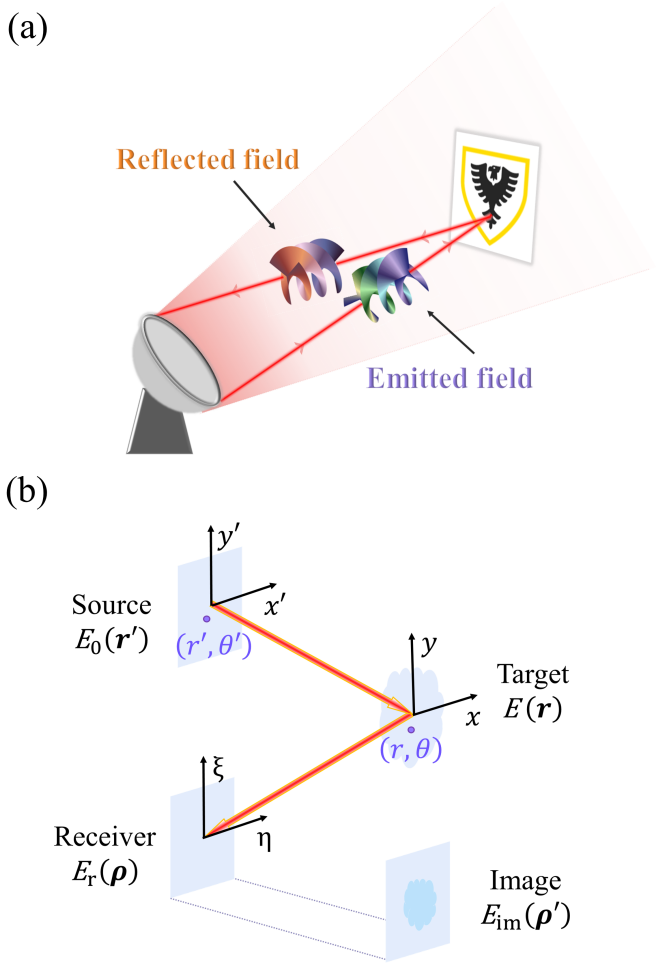

Figure 4.1: Concept (a) and protocol schematics (b) of vortex MFR.

We sketch the vortex MFR geometry and schematic diagram of our protocol in Fig. 4.1. The source field $E_0(\mathbf{r}')$ of the radar is emitted into free space and reaches the target plane after free-space propagation. The electrical field $E(\mathbf{r})$ arriving at the

target plane can be expressed, in the paraxial approximation, by the Fresnel integral

$$E\left(\mathbf{r}\right) \propto \int d\mathbf{r}'\, E_0\left(\mathbf{r}'\right) \exp\left[\frac{ik(\mathbf{r}-\mathbf{r}')^2}{2z}\right]. \tag{4.1}$$

The source field in our protocol is generated by a vortex beam array. We produce the array from an input Gaussian laser beam illuminating a phased-modulation element, such as a spatial light modulator (SLM), say, loaded with a customized set of holograms. We assume that the coordinates of a point $\mathbf{r}'$ in the SLM plane are represented by (x', y'). To generate the source field $E_0\left(x', y'\right)$, we endow the field of the input Gaussian beam with the phase

$$\sum_{n=1}^{N} \exp\left[-\frac{ik}{f}\left(x_n x' + y_n y'\right)\right] \exp\left(il\theta'\right). \tag{4.2}$$

Here N is a total number of identical optical vortices (OV) with the topological charge l composing the array. All vortices are located at the vertices of a regular N-sided polygon inscribed into a circle of radius r_n. The center of the circle marks the array center with Cartesian coordinates (x_c, y_c). The nth OV within the array is situated at the point with coordinates $x_n = r_n \cos\theta_n + x_c$ and $y_n = r_n \sin\theta_n + y_c$, where $\theta_n = 2\pi n/N$. We sketch the vortex array geometry in Fig. 4.2(a). The gauge transformation of Eq. (4.2) allows us to shift the overall array or individual vortices within the array via phase modulation realized with the aid of a thin lens of focal length f.

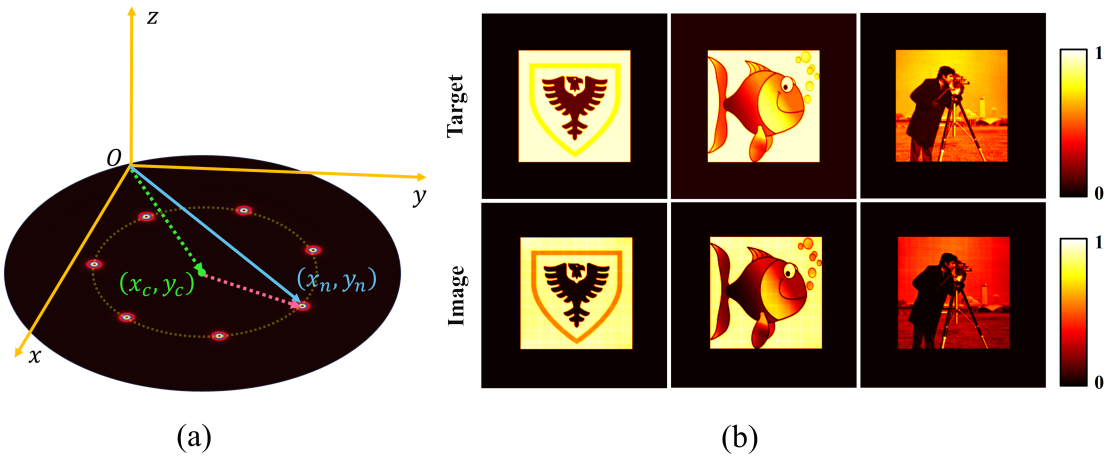

Figure 4.2: Geometry of the vortex array (a) and recovered images (b).

The radar operates as follows. First the source field, having reached the target, is reflected back to the source/receiver along a straight-line path. The reflected field $E_{\mathrm{r}}(\boldsymbol{\rho})$ registered by the receiver then reads

$$E_{\mathrm{r}}(\boldsymbol{\rho}) \propto \int d\mathbf{r}\, E(\mathbf{r})\, O(\mathbf{r}) \exp\left[\frac{ik(\boldsymbol{\rho}-\mathbf{r})^2}{2z}\right], \tag{4.3}$$

where $O(\mathbf{r})$ is an aperture function of the target. Second, we obtain the image field $E_{\mathrm{im}}(\boldsymbol{\rho}')$ via a Fourier transformation of the received one using the lens of focal length f as [182]

$$E_{\mathrm{im}}(\boldsymbol{\rho}') \propto \int d\boldsymbol{\rho}\, E_{\mathrm{r}}(\boldsymbol{\rho}) \exp\left(\frac{-ik\boldsymbol{\rho}\cdot\boldsymbol{\rho}'}{f}\right). \tag{4.4}$$

To showcase the performance of our protocol, we present several recovered images of variable texture, complexity and grayscale range, including the logo of Dalhousie and two standard test images: Happyfish and Cameraman. We model these grayscale images (from 0 to 255) as 2D targets $O(\mathbf{r})$ with normalized grey levels used as reflection coefficient indicators. Hereafter we consider vortex arrays comprised of nine OVs with $l = 2$, placed on the ring of radius $r_n = 4.5$ mm. Further, we first assume an ideal scenario whereby the radar precisely locks onto the target, so that the center of the vortex array is perfectly aligned with the target center. The target is located 1500 m away from the source. By utilizing Eqs. 4.1 through 4.4, we display the target images in Fig. 4.2(b). Good resemblance between the objects and images points to excellent accuracy of our MFR protocol in this idealized situation.

In general, however, the array and target centers are misaligned, resulting in poor image quality and scarce resemblance of the image to the target, especially for moving targets. Hence, precise target position acquisition, which must incorporate accurate orientation information, is crucial to achieve optimal imaging results. The MFR is expected to extract additional implicit information from the image plane, which can effectively guide the system to accurately track a moving target, at least, as far as providing azimuth or radial references for the subsequent detection procedure is concerned. To realize this idea within our MFR, we carried out further simulations.

The target position acquisition procedure involves extracting information about a relative position of the array and target centers. To this end, we start by setting up our polar coordinate system in the target plane, with the array center serving as the

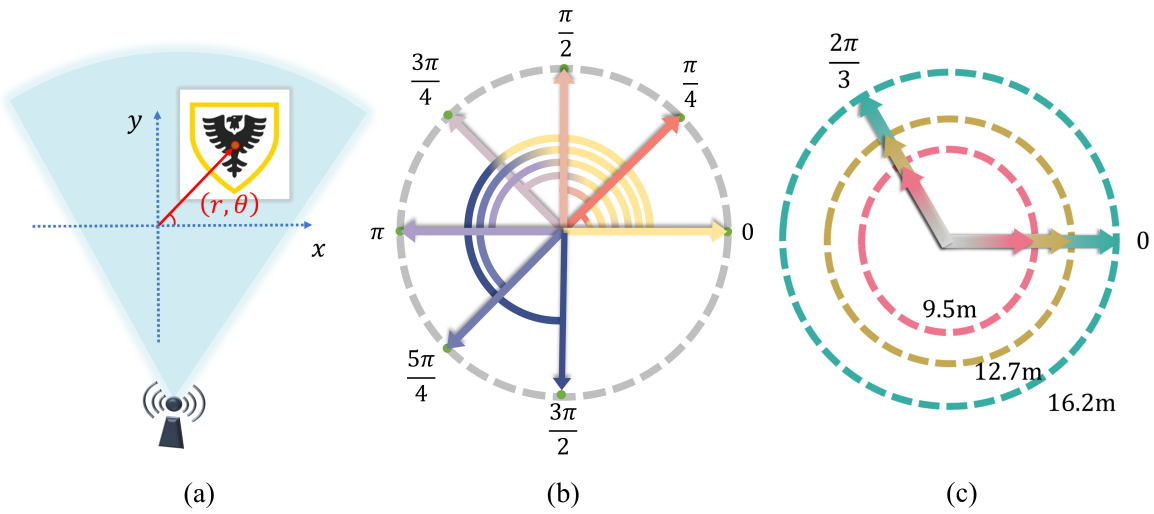

Figure 4.3: Target acquisition of the proposed vortex MFR (a) with variable azimuth (b) and relative radial position of the array and target centers (b).

origin. The target center, marked by a red solid point, is located at a point with the radius vector $\boldsymbol{r} = (r, \theta)$ (see Fig. 4.3(a)). Adjusting (r, θ), we can control the relative position of the two centers, thereby enabling target movement tracking. The target acquisition process entails detecting the azimuthal angles (Fig. 4.3(b)) and radial distances (Fig. 4.3(c)) of the relative position vector. Our primary goal is to determine θ of the target center relative to $x-$ axis. As depicted in Fig. 4.3(b), we evaluate misalignment for seven different angles separated by the same interval of $\pi/4$ at a fixed relative radius of $r = 16$ m. Repeating the tracking protocol yields the results shown in Fig. 4.4(b)-(h). For better comparison, we also display the "perfect" case with the aligned array and target centers in Fig. 4.4(a). As anticipated, due to the source-target misalignment, we can observe image distortions, which are related to azimuthal misalignment. These results further highlight the importance of optimal array positioning to attain optimal image quality. To obtain the azimuth direction of the relative position of the target relative to the array center, we evaluate the Poynting vector of the imaged electromagnetic field. [139] The former yields us the direction of electromagnetic energy flow and is defined as $\vec{S}_{\perp}=\vec{S}_x+\vec{S}_y = \frac{i}{4\eta_0 k}\left(E_{im}\vec{\nabla}_{\perp}E^*_{im} - E^*_{im}\vec{\nabla}_{\perp}E_{im}\right)$. We exhibit the transverse power flow distributions for each case in Fig. 4.4 (b)-(h) by the arrows. We can infer from the figure that the power flow direction is affected by the relative azimuth, indicating that the flow distribution determines the azimuth

direction, which facilitates target tracking. For instance, when the target center is located at (16 m, $\pi/4$), the energy flow direction aligns with the angle the target center makes with $x-$axis (see Fig. 4.4(c)). In the perfect alignment situation, however, a perfect image can be acquired, which is characterized by a nearly isotropic energy flow (see Fig. 4.4(a)).

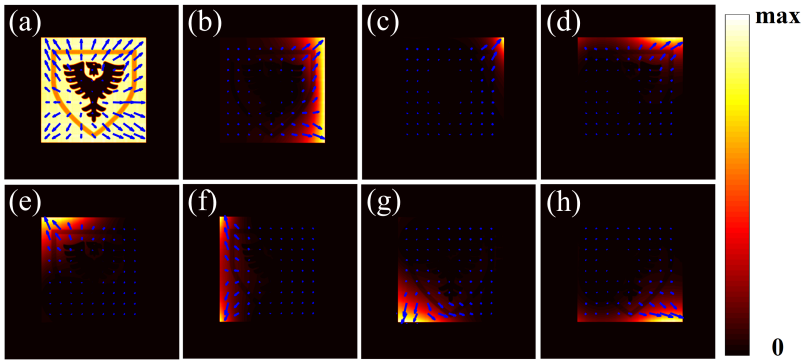

Figure 4.4: Recovered image and the corresponding transverse power flow distributions for a variable azimuth.

In addition, we aim to determine the radial distance r between the target and array centers. As is illustrated in Fig. 4.3(c), we consider six cases featuring three different radii (r = 9.5 m, 12.7 m, 16.2 m) across two azimuthal directions, 0 and $2\pi/3$. We display the corresponding images and the corresponding transverse power flow distributions (indicated by arrows) in Fig. 4.5. Fig. 4.5(a)-(f) support the earlier conclusions regarding the role of the source-target azimuth for correct target acquisition. However, the flow distribution in the case of partially recovered images only specifies the azimuth direction and does not provide any valid information about the radial position of the target. Therefore, to determine the distance to the target, we work out the total power carried by the image field as $P = \int d\boldsymbol{\rho}' I_{im}(\boldsymbol{\rho}')$. To study the dependence of the total power P on relative distance r further, we examine the total power as a function of the radial distance between the centers for two azimuth directions, 0 and $2\pi/3$ and display it in panels (g) and (h) of Fig. 4.5. It follows that as the source-target distance gradually increases, so does the total power, although the power growth is non-uniform across different radii. Moreover, a comparison of the two panels indicates that the power growth is affected by the azimuth. In the short distance range (0 m-15 m), the power flow slightly increases with the distance

and only marginally depends on the azimuth. As the radial distance between the centers reaches the range (15 m-20 m), though, the power growth rate difference in the two directions becomes noticeable. This observation highlights a nuanced interplay between the azimuth direction and the power evolution as a function of the radial separation distance. Ultimately, this dependence ascertains the magnitude of the radial separation between the target and array centers, allowing the radar system to accurately locate the target during each scan.

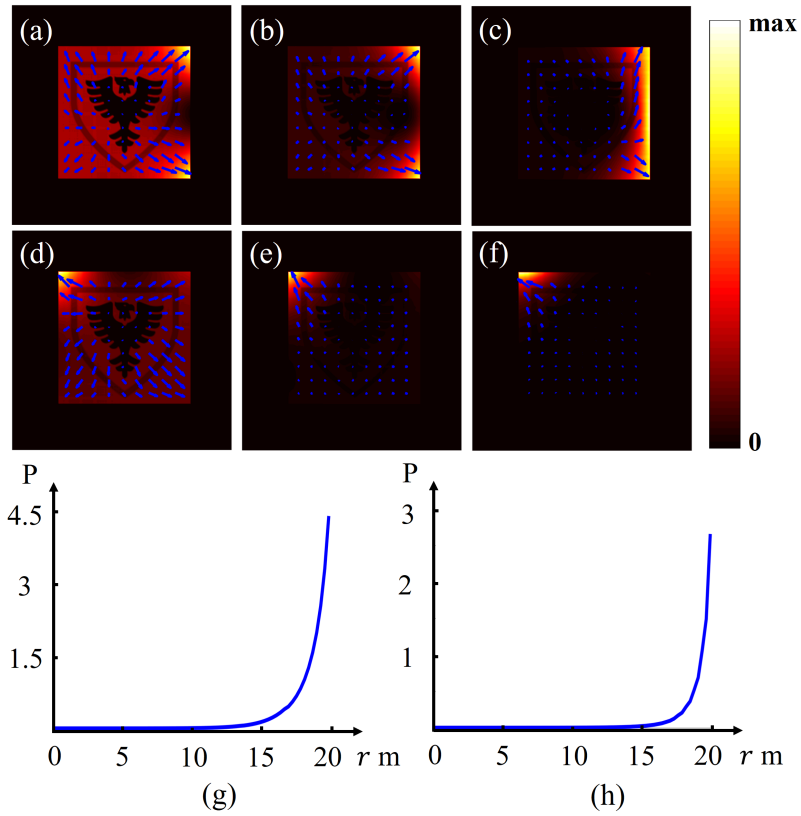

Figure 4.5: Recovered images and the corresponding transverse power flow distributions for a variable array-target separation distance 9.5 m, 12.7 m, 16.2 m in directions corresponding to the angles 0 (a)-(c) and $2\pi/3$ (d)-(f). Power curves versus the separation distance r for azimuthal directions 0 (g) and $2\pi/3$ (h), respectively.

To summarize, we can complete the target acquisition process in two consecutive steps. First, we determine the azimuth of the target by evaluating the Poynting vector flow. Second, we elucidate the corresponding radial distance from the array to the target center by analyzing the total power associated with said azimuth. Consequently, we can extract the crucial target orientation information through the analysis of the

power distribution of the received field. Moreover, we can also estimate the velocity of a moving target. By comparing the power curves of two consecutive scans, we can infer the distance the target has travelled between the scans, thereby estimating its velocity for subsequent tracking.

4.3 Topography profiling process

Our simulations indicate that the peak intensity of the 2D image field is moderately influenced by the distance to the target. We can then acquire a 3D image by figuring out the distance to each point on the target surface and accumulating these distance measurements to construct a point cloud representation of the target (as depicted in Fig. 4.6(a)). Notably, laser radar systems have the capability to directly assess the landscape while circumnavigating geometric distortion issues [183, 184]. In this connection, one might wonder whether the proposed MFR protocol is capable of 3D imaging and sensing. Hence, we explore the potential of our protocol for topographic laser profiling.

To this end, we exhibit a 3D landscape in Fig. 4.6(a), together with the results of its reconstruction within our protocol. We assume, for simplicity, that the reflectivity index of the mountain surface is unity, $O\left(x,y\right)=1$. As is seen in Fig. 4.6(b), we denote the height at the point in the ith column and jth row of a matrix representation (x_i,y_j) of the target surface by h_{ij} and place a light source a distance d above the ground. Further, we denote the detection distance from the source to each point by z_{ij}. We can then write down the electrical field $E\left(x_i,y_j\right)$ at each point on the terrain surface in terms of the Fresnel integral as

$$\mathbf{E}\left(x_i,y_j\right)\propto\int d\mathbf{r}'\mathbf{E}_0(\mathbf{r}')\exp\left\{\frac{ik[(x_i-x')^2+(y_j-y')^2]}{2z_{ij}}\right\}. \tag{4.5}$$

The field of the echo signal at the receiver then reads

$$\mathbf{E}_r(\xi_i,\eta_j)\propto\int d\mathbf{r}\mathbf{E}\left(\mathbf{r}\right)O(\mathbf{r})\exp\left\{\frac{ik\left[(\xi_i-x)^2\right]}{2z_{ij}}\right\}\exp\left\{\frac{ik\left[(\eta_j-y)^2\right]}{2z_{ij}}\right\}. \tag{4.6}$$

By utilizing Eqs.(4.5) and (4.6), we map the terrain features of two modeled target landscapes as displayed in Fig. 4.6(c). The two examples we provide have different terrain distributions and altitude maxima. In the left column, the source is located at a distance $d=3270$ m, whereas in the right one, it is placed $d=3570$ m away from the

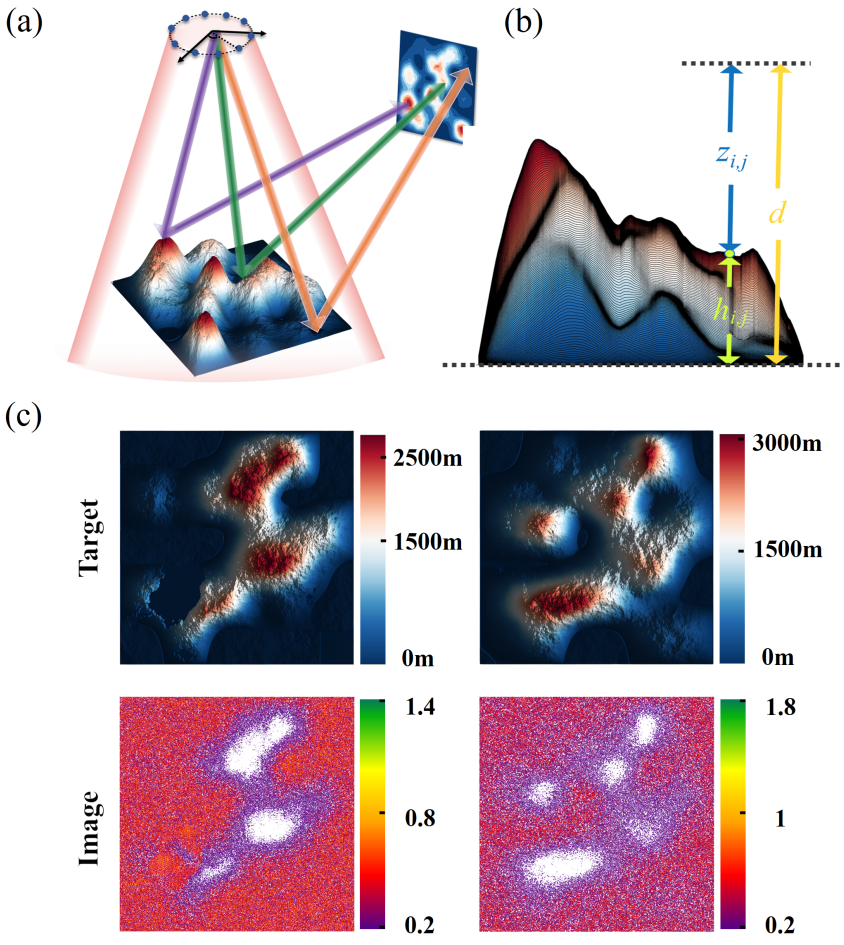

Figure 4.6: 3D and 2D views of the schematics of the terrain profiling process.

ground. The comparison of the target and image landscapes reveals that the generated 2D contour patterns derived from the point clouds closely match the visual depiction of the terrains in 2D view. The similarity between the reconstructed patterns and the actual landscapes highlights the efficacy of our protocol in translating point cloud data into meaningful 2D landscape representations. On comparing the two columns of Fig. 4.6(c), we observe that the maximum image intensity is indeed related to the altitude range of the original target. These results underscore the versatility and adaptability of our protocol, indicating its potential to address a wider range of scenarios beyond the current context.

4.4 Conclusion

In conclusion, we have introduced and illustrated a protocol realizing a multi-function radar employing an optical vortex array. Our protocol integrates the benefits of both hardware-based management and signal processing methods to enable potentially flexible deployment in miniaturized hardware configurations. Further, our protocol manifests a high level of versatility, enabling multiple functions such as imaging, as well as moving target tracking and identification. Moreover, the protocol utility extends to topographic laser profiling for comprehensive evaluation of 3D landscapes, further highlighting its remarkable adaptability. The versatility and adaptability of our protocol carry promise for even further extensions to such sophisticated, cutting edge applications as self-driving vehicles. Currently our protocol is limited by its inability to obtain highly accurate angle measurements, providing only an approximate azimuth. We conjecture that optimizing signal sampling enables us overcome this obstacle in the future, thereby further enhancing the protocol capacity and by implication its attractiveness for multiple applications.

4.5 Acknowledgement

This work was supported by National Key Research and Development Program of China (2022YFA1404800, 2019YFA0705000); National Natural Science Foundation of China (12192254, 92250304); Natural Sciences & Engineering Research Council (NSERC) of Canada (RGPIN-2018-05497).

Chapter 5

Prime number factorization with light beams carrying orbital angular momentum

This chapter's work is published in the paper entitled "Prime number factorization with light beams carrying orbital angular momentum", APL Photonics 9(4), 046107 (2024). The authors are Xiaofei Li, Xin Liu, Quanying Wu, Jun Zeng, Yangjian Cai, Sergey A. Ponomarenko and Chunhao Liang. We propose a simple and ultrafast protocol for prime number factorization by employing OAM endowed beams that are modulated by a prime number sieve. This sieving method not only facilitates rapid processing of large prime numbers but also ensures the confidentiality and integrity of information during storage and transmission.

My contribution to this work includes performing numerical simulations and formal analysis.

5.1 Introduction

The OAM beams have attracted enormous interest within the optical community since the pioneering work of Allen [185, 186]. Ever since their inception, the OAM beams have found diverse applications which take advantage of their phase singularities and mode orthogonality, among other unique properties. He et al. first observed the transfer of the optical OAM to a micro-particle, causing particle trapping by an optical vortex around a phase singularity [187]. Larocque et al. proposed the concept of optical framed topology, whereby the structures formed by the evolution of the phase singularity in space are employed as the information carriers to implement potent, high-security information encoding [188, 189] . Further, optical vortices can be utilized for mode division multiplexing to realize ultra-high capacity optical communication protocols [190, 191]. Fang et al. advanced an OAM holography as a promising technique for high-security, high-capacity optical encryption [45, 192, 193].

On the other hand, the prime number decomposition of an integer, which is a

cornerstone of number theory, has piqued the curiosity of the physics community due to recently discovered intriguing connections between the number theory and condensed matter physics [194] and photonics [195], respectively. Factorizing a large integer into primes is a tricky problem, though. On the flip side, the complexity of the task can ensure high security of number-decomposition based information encoding, all-optical machine learning and other number factorization related applications [192, 196, 197, 198]. To date, several approaches have been proposed to realize efficient prime number decomposition [199, 47, 48, 200, 49, 50, 51, 52, 53, 201], including quantum algorithms, quantum annealing, variational algorithms, and classical protocols involving Gauss sums. The latter involve coherent superpositions of optical waves [200, 49], Bose-Einstein condensates[50], nuclear spins [51], cold atoms [52], or matter waves in atom interferometers [53]. The interferometric approaches typically employ multiple sources to realize a Gauss sum whereby a single source produces a term in the sum. Therefore, such techniques place strenuous demands for precise phase control of multiple wave sources, which is often difficult to implement in experiment, especially if factorizing a large number is required [53]. At the same time, the factorization procedure relying on the optical Talbot effect is hampered by light diffraction from the apertures of an optical system, which, ultimately, sets the upper limit on the factorizable number. Indeed, Pelka et al. were able to factor only a modest number of 27 using this approach [200]. Recently, we have advanced a number factorization protocol employing axial correlation revivals of structured random waves, such that no phase control was necessary at all [49]. The approach of [49] makes it possible to decompose a number as large as a few million, but it is rather time-consuming to work with large statistical ensembles to accurately determine the speckle statistics. In this work, we propose and implement a conceptually simple, time-efficient classical optical approach to number factorization which involves OAM carrying optical beams and a carefully engineered prime number sieve. Our approach relies on the intrinsic periodicity of the phase distribution of an optical OAM beam propagating in free space.

5.2 Theory and simulation analysis

Consider the simplest OAM carrying optical beam, a Laguerre-Gaussian (LG) beam of zero radial mode index. The complex field amplitude of the beam can be expressed in cylindrical coordinates as [202]

$$E_l(r,\varphi) = A_0 \left(\frac{\sqrt{2}r}{w_0}\right)^{|l|} \exp\left(-\frac{r^2}{w_0^2}\right) \exp\left(-\mathrm{i}l\varphi\right), \tag{5.1}$$

where l is a topological charge of the beam vortex and w_0 is a beam width at its waist. The phase of the beam field spirals around the beam propagation direction z as is schematically shown in Fig. 5.1(a). In any transverse plane $z = const$, the phase is manifesltly periodic with the period $\varphi_T = 2\pi/l$.

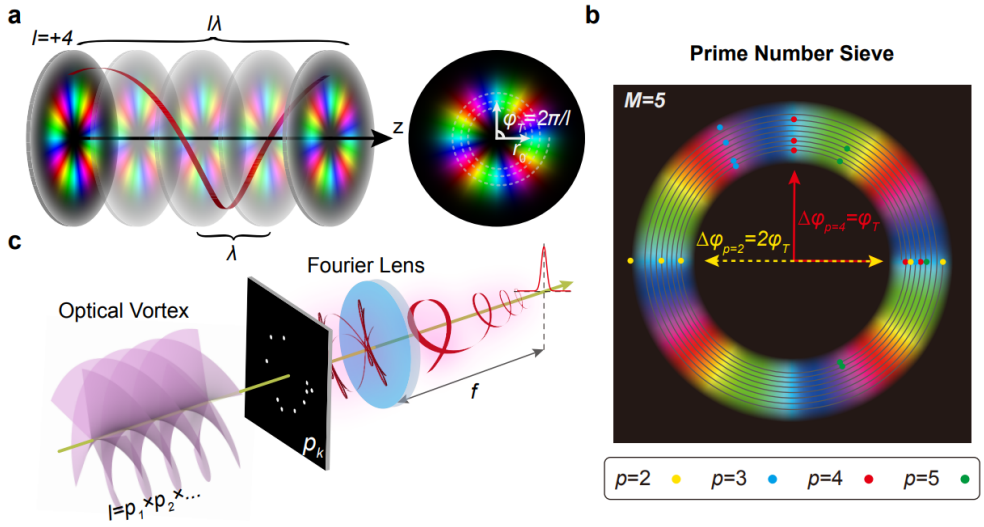

Figure 5.1: Schematic illustration of the principle of prime number factorization with OAM beams. (a) The phase distribution of an OAM beam twisted as a spiral staircase during propagation exhibits azimuthal periodicity with the period $\varphi_T = 2\pi/l$. (b) Prime number sieve examples marked with color dots. (c) Implementing prime number factorization with OAM beams. Hue and brightness of plots in (a) and (b) refer to the phase and intensity, respectively.

To perform prime number decomposition with such LG beams, we engineer a prime number sieve composed of M Dirac pinholes lying on a curve spiralling around the optical axis as shown in Fig. 5.1(b). The transmittance function T_p of the sieve

is defined as

$$T_p\left(r,\varphi\right)=\frac{1}{M}\sum_{m=1}^{M}\delta\left(\varphi-\frac{2\pi m^2}{p}+\varphi_0\right)\delta\left(r-r_m\right), \tag{5.2}$$

where M is the number of pinholes, δ is Dirac delta function, and φ_0 denotes the initial phase. In the experiment, each Dirac pinhole is replaced by a circle of diameter d. Further, $r_m = r_0 + m^2/p \cdot d$ is an offset of the mth pinhole from the optical axis; p is a trail factor, and m^2/p determines in between which consecutive rings the m^{th} pinhole is located. The second delta function on the right-hands side of Eq. (5.2) ensures that the pinholes falling into the areas between different consecutive rings do not overlap.

We envision an optical system such that the OAM beam, modulated by the prime number sieve, is focused by a thin lens [see Fig. 5.1(c)]onto an observation screen. We can express the beam field in the rear focal plane of the lens as

$$U_f(\mathbf{r})=-\frac{i}{\lambda f}\int d^2\mathbf{r}' E_l(\mathbf{r}',\varphi)T_p(\mathbf{r}',\varphi)e^{-ik\mathbf{r}'\cdot\mathbf{r}/f}, \tag{5.3}$$

where $\mathbf{r}=(r,\theta)$ and $\mathbf{r}'=(r',\varphi)$. On substituting from Eqs. (5.1) and (5.2) into Eq. (5.3), we obtain

$$\begin{aligned} U_f(\mathbf{r}) \propto & \frac{1}{M}\sum_{m=1}^{M} r_m\left(\frac{\sqrt{2}r_m}{w_0}\right)^{|l|} e^{-r_m^2/w_0^2}e^{-2\pi i\Delta\varphi_p/\varphi_T} \\ & \times\exp\left[-\frac{\mathrm{i}krr_m}{f}\cos\left(\theta-\frac{2\pi m^2}{p}+\varphi_0\right)\right], \end{aligned} \tag{5.4}$$

up to an immaterial constant. In the approximation $r_0 \gg m^2/p$, the on-axis intensity reduces to

$$I_{\text{axis}}\propto\left|\frac{1}{M}\sum_{m=1}^{M}\exp\left(-2\pi i\frac{\Delta\varphi_p}{\varphi_T}\right)\right|^2=\left|\mathcal{G}_M\left(p,l\right)\right|^2, \tag{5.5}$$

where $\Delta\varphi_p = 2\pi m^2/p$. The function $\mathcal{G}_M(p,l)$ is an incomplete Gauss sum, defined as [201]

$$\mathcal{G}_M(p,l)=\frac{1}{M}\sum_{m=1}^{M}\exp(-2\pi i m^2 l/p). \tag{5.6}$$

In our protocol, the number to be factored and trial factors are given by the topological charge l of an OAM beam and number p which specifies locations of the pinholes in the sieve. The Gauss sum equals to unity whenever $\Delta\varphi_p$ are multiples of φ_T, such that p is a trial factor of the topological charge. Otherwise, $\mathcal{G}_M(p,l)$ oscillates rapidly, taking on small values. In Fig. 5.1(b), we exhibit four prime number sieves with

$p = 2, 3, 4$, and 5, marked by the dots of different colors. We assume there are 5 pinholes, $M = 5$ and the number to be factorized is $l = 4$. Whenever p is a factor of l, i.e., $p = 2$ (yellow dots) and 4 (red dots), all pinholes are in phase. We can infer from Eq. (5.5) that the result is independent of the initial phase φ_0, implying that our protocol is insensitive to initial placement angle of the sieve. This is a huge bonus for the experimental implementation of our protocol. We note that we adopt a general criterion $M \geqslant 0.7\sqrt[4]{l}$ to suppress all non-factors situated below a threshold value $1/\sqrt{2}$ to improve factor identification[201].

We now present our numerical simulations of the proposed number factorization protocol sketched in Fig. 5.1(c). The incident OAM beam with the topological charge l and wavelength λ passes through the prime number sieve, and is then focused by a thin lens of focal length f. We can evaluate the on-axis intensity numerically using the Matlab. We chose the following numerical parameters: λ=532nm, f=400mm, d=0.04mm, r_0=6mm and M=7. In Fig. 5.2 we display three examples of prime number factorization with OAM beams of variable l. We express the number l to be factorized as a product of prime factors, exhibited on top of each panel in Fig. 5.2. All results demonstrate that as long as p is a factor of l, the (normalized) on-axis intensity equal to unity to good accuracy; otherwise, it takes on small values below the threshold value $1/\sqrt{2}$ labelled by the dash-dotted line. Our theoretical results [blue squares, attained by the incomplete Gauss sum] and simulation results (red dots) are in good agreement, validating the feasibility of our protocol.

5.3 Experimental implementation

We proceed to the experimental implementation of the protocol. A linearly polarized beam of the carrier wavelength 532nm, emitted from a DPSS laser, passes through a half-wave plate (HP) and a beam expander (BE). We rotate HP to guarantee the horizontal polarization of an output beam as it must align with the reflection angle of a phase-only spatial light modulator (SLM) (Holoeye GAEA-2, 3840×2160 Pixels with a 3.74μm$\times 3.74\mu$m pixel pitch). To generate a high-quality OAM beam [described by Eq. (5.1)], we employ the complex-amplitude encoding scheme [202] to customize a computer-generated hologram to be loaded onto the SLM [see an example for $l = 30$ in Fig. 5.3(a)]. The input beam illuminates the SLM, and $+1^{\text{st}}$ or -1^{st}-order diffracted

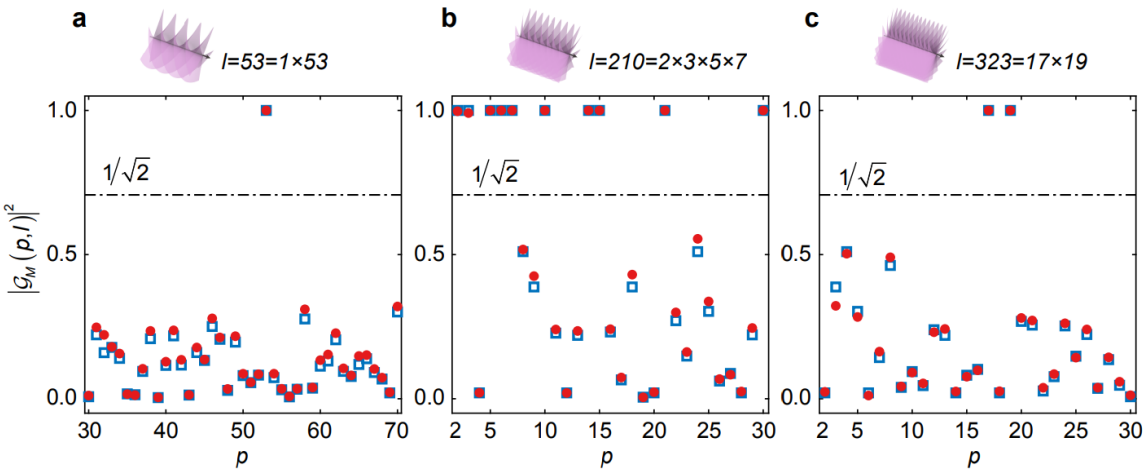

Figure 5.2: Numerical simulation of prime number factorization with the OAM beam with l=1×53 (a), l=2×3×5×7 (b) and l=17×19 (c). The blue squares (red dots) mark theoretical results obtained from the incomplete Gauss sum (simulation results obtained with the aid of Matlab).

beam forms our output OAM beam. Such a beam can be selected out via a modified $4f$ optical system consisting of two lenses of focal length $f_1 = f_2 = 10$cm and an iris. We employ a generalized Arago spot method [203] to obtain the complex field distribution of the generated OAM beam, which we illustrate in Fig. 5.3(b). Hue and brightness refer to the phase and intensity of the beam, respectively. The generated OAM beam illuminates a Digital Micro-mirror Device (DMD) (Vialux, 1920×1080 pixels with a 10μm×10μm pixel pitch), to which the prime number sieve is loaded. The sieve is displayed in Fig. 5.3(c), and the relevant parameters are set as M =7, $d = 0.15$mm and $r_0 = 3$mm. The modulated beam is focused by a thin lens (Lens 3) of focal length of $f_3 = 40$cm and a camera, located in the rear focal plane of the lens, records an intensity pattern.

We exhibit three normalized intensity patterns in Fig. 5.4. We take the topological charge to be $l = 30$. Following Eq. (5.2), we design three prime number sieves varying the magnitude of p. We set the other parameters as M=7, d=0.15mm and r_0= 3mm. We find that the on-axis normalized intensity (marked by the cross symbol) is unity if p is a factor of $l = 30$ (see $p = 5$ and 10 in the central and right panels), or not (see $p = 4$ in the left panel). Further, we experimentally factor the numbers l=30 and l=53. We present our results in Fig. 5.5. It can be seen in the figure that the factors

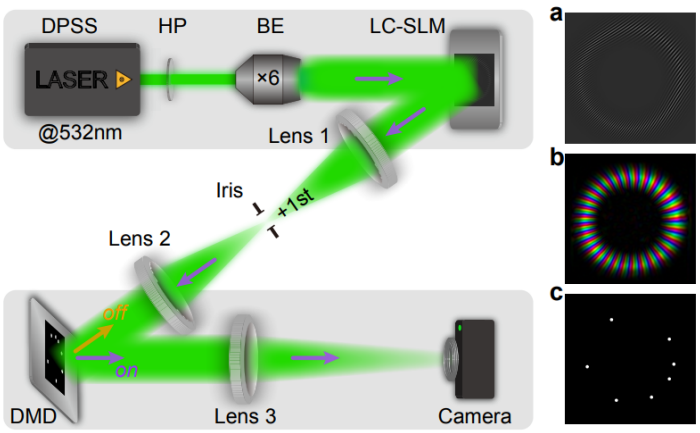

Figure 5.3: Experimental setup for prime number factorization with OAM beams. DPSS, Diode-Pumped Solid-State laser; HP, half-wave plate; BE, beam expander; SLM, reflective phase-only liquid crystal spatial light modulator; DMD, Digital Micromirror Device. (a) Computer-generated hologram of a Laguerre-Gauss beam with topological charge l=30 and $w_0 = 0.8$ mm. (b) Complex amplitude of an experimentally reproduced Laguerre-Gaussian beam at the front surface of the DMD. The image size is 9.6 mm ×9.6 mm, and hue and brightness refer to the phase and intensity, respectively. (c) An example mask of prime number sieve T_p with M=7, $d = 0.15$ mm and $r_0 = 3$ mm.

and non-factors of both numbers are clearly discriminated by the threshold value of $1/\sqrt{2}$. Slight deviations of the experimental from simulation results are mainly due to misalignment between the OAM beam and prime number sieve axes, as well as to imperfect generation of the OAM beam. Overall, our experimental results agree well with our simulations, as is seen in Figs. 5.4 and 5.5.

In our time-efficient number factorization protocol, l serves as a number to be factored, so that we first produce the required OAM beam. It is followed by design of a set of variable trial number sieves. It is worth noting that the transmittance function of any sieve is binary, such that light passes through the pinholes and reflected otherwise. Such a sieve is realized by the DMD, and in the binary regime, the refreshment rate of the DMD can reach the maximum value of around 17 kHz. It implies that we can rapidly change the sieve in order to swiftly refresh the trial factor p. In the receiver plane, we can use the camera with a high frame rate to quickly record the intensity patterns of the modulated OAM beams saved as 8-bit grayscale

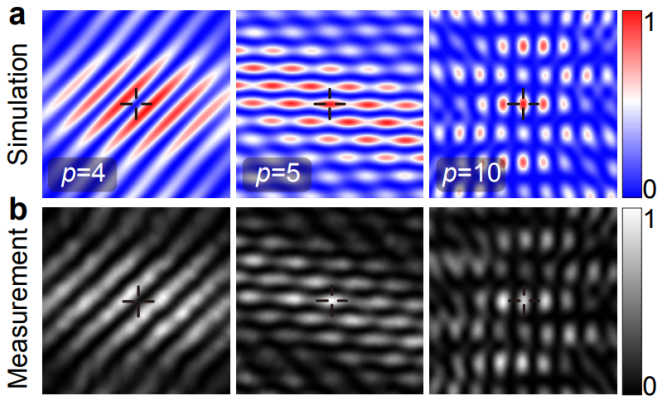

Figure 5.4: Numerical (a) and experimental (b) results for the normalized intensity patterns of an OAM beam modulated by prime number sieves. The topological charge is $l = 30$ and the trial factor p is given by 4, 5, 10 from left to right. The size of each pattern is 375μm$\times 375\mu$m, and the optical axis is labelled by the cross symbol.

pictures. The commercial software Matlab reads a picture and converts it into a matrix. We save a gray value of the central pixel (corresponding to the on-axis intensity value) and plot it as a function of the trial number p. This function is normalized by its maximum to ensure the on-axis intensity value is unity when p is a factor of l. We can visually separate factors from non-factors by looking at the threshold line. According to a short board principle, the speed of our technology mainly depends on the lower of the refreshment rate of the DMD and the camera frame rate. Here we choose the camera (IBTEK, STC-MBS43POE) as an example. Its frame rate can be up to 282 fps, so that the ideal time interval to test a trial factor is around 3.55 ms. If we attempt to factorize a large number $l = 10^6$, say, the trial factor p takes one values from 2 to $\sqrt{l}$. The total time it takes to perform the factorization is then around 3.55 s, which is significantly faster than the competing number factorization methods.

Further, the noisy nature of any realistic light source implies that any genuine light beam is, in practice, only partially coherent. The latter has a random (fluctuating) phase. Our protocol heavily relies on the tight control of source OAM beam and sieve pinhole phases, and hence can lose its credibility in presence of phase fluctuations. To elucidate the role of phase fluctuations, we compare the fluctuating and ensemble average phases in Fig. 5.6(a). The latter is obtained by averaging over an ensemble of 5000 realizations of OAM beams with topological charge $l = 2$. We observe in the

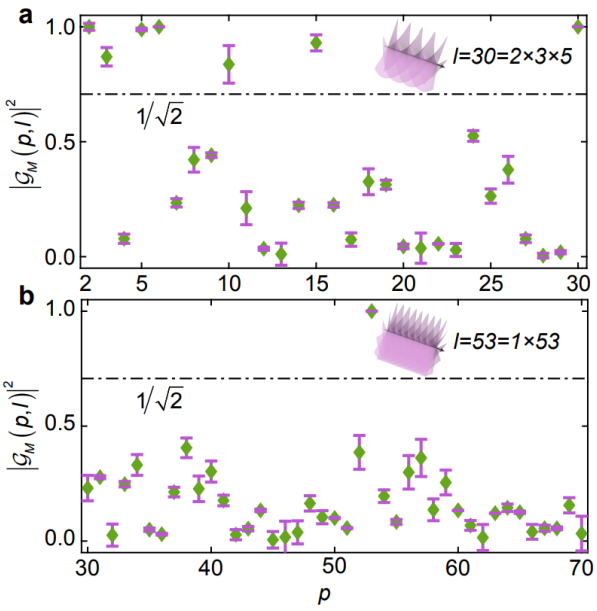

Figure 5.5: Experimental implementation of prime number factorization with OAM beams. The number to be factorized is given by $l = 30$ (a) and $l = 53$(b). The vertical lengths of error bars characterize an absolute value of the difference between the experimental and simulation results.

figure that the average phase is rather stable within the purple dashed circle area. In Fig. 5.6(b), we plot the phase magnitudes at the same locations, labelled by the purple dots p_1 and p_2, within the phase distributions of the random and average phases. We can infer from the figure that the random phase (blue line) fluctuates dramatically with time while the average phase (red line) is nearly stationary. Instructively, the average phase outside the purple dashed circle area fluctuates as well [see the right panel in Fig. 5.6(a)]. The radius of the circle is given by the coherence width of the source. Thus, we can employ noisy OAM beams in our number factorization protocol as long as the pinholes of the sieve are offset from the optical axis by distances shorter than the coherence width of the beam.

5.4 Conclusion

In summary, we have pointed out the link between number theory and the OAM beams that makes it possible to formulate a simple and time-efficient protocol for number factorization. In our protocol, an OAM beam, modulated by a prime-number

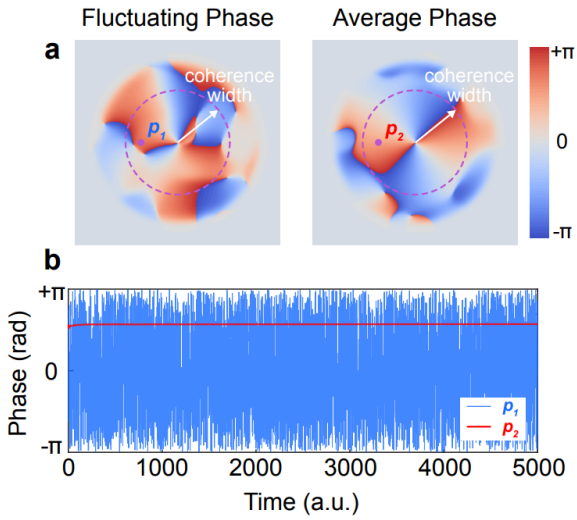

Figure 5.6: (a) Fluctuating and ensemble average phases of the field of a noisy OAM beam. (b) Time evolution of two phases at the same locations within the phase distribution marked by the purple dots (p_1 and p_2) in (a). The radius of the purple dashed circles in (a) corresponds to the coherence width of the beam.

sieve, is focused by a thin lens. The number to be factorized corresponds to the topological charge of the beam, and all trial p are encapsulated into the sieve. The factors and non-factors can be distinguished by measuring the on-axis intensity of the focused beam. The experimental scheme is simple and the results are independent of the sieve orientation. We can swiftly refresh a sieve by a DMD to change the trial factor p. In principle, we can decompose a number as large as even 10^6 in 3.55s by our protocol. Our protocol works for noisy OAM beams as long as the sieve size is smaller than the coherence width of the beam. Our results are independent of the wavelength of light and only depend on the azimuthal periodicity the phase distribution of OAM beams. Hence, our protocol is capable of handling any OAM beams, such as Laguerre-Gaussian, Bessel, etc., as well as vortex carrying waves of any physical nature (electron, matter-wave vortices, etc).

5.5 Acknowledgement

This work was supported by the National Key Research and Development Program of China (Grants No. 2022YFA1404800 and No. 2019YFA0705000), the National Natural Science Foundation of China (Grants No. 12374311, No. 11974218,

and No. 92250304), the Qingchuang Science and Technology Plan of Shandong Province (Grant No.2022KJ246), the China Postdoctoral Science Foundation (Grant No. 2022T150392), the Natural Science Foundation of Shandong Province (ZR2023YQ006), and the Natural Sciences and Engineering Research Council of Canada (Grant No. RGPIN-2018-05497).

Chapter 6

Conclusion

This chapter provides an overview of the thesis, draws conclusions, and outlines plans for future research.

6.1 Discussion and Conclusion Remarks

In Chapter 2, we propose theoretically and implement experimentally an FSO protocol for high-fidelity image transfer through a complex environment. The protocol is a combination of structuring random light at the transmitter with the engagement of a deep learning network at the receiver end. This fusion offers several advantages. First, the utilization of random light source grants access to a multitude of novel, independent, mutually orthogonal degrees of freedom (DoF) associated with two-point correlations of structured light fields at the source. This creates numerous avenues for multiplexing among such crosstalk-free DoFs to boost communication capacity of our FSO link, some of which we explicitly demonstrate. Second, light beams generated by structured random sources have been previously demonstrated to be extremely resilient to environmental noise, such as atmospheric turbulence, and capable of self-reconstructing upon encountering opaque obstacles, such as colloidal particles, to a far greater extent than their coherent cousins. This feature improves the received image quality, thereby enhancing the fidelity of information transmission in our protocol. Finally, the documented capacity of deep learning networks to realize accurate object classification in a timely manner further ensures the efficiency and fidelity of our FSO protocol, making it an attractive candidate to transfer images, or other forms of information messages, through complex environments. This work provides a fresh impetus to the emerging field of free-space optical communications with structured random light and it will undoubtedly inform further research in the topical field of deep learning network applications to photonics.

The structured random light-based FSO communication link of Chapter 2 is limited to short-distance information transfer. Thus, for outdoor wireless long-distance information transport, it is essential to design an innovative structured random light model by modulating the correlation structure. In Chapter 3, we introduce perfect correlation vortices and show that the degree of coherence of any such vortex at the source is nearly statistically homogeneous and independent of the topological charge of the vortex. We demonstrate that while slowly diffracting in free space, perfect correlation vortices maintain their "perfect" vortex structure; they are capable of preserving said structure even in strong atmospheric turbulence. Structural resilience to diffraction and turbulence sets the discovered perfect correlation vortices apart from their coherent cousins and makes them potential candidates for long-distance free space optical communications.

In Chapter 4, we theoretically propose and numerically simulate an efficient multifunction radar system that leverages optical vortex structures to achieve imaging, real-time positioning, and tracking 2D targets. The principle of this protocol involves modulating detection signals using optical vortices, and real-time processing within its imaging field makes it possible to track and estimate the velocity of a moving target. Furthermore, the protocol's extension to 3D landscape identification as a topographic laser profiling system underscores its adaptability to diverse scenarios. This versatility and adaptability of our radar protocol indicate the potential of this proposed radar across a wide range of applications, from self-driving vehicles to aerial systems.

In Chapter 5, we propose a conceptually simple and fast protocol for prime number factorization using OAM-endowed beams, modulated by a prime number sieve. Our protocol establishes a surprising link between optics of structured light and number theory. By measuring the on-axis intensity of light in the rear focal plane of a thin lens focusing a source beam, we can effectively differentiate prime factors from non-factors of a given number. The proposed protocol leverages the periodicity of the OAM phase distribution, making it applicable to fully or partially coherent fields of any frequency and physical nature ranging from optical and x-ray to matter waves endowed with OAM. This protocol will inspire new advancements in optical cryptography and information storage using OAM beams.

6.2 Future work

Motivated by these advancements, we will continue exploring the integration of structured random light with information networks.

Regarding the structured random light-based FSO communications, several intriguing topics are awaiting further exploration.

First, Chapter 2 states that any value of coherence radius can be used as an individual state, thereby providing, in principle, an infinite number of states to boost information capacity. In practice, however, if the coherence radii of adjacent states are too close to each other, the states can be difficult to distinguish, leading to a high crosstalk among adjacent channels. It poses a greater challenge to high-quality data transfer. One effective solution is to enhance the classification accuracy by optimizing the signal processing network to leverage machine learning.

Second, as stated in the first three chapters, coherence radii and correlation functions of structured random light are two DoFs that can be multiplexed together. However, we would like to point out that the integration of several DoFs may give rise to some issues such as precision and interference. Hence, the combined effect of two or more DoFs should be discussed in the forthcoming work.

Third, the perfect correlation vortex beams introduced in Chapter 3 are promising candidates for high-capacity long-haul transmission in noisy free-space environment. However, the current experimental generation of these beams relies on the superposition of many holographic modes, leading to a relatively long computation time. This method does not meet the critical requirement for time efficiency in communication. Therefore, it is essential to consider effective time-saving methods in experimental setups.

As for the radar protocol, the MFR scheme introduced in Chapter 4 has versatile functions and is adaptable to various working scenarios. However, the drawback of this scheme is its low precision. On the one hand, the azimuthal and radial positioning can only be roughly determined, lacking precision. As a result, for high-speed moving objects, the positioning and tracking capabilities are somewhat inadequate. On the other hand, when the protocol is employed in practical application, the limited imaging resolution of devices will exacerbate the precision deficiency.

Our work in Chapter 5, exploring the number theory of OAM beams, plays a

crucial role in protecting the integrity and security of information. Therefore, another objective is to establish a joint information network involving information acquisition, transfer, and storage. This network will effectively synergize with OAM-carrying structured random light to enhance data transmission efficiency and security.

Appendix

Appendix A Deep learning and random light structuring ensure robust free-space communications

The structure of ResNet 34— ResNet 34 is a specific implementation of a deep

Table 6.1: **ResNet 34 architecture**

Layer Name	Output Size	34-Layer
Conv1	112×112	7×7, 64, stride 2
		3×3 max pool, stride 2
Conv2	56×56	$\begin{bmatrix} 3 \times 3, & 64 \\ 3 \times 3, & 64 \end{bmatrix} \times 3$
Conv3	28×28	$\begin{bmatrix} 3 \times 3, & 128 \\ 3 \times 3, & 128 \end{bmatrix} \times 4$
Conv4	14×14	$\begin{bmatrix} 3 \times 3, & 256 \\ 3 \times 3, & 256 \end{bmatrix} \times 6$
Conv5	7×7	$\begin{bmatrix} 3 \times 3, & 512 \\ 3 \times 3, & 512 \end{bmatrix} \times 3$
	1×1	average pool, fc, softmax

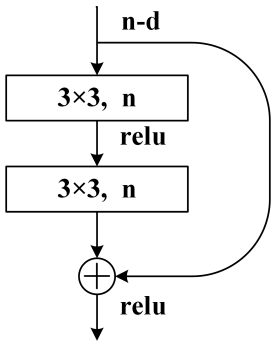

Figure 6.1: Residual building block diagram of ResNet 34 with n representing a number of convolution kernels.

residual network; we list the ResNet34 parameters in Tab. 6.1. ResNet 34 comprises 33 convolutional layers and one average pool layer, followed by a fully connected layer. The overall architecture of ResNet 34 can be subdivided into five modules from Conv1 to Conv5. Conv1 is a 7×7 convolutional layer with a stride of 2, followed by a 3×3

max pooling layer with a stride of 2. The next four modules, Conv2 to Conv5, mainly consist of a series of residual building blocks which form the basis of ResNet 34 network. The residual building block is composed of the following convolutional layers: batch normalization, rectified linear unit activation function (ReLU) and a shortcut, as shown in Fig. 6.1. The residual block is designed to effectively alleviate the problem of vanishing and exploding gradients caused by the depth increase of the neural network. It can improve the classification efficiency, namely, the decoding fidelity of our FSO system. The number of residual building blocks embedded into Conv2, Conv3, Conv4 and Conv5 is 3, 4, 6 and 3, respectively. The convolution kernel size is fixed at 3×3. The corresponding numbers of convolution kernels are then 64, 128, 256 and 512. Additionally, after each stage, downsampling is performed to reduce the size of feature maps and achieved by a 1×1 convolutional layer with a stride of 2. The final module of ResNet 34 is a global average pooling layer which transforms the feature map into a vector. A fully connected layer with a softmax activation function is then used to obtain the final classification results.

Experimental setup for image transfer through random medium— The setup for image transmission through a realistic random medium is similar to that in Fig. 2.3; only the optical elements emulating the complex environment are added. In the image transmission through turbulence experiment—see Fig. 6.2(a)—we apply an optical diffuser (OD) with a diffuse Gaussian-like distribution to emulate atmospheric turbulence (https://www.lbtek.com/product/92/product_id/1489.html#DW120-1500). A OD is employed to simulate weaker turbulence, while two ODs are placed in the beam path to mimic stronger turbulence. We place a sector-shaped opaque obstacle (SSOO) with an angle of $2/3\pi$ in the light path to model obstructing particles in a separate experiment shown in Fig 6.2(b).

Resilience of LG-correlated beams to obstacles— We can see in Fig. 6.3 that the structure of fully coherent LG beams at the receiver is heavily affected by the presence of solid particles in the medium, while the corresponding patterns of LG-correlated beams are hardly affected by the obstructions at all due to their outstanding self-healing capabilities. Our results are consistent with the previous work on the subject[96, 204].

LG-correlated beam intensity versus source coherence radius— In our protocol

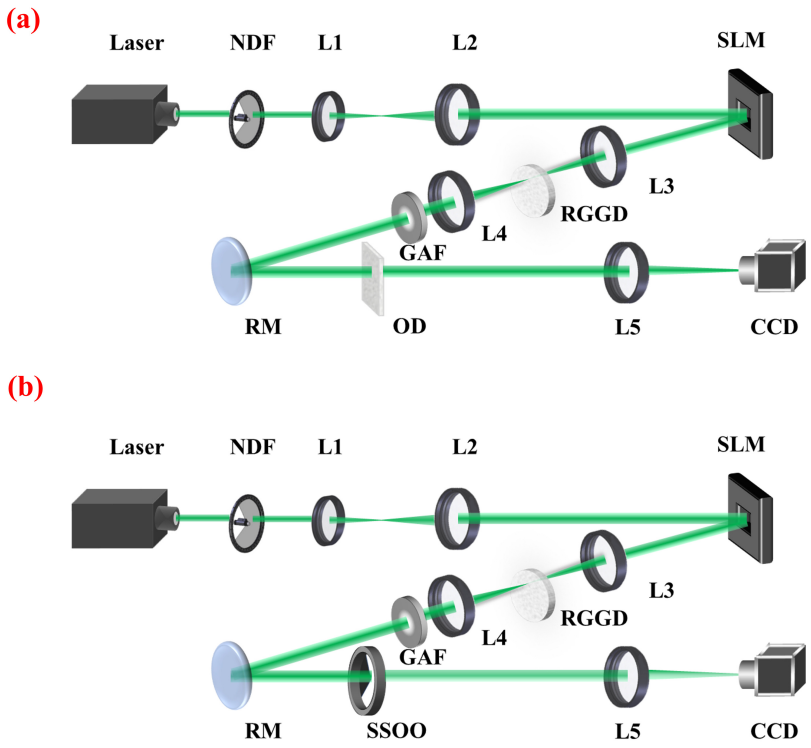

Figure 6.2: Experimental setup of grey image (a) transmitting in atmospheric turbulence and (b) suffering obstructing particles. OD: optical diffuser; SSOO: sector-shaped opaque obstacle, others are same with Fig. 2.3.

utilizing the source coherence radius for image encoding, the 4 quaternary states for image encoding correspond to $\sigma_c = 0.02$mm, 0.025mm, 0.03mm, 0.05mm. These states are realized with the aid of digital focusing holograms of four focal lengths: $f = 50, 500, 700$, and 1200mm.

Transmitted image fidelity evaluation— We assess the performance of our protocol by evaluating the conditional probability $P_{s_r|s_t}$ of a measuring state s_t given s_r and the total fidelity of each transmission. Here, we give a simple example to illustrate the evaluation process. We stress that this is just an illustrative example which has nothing to do with the actual transmitted data.

Suppose a transmitted data string is composed of 12 quaternary numbers, "000111222333", say. Further, assume that the received string is "000101223333". First, we notice that each transmitted quaternary state is composed of 3 digits, such that each transmitted state s_t makes the fraction $P_0 = P_1 = P_2 = P_3 = 3/12 = 0.25$ of the total

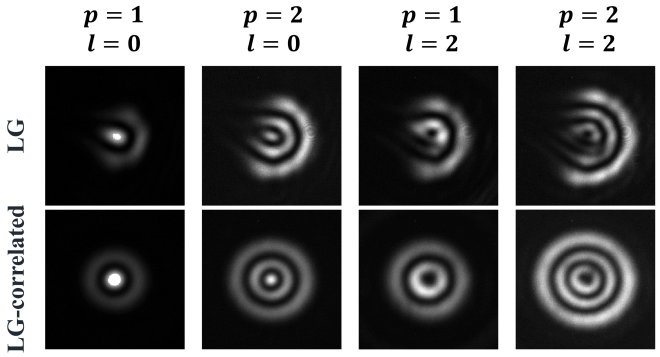

Figure 6.3: Recorded intensity profiles of LG-correlated versus fully coherent LG beams obstructed by a sector-shape obstacle situated in the beam path.

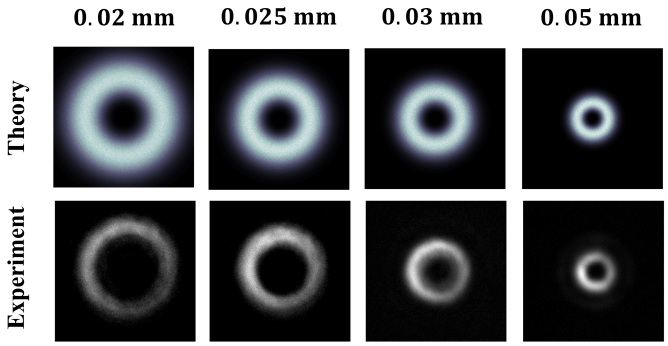

Figure 6.4: Normalized intensity of an LG-correlated beam (LG_{04}) at the receiver generated by a source of variable coherence radius.

12 digits making up the information string. Further, on comparing the transmitted and received data strings, we can infer that 2 states are incorrectly received (marked in red ink): the 5th digit in the received string is 0 instead of 1, while 9th is 3 in lieu of 2. We can then compose a confusion matrix N based on these observations. The row and column elements of the confusion matrix are separately determined by the transmitted and received states. Starting with the first row, all 3 transmitted "0" are correctly received as "0", implying that $N_{00} = 3$, and $N_{01} = N_{02} = N_{03} = 0$. Next, consider the second row. We notice that 3 transmitted states "1" are received as 2 states "1" (correct) and 1 state "0" (incorrect). Thus, $N_{10} = 1$, $N_{11} = 2$, and $N_{12} = N_{13} = 0$. Following the same procedure, we can fill up the other two rows of the "green" matrix . We have $N_{22} = 2$, $N_{23} = 1$ and $N_{33} = 3$, with the other matrix elements being zeroes. We exhibit the resulting

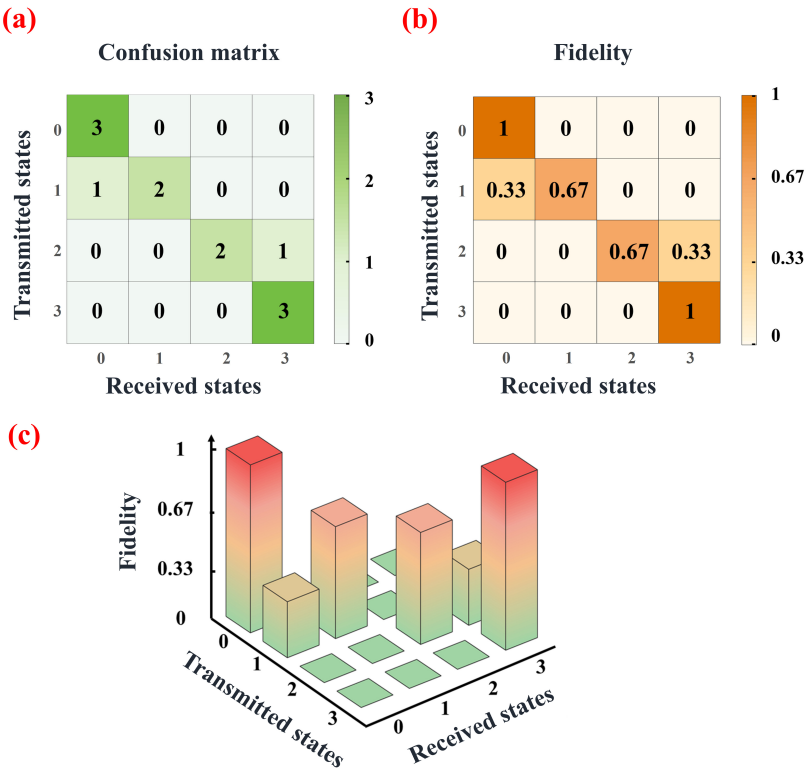

Figure 6.5: Confusion matrix and transmission fidelity of an illustrative example.

matrix in Fig. 6.5(a). We can then easily evaluate the conditional probabilities of of finding transmitted states in given received states as follows: $P_{0|0} = P_{3|3} = 3/3 = 1$, $P_{1|1} = P_{2|2} = 2/3 = 0.67$, $P_{0|1} = P_{3|2} = 1/3 = 0.33$, with the others being 0. We display these results in the "brown" matrix of Fig. 6.5(b), as well as show them with the bar chart in Fig. 6.5 (c). Finally, we can evaluate the total fidelity of data transmission as $\sum_{s_r=s_t} P(s_r|s_t)\,P(s_t) = 1\times 0.25 + \frac{2}{3}\times 0.25 + \frac{2}{3}\times 0.25 + 1\times 0.25 = 83.3\%$.

At the same time, the total fidelity of image transmission is determined by the fraction of correctly received states versus the total number of transmitted states as $10/12 = 83.3\%$, which is in complete agreement with our calculation based on state detection probabilities.

Qualitative comparison of transmitted and received images— We juxtapose the transmitted and received images of Lena and show the quantitative measure of the state detection fidelity on the side in Fig. 6.6. Specifically, we can infer from Fig. 6.6(a) and Fig. 6.6(b) that neither medium turbulence nor the presence of opaque particles significantly degrades the image in our protocol when the source coherence structure

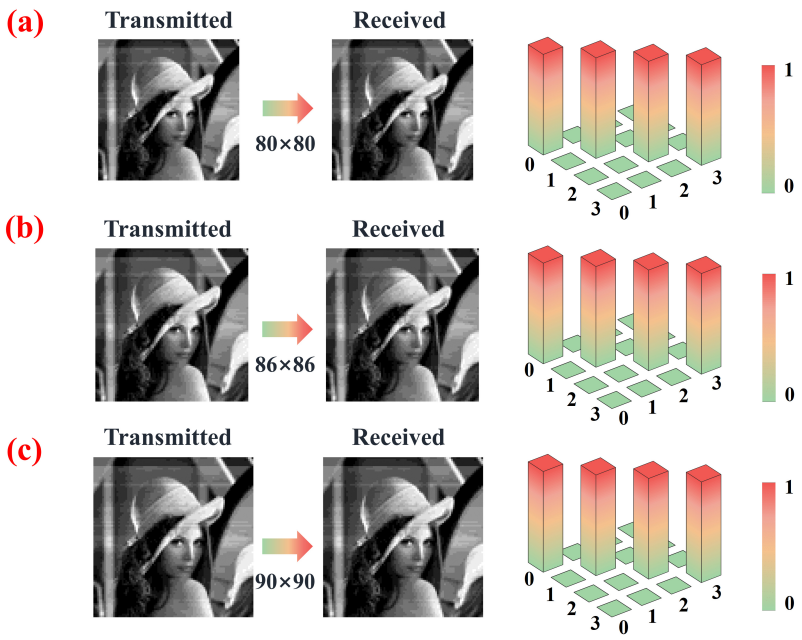

Figure 6.6: Qualitative (visual) and quantitative (fidelity) comparison between transmitted and received images. (a), & (b) correspond to the protocol utilizing the source correlation structure, while (c) corresponds to that using the source coherence length for image encoding. The color bar shows normalized fidelity with unity corresponding to 100%.

is employed for image encoding. The same conclusion applies to our protocol with the source coherence radius which is evidenced by Fig. 6.6(c).

Appendix B Derivation of PCV evolution in free space

First, let us substitute Eq. (3.3) into Eq. (3.11), we can obtain the evolution of each pseudo-mode in free space.

$$\begin{aligned}
\Psi_m^{(k)}(r,\phi,z) &= \frac{k_0}{2\pi i z}\int d\mathbf{r}'\Psi_m^{(k)}(r',\phi',0)\exp\left(\frac{ik_0(\mathbf{r}-\mathbf{r}')^2}{2z}\right)\\
&= \frac{k_0}{2\pi i z}\int_0^\infty r'dr'\sqrt{k}J_m(kr')\exp\left(\frac{ik_0r'^2}{2z}\right)\exp\left(-\frac{r'^2}{2w_0^2}\right)\\
&\quad \exp\left(\frac{ik_0r^2}{2z}\right)\int_0^{2\pi}\exp(im\phi')\exp\left[\frac{-rr'ik_0}{z}\cos(\phi-\phi')\right]d\phi'\\
&= \frac{\sqrt{k}k_0}{iz}\exp\left(\frac{ik_0r^2}{2z}\right)\exp(im\phi)\\
&\quad \int_0^\infty J_m(kr')J_m\left(\frac{rr'k_0}{z}\right)\exp\left(-\frac{r'^2}{2w_0^2}\left(1-\frac{iL_R}{z}\right)\right)r'dr'\\
&= \frac{\sqrt{k}}{(1+iz/L_R)}\exp(im\phi)\exp\left(\frac{ik_0r^2}{2z}\right)\\
&\quad \exp\left[-\frac{w_0^2(k^2+r^2k_0^2/z^2)}{2(1-iL_R/z)}\right]J_m\left[\frac{kr}{(1+iz/L_R)}\right].
\end{aligned} \tag{6.1}$$

It follows with the aid of the integral representation for the Bessel function and the table integral [205]

$$I_m(x) = i^{-m}J_m(ix), \tag{6.2}$$

$$J_m(x) = \frac{1}{2\pi i^m}\int_0^{2\pi} e^{ix\cos\phi}e^{-im\phi}d\phi, \tag{6.3}$$

$$\int_0^\infty dx x J_m(ax)J_m(bx)e^{-cx^2} = \frac{1}{2c}\exp\left(-\frac{a^2+b^2}{4c}\right)I_m\left(\frac{ab}{2c}\right). \tag{6.4}$$

Thus, we can obtain the vortex modes at points $\boldsymbol{r}_j$ $(j=1,2)$ in any transverse plane z,

$$\begin{aligned}
\Psi_m^{(k)}(r_j,\phi_j,z) =& \frac{\sqrt{k}}{(1+iz/L_R)}\exp\left(\frac{ik_0r_j^2}{2z}\right)\exp(im\phi_j)\\
&\exp\left[-\frac{w_0^2\left(k^2+r_j^2k_0^2/z^2\right)}{2(1-iL_R/z)}\right]J_m\left[\frac{kr_j}{(1+iz/L_R)}\right].
\end{aligned} \tag{6.5}$$

Subsequently, Eq. (6.5) can be substituted into Eq. (3.10) yielding

$$
\begin{aligned}
W\left(\mathbf{r}_1,\mathbf{r}_2,z\right) &= \int_0^\infty dk \exp\left(-k^2\sigma_c^2\right)\Psi_m^{(k)*}\left(\mathbf{r}_1,z\right)\Psi_m^{(k)}\left(\mathbf{r}_2,z\right) \\
&= \int_0^\infty dk \exp\left(-k^2\sigma_c^2\right)\frac{k}{\left(1+iz/L_R\right)\left(1-iz/L_R\right)}\exp\left[\frac{-ik_0\left({r_1}^2-{r_2}^2\right)}{2z}\right] \\
&\quad\times\exp\left[im\left(\phi_2-\phi_1\right)\right]\exp\left[-\frac{w_0^2\left(k^2+{r_2}^2k_0^2/z^2\right)}{2\left(1-iL_R/z\right)}\right]J_m\left[\frac{kr_2}{\left(iz/L_R+1\right)}\right] \\
&\quad\times\exp\left[-\frac{w_0^2\left(k^2+{r_1}^2k_0^2/z^2\right)}{2\left(1+iL_R/z\right)}\right]J_m\left[\frac{kr_1}{\left(-iz/L_R+1\right)}\right] \\
&= \exp\left[\frac{-ik_0\left({r_1}^2-{r_2}^2\right)}{2z}\right]\exp\left[-\frac{\left({r_2}^2+{r_1}^2\right)}{2w_0^2\left(z^2/{L_R}^2+1\right)}\right] \\
&\quad\times\exp\left[-\frac{ik_0}{2z}\left[\frac{\left({r_2}^2-{r_1}^2\right)}{1+z^2/{L_R}^2}\right]\right]\frac{\exp\left[im\left(\phi_2-\phi_1\right)\right]}{\left(1+z^2/{L_R}^2\right)} \\
&\quad\times\int_0^\infty dkkJ_m\left[\frac{kr_1}{\left(-iz/L_R+1\right)}\right]J_m\left[\frac{kr_2}{\left(iz/L_R+1\right)}\right]\exp\left[-\left(\frac{w_0^2}{1+{L_R}^2/z^2}+\sigma_c^2\right)k^2\right] \\
&= \frac{\exp\left[im\left(\phi_2-\phi_1\right)\right]}{2\left(\frac{w_0^2}{1+{L_R}^2/z^2}+\sigma_c^2\right)\left(1+z^2/{L_R}^2\right)}\exp\left[-\frac{\left({r_2}^2+{r_1}^2\right)}{2w_0^2\left(z^2/{L_R}^2+1\right)}\right] \\
&\quad\exp\left[\frac{ik_0}{2z}\left(\frac{{r_2}^2-{r_1}^2}{1+{L_R}^2/z^2}\right)\right]I_m\left[\frac{r_1r_2}{2\left(\frac{w_0^2}{1+{L_R}^2/z^2}+\sigma_c^2\right)\left(z^2/{L_R}^2+1\right)}\right] \\
&\quad\exp\left\{-\frac{1}{4\left(\frac{w_0^2}{1+{L_R}^2/z^2}+\sigma_c^2\right)}\left[\frac{{r_2}^2}{\left(1+iz/L_R\right)^2}+\frac{{r_1}^2}{\left(1-iz/L_R\right)^2}\right]\right\}. \qquad (6.6)
\end{aligned}
$$

After rearrangement, we obtain Eq.(3.12) of the mian text,

$$
\begin{aligned}
W\left(\mathbf{r}_1,\mathbf{r}_2,z\right) \propto &\frac{e^{im(\phi_2-\phi_1)}}{(1+z^2/L_d^2)}\exp\left[\frac{i(r_2^2-r_1^2)}{2(\sigma_c^2L_R/z+w_0^2z/L_R)}\right]\exp\left[-\frac{(r_1^2+r_2^2)}{4\sigma_c^2(1+z^2/L_d^2)}\right] \\
&\exp\left[-\frac{(r_1^2+r_2^2)}{2w_0^2(1+z^2/L_R^2)(1+z^2/L_d^2)}\right]I_m\left[\frac{r_1r_2}{2\sigma_c^2(1+z^2/L_d^2)}\right]. \qquad (6.7)
\end{aligned}
$$

Appendix C Copyright Permissions

Aug, 22,2024

Dear AIP Publishing,

I am preparing my PhD thesis for submission to the Faculty of Graduate Studies at Dalhousie University, Halifax, Nova Scotia, Canada. I am seeking your permission to include a manuscript version of the following papers as a chapter in the thesis:

1. Deep learning and random light structuring ensure robust free-space communications, Xiaofei Li, Yu Wang, Xin Liu, Yuan Ma, Yangjian Cai, Sergey A. Ponomarenko and Xianlong Liu, Applied Physics Letters 124 (21), 214103 (2024).

2. Prime number factorization with light beams carrying orbital angular momentum, Xiaofei Li, Xin Liu, Quanying Wu, Jun Zeng, Yangjian Cai, Sergey A. Ponomarenko and Chunhao Liang, APL Photonics 9(4), 046107 (2024).

Dalhousie graduate theses are collected and stored online by Dalhousie University and Library and Archives of Canada. I am seeking your permission for the material described above to be stored online in Dalhousie Universitys institutional repository and in Library and Archives of Canada (LAC)s Theses Canada Collection.

Full publication details and a copy of this permission letter will be included in the thesis.

Yours sincerely,

Xiaofei Li

From: AIPRights Permissions ⟨Rights@aip.org⟩

Sent: Thursday, August 22, 2024 4:28 PM

To: Xiaofei Li ⟨XiaofeiLi@dal.ca⟩

Subject: RE: Permission for using published papers in PhD thesis

Dear Dr. Li,

Thank you for reaching out to AIP Publishing with your reproduction request. We are delighted to be able to assist!

You are permitted to include all or part of your published articles in your thesis, provided you also include a credit line referencing the original publication.

Our preferred format is (please fill in the citation information): Reproduced from [FULL CITATION], with the permission of AIP Publishing.

If the thesis will be available electronically, please include a link to the version of record on AIP Publishings site.

Please let us know if you have any questions. Congratulations on the completion of your thesis and your degree!

Sincerely,

Suzanne Inge

Aug, 22,2024

Dear Optica,

I am preparing my PhD thesis for submission to the Faculty of Graduate Studies at Dalhousie University, Halifax, Nova Scotia, Canada. I am seeking your permission to include a manuscript version of the following paper as a chapter in the thesis:

Perfect correlation vortices, Xiaofei Li, Sajjad Bashiri, Yuan Ma, Chuanhao Liang, Yangjian Cai, Sergey A. Ponomarenko and Zhiheng Xu, Optics Letters 49(16), 4717-4720 (2024).

Dalhousie graduate theses are collected and stored online by Dalhousie University and Library and Archives of Canada. I am seeking your permission for the material described above to be stored online in Dalhousie Universitys institutional repository and in Library and Archives of Canada (LAC)s Theses Canada Collection.

Full publication details and a copy of this permission letter will be included in the thesis.

Yours sincerely,

Xiaofei Li

From: Optica Publishing Group Copyright ⟨copyright@optica.org⟩

Sent: Friday, August 23, 2024 2:04 PM

To: Xiaofei Li ⟨XiaofeiLi@dal.ca⟩

Subject: RE: Permission for using a published paper in PhD thesis 2723

Dear Xiaofei Li,

Thank you for contacting Optica Publishing Group.

For the use of material from Xiaofei Li, Sajjad Bashiri, Yuan Ma, Chunhao Liang,

Yangjian Cai, Sergey A. Ponomarenko, and Zhiheng Xu, "Perfect correlation vortices," Opt. Lett. 49, 4717-4720 (2024):

Because you are the author of the source paper from which you wish to reproduce material, Optica Publishing Group considers your requested use of its copyrighted materials to be permissible within the author rights granted in the Copyright Transfer Agreement submitted by the requester on acceptance for publication of his/her manuscript. If the entire article is being included, it is requested that the Author Accepted Manuscript (or preprint) version be the version included within the thesis and any archives and that a complete citation of the original material be included in any publication. This permission assumes that the material was not reproduced from another source when published in the original publication.

The Author Accepted Manuscript version is the preprint version of the article that was accepted for publication but not yet prepared and/or formatted by Optica Publishing Group or its vendors.

While your publisher should be able to provide additional guidance, we prefer the below citation formats:

For citations in figure captions:

[Reprinted/Adapted] with permission from [ref #] ©Optical Society of America [or Optica Publishing Group. (Please include the full citation in your reference list)

Please let me know if you have any questions.

Kind Regards,

Cassie Travers

Cassie Travers

23 August 2024

Authorized Agent, Optica Publishing Group

Bibliography

[1] Tongyi Huang, Wu Yang, Jun Wu, Jin Ma, Xiaofei Zhang, and Daoyin Zhang. A survey on green 6g network: Architecture and technologies. *IEEE Access*, 7:175758–175768, 2019.

[2] Darui Jin, Ying Chen, Yi Lu, Junzhang Chen, Peng Wang, Zichao Liu, Sheng Guo, and Xiangzhi Bai. Neutralizing the impact of atmospheric turbulence on complex scene imaging via deep learning. *Nature Machine Intelligence*, 3(10):876–884, 2021.

[3] Xiaodong Duan, Xiaoyun Wang, Lu Lu, Nanxiang Shi, Chao Liu, Tong Zhang, and Tao Sun. 6g architecture design: from overall, logical and networking perspective. *IEEE Communications Magazine*, 61(7):158–164, 2023.

[4] Murat Yücel and Muharrem Açikgöz. Optical communication infrastructure in new generation mobile networks. *Fiber and Integrated Optics*, 42(2):53–92, 2023.

[5] Vasyl Molebny, Paul McManamon, Ove Steinvall, Takao Kobayashi, and Weibiao Chen. Laser radar: historical prospectivefrom the east to the west. *Optical Engineering*, 56(3):031220–031220, 2017.

[6] Maarten Uijt de Haag, Don Venable, and Mark Smearcheck. Use of 3d laser radar for navigation of unmanned aerial and ground vehicles in urban and indoor environments. In *Laser Radar Technology and Applications XII*, volume 6550, pages 95–106. SPIE, 2007.

[7] Glauber Mosqueira, J Apetz, Kleber Roberto Da Silva Santos, Emilia Villani, Ricardo Suterio, and Lus Gonzaga Trabasso. Analysis of the indoor gps system as feedback for the robotic alignment of fuselages using laser radar measurements as comparison. *Robotics and Computer-Integrated Manufacturing*, 28(6):700–709, 2012.

[8] Dong Shen, Yuhang Xu, and Yakun Huang. Research on 2d-slam of indoor mobile robot based on laser radar. In *Proceedings of the 2019 4th International Conference on Automation, Control and Robotics Engineering*, pages 1–7, 2019.

[9] Seongwook Lee, Song-Yi Kwon, Bong-Jun Kim, Hae-Seung Lim, and Jae-Eun Lee. Dual-mode radar sensor for indoor environment mapping. *Sensors*, 21(7):2469, 2021.

[10] Christoph Froehlich, Markus Mettenleiter, and F Haertl. Imaging laser radar for high-speed monitoring of the environment. In *Intelligent Transportation Systems*, volume 3207, pages 50–64. SPIE, 1998.

[11] Chunhe Yu and Danping Zhang. Road curbs detection based on laser radar. In *2006 8th International Conference on Signal Processing*, volume 4. IEEE, 2006.

[12] Julian Ryde and Nick Hillier. Performance of laser and radar ranging devices in adverse environmental conditions. *Journal of Field Robotics*, 26(9):712–727, 2009.

[13] Junxuan Zhao, Hao Xu, Hongchao Liu, Jianqing Wu, Yichen Zheng, and Dayong Wu. Detection and tracking of pedestrians and vehicles using roadside lidar sensors. *Transportation Research part C: Emerging Technologies*, 100:68–87, 2019.

[14] Douglas L McMakin, David M Sheen, Thomas E Hall, Mike O Kennedy, and Harlen P Foote. Biometric identification using holographic radar imaging techniques. In *Sensors, and Command, Control, Communications, and Intelligence (C3I) Technologies for Homeland Security and Homeland Defense VI*, volume 6538, pages 80–91. SPIE, 2007.

[15] Dusan Kocur, Maria Svecova, and Jakub Demcak. Estimation of breathing frequency and heart rate by biometric uwb radar. In *2018 IEEE International Conference on Systems, Man, and Cybernetics (SMC)*, pages 2570–2576. IEEE, 2018.

[16] Aditya Singh Rathore, Zhengxiong Li, Weijin Zhu, Zhanpeng Jin, and Wenyao Xu. A survey on heart biometrics. *ACM Computing Surveys (CSUR)*, 53(6):1–38, 2020.

[17] TH Kim. Analysis of optical communications, fiber optics, sensors and laser applications. *Journal of Machine and Computing*, 3(2):115–125, 2023.

[18] Saleha Al-Zhrani, Nada M Bedaiwi, Intesar F El-Ramli, Abeer Z Barasheed, Ali Abduldaiem, Yas Al-Hadeethi, and Ahmad Umar. Underwater optical communications: A brief overview and recent developments. *Engineered Science*, 16:146–186, 2021.

[19] Shuai Cao, Xiangning Chen, and Benchi Yuan. Overview of short-range wireless communication protocol. In *2022 7th International Conference on Computer and Communication Systems (ICCCS)*, pages 519–523. IEEE, 2022.

[20] Fernando P Guiomar, Marco A Fernandes, José Leonardo Nascimento, Vera Rodrigues, and Paulo P Monteiro. Coherent free-space optical communications: opportunities and challenges. *Journal of Lightwave Technology*, 40(10):3173–3186, 2022.

[21] Abu Jahid, Mohammed H Alsharif, and Trevor J Hall. A contemporary survey on free space optical communication: Potentials, technical challenges, recent advances and research direction. *Journal of Network and Computer Applications*, 200:103311, 2022.

[22] William J Buchanan, Shancang Li, and Rameez Asif. Lightweight cryptography methods. *Journal of Cyber Security Technology*, 1(3-4):187–201, 2017.

[23] Ramesh Yegireddi and R Kiran Kumar. A survey on conventional encryption algorithms of cryptography. In *2016 International Conference on ICT in Business Industry & Government (ICTBIG)*, pages 1–4. IEEE, 2016.

[24] Stefano Pirandola, Ulrik L Andersen, Leonardo Banchi, Mario Berta, Darius Bunandar, Roger Colbeck, Dirk Englund, Tobias Gehring, Cosmo Lupo, Carlo Ottaviani, et al. Advances in quantum cryptography. *Advances in Optics and Photonics*, 12(4):1012–1236, 2020.

[25] Peter W Shor and John Preskill. Simple proof of security of the bb84 quantum key distribution protocol. *Physical Review Letters*, 85(2):441, 2000.

[26] Miralem Mehic, Libor Michalek, Emir Dervisevic, Patrik Burdiak, Matej Plakalovic, Jan Rozhon, Nerman Mahovac, Filip Richter, Enio Kaljic, Filip Lauterbach, et al. Quantum cryptography in 5g networks: a comprehensive overview. *IEEE Communications Surveys & Tutorials*, 2023.

[27] Chao He, Yijie Shen, and Andrew Forbes. Towards higher-dimensional structured light. *Light: Science & Applications*, 11(1):205, 2022.

[28] Yiyan Wu and William Y Zou. Orthogonal frequency division multiplexing: A multi-carrier modulation scheme. *IEEE Transactions on Consumer Electronics*, 41(3):392–399, 1995.

[29] Joseph Y N Hui. Pattern code modulation and optical decoding-a novel code-division multiplexing technique for multifiber networks. *IEEE Journal on Selected Areas in Communications*, 3(6):916–927, 1985.

[30] Evgenii Krouk and Sergei Semenov. *Modulation and coding techniques in wireless communications*. John Wiley & Sons, 2011.

[31] Syed Alwee Aljunid, Mahamod Ismail, Abd Rahman Ramli, Borhanuddin Mohd Ali, and Mohamad Khazani Abdullah. A new family of optical code sequences for spectral-amplitude-coding optical cdma systems. *IEEE Photonics Technology Letters*, 16(10):2383–2385, 2004.

[32] René L Eriksen, Paul C Mogensen, and Jesper Glückstad. Elliptical polarisation encoding in two dimensions using phase-only spatial light modulators. *Optics Communications*, 187(4-6):325–336, 2001.

[33] Chaoran Huang, Dongliang Wang, Weipeng Zhang, Benshan Wang, Alexander N Tait, Thomas Ferreira De Lima, Bhavin J Shastri, and Paul R Prucnal. High-capacity space-division multiplexing communications with silicon photonic blind source separation. *Journal of Lightwave Technology*, 40(6):1617–1632, 2022.

[34] Stanislav A Derevyanko and Jaroslaw E Prilepsky. Channel model for the dual-polarization b-modulated nonlinear frequency-division multiplexing optical transmission systems. *Optics Express*, 31(12):19686–19702, 2023.

[35] Zhengyang Duan, Hang Chen, and Xing Lin. Optical multi-task learning using multi-wavelength diffractive deep neural networks. *Nanophotonics*, 12(5):893–903, 2023.

[36] Daniel JF Barros, Sarah K Wilson, and Joseph M Kahn. Comparison of orthogonal frequency-division multiplexing and pulse-amplitude modulation in indoor optical wireless links. *IEEE Transactions on Communications*, 60(1):153–163, 2011.

[37] Dany-Sebastien Ly-Gagnon, Satoshi Tsukamoto, Kazuhiro Katoh, and Kazuro Kikuchi. Coherent detection of optical quadrature phase-shift keying signals with carrier phase estimation. *Journal of Lightwave Technology*, 24(1):12, 2006.

[38] Brian Stern, Haoshuo Chen, Kwangwoong Kim, and Nicolas K Fontaine. Large dispersion silicon bragg grating for full-field 40-gbd qpsk phase retrieval receiver. *Journal of Lightwave Technology*, 40(22):7358–7363, 2022.

[39] Kang Liu, Yongqiang Cheng, Zhaocheng Yang, Hongqiang Wang, Yuliang Qin, and Xiang Li. Orbital-angular-momentum-based electromagnetic vortex imaging. *IEEE Antennas and Wireless Propagation Letters*, 14:711–714, 2014.

[40] Jianqiu Wang, Kang Liu, Yongqiang Cheng, and Hongqiang Wang. Vortex sar imaging method based on oam beams design. *IEEE Sensors Journal*, 19(24):11873–11879, 2019.

[41] Alan E Willner, Hao Huang, Yan Yan, Yongxiong Ren, Nisar Ahmed, Goudong Xie, Changjing Bao, L Li, Y Cao, Z Zhao, et al. Optical communications using orbital angular momentum beams. *Advances in Optics and Photonics*, 7(1):66–106, 2015.

[42] Alan E Willner, Kai Pang, Hao Song, Kaiheng Zou, and Huibin Zhou. Orbital angular momentum of light for communications. *Applied Physics Reviews*, 8(4), 2021.

[43] Jian Wang, Jun Liu, Shuhui Li, Yifan Zhao, Jing Du, and Long Zhu. Orbital angular momentum and beyond in free-space optical communications. *Nanophotonics*, 11(4):645–680, 2022.

[44] Hugo Larocque, Jérémie Gagnon-Bischoff, Dominic Mortimer, Yingwen Zhang, Frédéric Bouchard, Jeremy Upham, Vincenzo Grillo, Robert W Boyd, and Ebrahim Karimi. Generalized optical angular momentum sorter and its application to high-dimensional quantum cryptography. *Optics express*, 25(17):19832–19843, 2017.

[45] Xinyuan Fang, Haoran Ren, and Min Gu. Orbital angular momentum holography for high-security encryption. *Nature Photonics*, 14(2):102–108, 2020.

[46] Rina Zazkis and Stephen Campbell. Prime decomposition: Understanding uniqueness. *The Journal of Mathematical Behavior*, 15(2):207–218, 1996.

[47] Xinhua Peng, Zeyang Liao, Nanyang Xu, Gan Qin, Xianyi Zhou, Dieter Suter, and Jiangfeng Du. Quantum adiabatic algorithm for factorization and its experimental implementation. *Physical Review Letters*, 101(22):220405, 2008.

[48] Eric Anschuetz, Jonathan Olson, Alán Aspuru-Guzik, and Yudong Cao. Variational quantum factoring. In *Quantum Technology and Optimization Problems: First International Workshop, QTOP 2019, Munich, Germany, March 18, 2019, Proceedings 1*, pages 74–85. Springer, 2019.

[49] Xin Liu, Chunhao Liang, Yangjian Cai, and Sergey A Ponomarenko. Axial correlation revivals and number factorization with structured random waves. *Physical Review Applied*, 20(2):L021004, 2023.

[50] Mark Sadgrove, Sanjay Kumar, and Kenichi Nakagawa. Enhanced factoring with a bose-einstein condensate. *Physical Review Letters*, 101(18):180502, 2008.

[51] Michael Mehring, Klaus Müller, Ilya Sh Averbukh, Wolfgang Merkel, and Wolfgang P Schleich. Nmr experiment factors numbers with gauss sums. *Physical Review Letters*, 98(12):120502, 2007.

[52] Michael Gilowski, Thijs Wendrich, T Müller, Ch Jentsch, Wolfgang Ertmer, EM Rasel, and Wolfgang P Schleich. Gauss sum factorization with cold atoms. *Physical Review Letters*, 100(3):030201, 2008.

[53] Damien Bigourd, Béatrice Chatel, Wolfgang P Schleich, and Bertrand Girard. Factorization of numbers with the temporal talbot effect: Optical implementation by a sequence of shaped ultrashort pulses. *arXiv preprint arXiv:0709.1906*, 2007.

[54] Ziyi Zhu, Molly Janasik, Alexander Fyffe, Darrick Hay, Yiyu Zhou, Brian Kantor, Taylor Winder, Robert W Boyd, Gerd Leuchs, and Zhimin Shi. Compensation-free high-dimensional free-space optical communication using turbulence-resilient vector beams. *Nature Communications*, 12(1):1666, 2021.

[55] Lei Gong, Qian Zhao, Hao Zhang, Xin-Yao Hu, Kun Huang, Jia-Miao Yang, and Yin-Mei Li. Optical orbital-angular-momentum-multiplexed data transmission under high scattering. *Light: Science & Applications*, 8(1):27, 2019.

[56] Mario Krenn, Johannes Handsteiner, Matthias Fink, Robert Fickler, Rupert Ursin, Mehul Malik, and Anton Zeilinger. Twisted light transmission over 143 km. *Proceedings of the National Academy of Sciences*, 113(48):13648–13653, 2016.

[57] Shuhui Li and Jian Wang. Adaptive free-space optical communications through turbulence using self-healing bessel beams. *Scientific Reports*, 7(1):43233, 2017.

[58] Guoxuan Zhu, Yuanhui Wen, Xiong Wu, Yujie Chen, Jie Liu, and Siyuan Yu. Obstacle evasion in free-space optical communications utilizing airy beams. *Optics Letters*, 43(6):1203–1206, 2018.

[59] Antonio García-Zambrana, Carmen Castillo-Vázquez, and Beatriz Castillo-Vázquez. Outage performance of mimo fso links over strong turbulence and misalignment fading channels. *Optics Express*, 19(14):13480–13496, 2011.

[60] Leonard Mandel and Emil Wolf. *Optical coherence and quantum optics*. Cambridge university press, 1995.

[61] Leonard Mandel and Emil Wolf. Spectral coherence and the concept of cross-spectral purity. *Journal of the Optical Society of America*, 66(6):529–535, 1976.

[62] Emil Wolf. *Introduction to the Theory of Coherence and Polarization of Light*. Cambridge university press, 2007.

[63] Sergey A Ponomarenko and Emil Wolf. Coherence properties of light in young's interference pattern formed with partially coherent light. *Optics Communications*, 170(1-3):1–8, 1999.

[64] Edward Collett and Emil Wolf. Is complete spatial coherence necessary for the generation of highly directional light beams? *Optics Letters*, 2(2):27–29, 1978.

[65] Franco Gori. Collett-wolf sources and multimode lasers. *Optics Communications*, 34(3):301–305, 1980.

[66] Emil Wolf and Edward Collett. Partially coherent sources which produce the same far-field intensity distribution as a laser. *Optics Communications*, 25(3):293–296, 1978.

[67] Yangjian Cai, Yahong Chen, Jiayi Yu, Xianlong Liu, and Lin Liu. Generation of partially coherent beams. *Progress in Optics*, 62:157–223, 2017.

[68] William H. Carter and Emil Wolf. Coherence and radiometry with quasihomogeneous planar sources. *Journal of the Optical Society of America*, 67(6):785–796, 1977.

[69] Franco Gori. Mode propagation of the field generated by collett-wolf schell-model sources. *Optics Communications*, 46(3-4):149–154, 1983.

[70] Pasi Vahimaa and Jari Turunen. Finite-elementary-source model for partially coherent radiation. *Optics Express*, 14(4):1376–1381, 2006.

[71] Sergey A Ponomarenko. Complex gaussian representation of statistical pulses. *Optics Express*, 19(18):17086–17091, 2011.

[72] Liyuan Ma and Sergey A Ponomarenko. Free-space propagation of optical coherence lattices and periodicity reciprocity. *Optics Express*, 23(2):1848–1856, 2015.

[73] Fang Wang, Yahong Chen, Lina Guo, Lin Liu, and Yangjian Cai. Complex gaussian representations of partially coherent beams with nonconventional degrees of coherence. *Journal of the Optical Society of America A*, 34(10):1824–1829, 2017.

[74] Franco Gori and Massimo Santarsiero. Devising genuine spatial correlation functions. *Optics Letters*, 32(24):3531–3533, 2007.

[75] Franco Gori, Massimo Santarsiero, Raja Simon, Gemma Piquero, Riccardo Borghi, and Giorgio Guattari. Coherent-mode decomposition of partially polarized, partially coherent sources. *Journal of the Optical Society of America A*, 20(1):78–84, 2003.

[76] Fei Wang, Shijun Zhu, and Yangjian Cai. Experimental study of the focusing properties of a gaussian schell-model vortex beam. *Optics Letters*, 36(16):3281–3283, 2011.

[77] Milo W Hyde IV, Santasri Bose-Pillai, David G Voelz, and Xifeng Xiao. Generation of vector partially coherent optical sources using phase-only spatial light modulators. *Physical Review Applied*, 6(6):064030, 2016.

[78] Benjamin Perez-Garcia, Adad Yepiz, Raul I Hernandez-Aranda, Andrew Forbes, and Grover A Swartzlander. Digital generation of partially coherent vortex beams. *Optics Letters*, 41(15):3471–3474, 2016.

[79] Xinlei Zhu, Fei Wang, Chengliang Zhao, Yangjian Cai, and Sergey A Ponomarenko. Experimental realization of dark and antidark diffraction-free beams. *Optics Letters*, 44(9):2260–2263, 2019.

[80] Xianlong Liu, Fei Wang, Lin Liu, Yahong Chen, Yangjian Cai, and Sergey A Ponomarenko. Complex degree of coherence measurement for classical statistical fields. *Optics Letters*, 42(1):77–80, 2017.

[81] Zhaofeng Huang, Yahong Chen, Fei Wang, Sergey A Ponomarenko, and Yangjian Cai. Measuring complex degree of coherence of random light fields with generalized hanbury brown–twiss experiment. *Physical Review Applied*, 13(4):044042, 2020.

[82] David Voelz, Xifeng Xiao, and Olga Korotkova. Numerical modeling of schell-model beams with arbitrary far-field patterns. *Optics Letters*, 40(3):352–355, 2015.

[83] Chunhao Liang, Raha Khosravi, Xiaoxiong Liang, Barbora Kacerovská, and Yashar E Monfared. Standard and elegant higher-order laguerre–gaussian correlated schell-model beams. *Journal of Optics*, 21(8):085607, 2019.

[84] Yahong Chen, Fei Wang, Chengliang Zhao, and Yangjian Cai. Experimental demonstration of a laguerre-gaussian correlated schell-model vortex beam. *Optics Express*, 22(5):5826–5838, 2014.

[85] Fei Wang, Chunhao Liang, Yangsheng Yuan, and Yangjian Cai. Generalized multi-gaussian correlated schell-model beam: from theory to experiment. *Optics Express*, 22(19):23456–23464, 2014.

[86] Hanna Lajunen and Toni Saastamoinen. Propagation characteristics of partially coherent beams with spatially varying correlations. *Optics Letters*, 36(20):4104–4106, 2011.

[87] Liyuan Ma and Sergey A Ponomarenko. Optical coherence gratings and lattices. *Optics Letters*, 39(23):6656–6659, 2014.

[88] Chunhao Liang, Xinlei Zhu, Chenkun Mi, Xiaofeng Peng, Fei Wang, Yangjian Cai, and Sergey A Ponomarenko. High-quality partially coherent bessel beam array generation. *Optics Letters*, 43(13):3188–3191, 2018.

[89] Yahong Chen, Andreas Norrman, Sergey A Ponomarenko, and Ari T Friberg. Coherence lattices in surface plasmon polariton fields. *Optics Letters*, 43(14):3429–3432, 2018.

[90] Chunhao Liang, Xin Liu, Zhiheng Xu, Fei Wang, Wei Wen, Sergey A Ponomarenko, Yangjian Cai, and Pujuan Ma. Perfect optical coherence lattices. *Applied Physics Letters*, 119(13), 2021.

[91] Yahong Chen, Sergey A Ponomarenko, and Yangjian Cai. Experimental generation of optical coherence lattices. *Applied Physics Letters*, 109(6), 2016.

[92] Fei Wang, Xianlong Liu, and Yangjian Cai. Propagation of partially coherent beam in turbulent atmosphere: a review (invited review). *Progress In Electromagnetics Research*, 150:123–143, 2015.

[93] Xianlong Liu, Jiayi Yu, Yangjian Cai, and Sergey A Ponomarenko. Propagation of optical coherence lattices in the turbulent atmosphere. *Optics Letters*, 41(18):4182–4185, 2016.

[94] Sergey A Ponomarenko, Weihong Huang, and Michael Cada. Dark and antidark diffraction-free beams. *Optics Letters*, 32(17):2508–2510, 2007.

[95] Zhiheng Xu, Xin Liu, Yangjian Cai, Sergey A Ponomarenko, and Chunhao Liang. Structurally stable beams in the turbulent atmosphere: dark and antidark beams on incoherent background. *Journal of the Optical Society of America A*, 39(12):C51–C57, 2022.

[96] Fei Wang, Yahong Chen, Xianlong Liu, Yangjian Cai, and Sergey A Ponomarenko. Self-reconstruction of partially coherent light beams scattered by opaque obstacles. *Optics Express*, 24(21):23735–23746, 2016.

[97] Zhiheng Xu, Xianlong Liu, Yahong Chen, Fei Wang, Lin Liu, Yashar E Monfared, Sergey A Ponomarenko, Yangjian Cai, and Chunhao Liang. Self-healing properties of hermite-gaussian correlated schell-model beams. *Optics Express*, 28(3):2828–2837, 2020.

[98] Yiming Dong, Yangjian Cai, Chengliang Zhao, and Min Yao. Statistics properties of a cylindrical vector partially coherent beam. *Optics Express*, 19(7):5979–5992, 2011.

[99] Miao Dong, ChengLiang Zhao, YangJian Cai, and YuanJie Yang. Partially coherent vortex beams: Fundamentals and applications. *Science China Physics, Mechanics & Astronomy*, 64(2):224201, 2021.

[100] Sergey A Ponomarenko. Twist phase and classical entanglement of partially coherent light. *Optics Letters*, 46(23):5958–5961, 2021.

[101] Gaofeng Wu and Yangjian Cai. Detection of a semirough target in turbulent atmosphere by a partially coherent beam. *Optics Letters*, 36(10):1939–1941, 2011.

[102] Jesse N Clark, Xiaojing Huang, Ross Harder, and Ian K Robinson. High-resolution three-dimensional partially coherent diffraction imaging. *Nature Communications*, 3(1):993, 2012.

[103] Chengliang Zhao and Yangjian Cai. Trapping two types of particles using a focused partially coherent elegant laguerre–gaussian beam. *Optics Letters*, 36(12):2251–2253, 2011.

[104] Deming Peng, Zhaofeng Huang, Yonglei Liu, Yahong Chen, Fei Wang, Sergey A Ponomarenko, and Yangjian Cai. Optical coherence encryption with structured random light. *PhotoniX*, 2:1–15, 2021.

[105] Zhi Zhou, Xu Chen, En Li, Liekang Zeng, Ke Luo, and Junshan Zhang. Edge intelligence: Paving the last mile of artificial intelligence with edge computing. *Proceedings of the IEEE*, 107(8):1738–1762, 2019.

[106] Ze Gao and Lin Lin. The intelligent integration of interactive installation art based on artificial intelligence and wireless network communication. *Wireless Communications and Mobile Computing*, 2021:1–12, 2021.

[107] Min Gu, Xiangping Li, and Yaoyu Cao. Optical storage arrays: a perspective for future big data storage. *Light: Science & Applications*, 3(5):e177–e177, 2014.

[108] Xu Ouyang, Yi Xu, Mincong Xian, Ziwei Feng, Linwei Zhu, Yaoyu Cao, Sheng Lan, Bai-Ou Guan, Cheng-Wei Qiu, Min Gu, et al. Synthetic helical dichroism for six-dimensional optical orbital angular momentum multiplexing. *Nature Photonics*, 15(12):901–907, 2021.

[109] Yoshitomo Okawachi, Bok Young Kim, Michal Lipson, and Alexander L Gaeta. Chip-scale frequency combs for data communications in computing systems. *Optica*, 10(8):977–995, 2023.

[110] Isaac Khader, Hugo Bergeron, Laura C Sinclair, William C Swann, Nathan R Newbury, and Jean-Daniel Deschênes. Time synchronization over a free-space optical communication channel. *Optica*, 5(12):1542–1548, 2018.

[111] Kaiheng Zou, Kai Pang, Hao Song, Jintao Fan, Zhe Zhao, Haoqian Song, Runzhou Zhang, Huibin Zhou, Amir Minoofar, Cong Liu, et al. High-capacity free-space optical communications using wavelength-and mode-division-multiplexing in the mid-infrared region. *Nature Communications*, 13(1):7662, 2022.

[112] Zhen Huang, Xiaohui Hu, Qinghua Li, Xiao Jin, Bing Xu, Deng Wang, Xuping Liu, Tingting Zhang, Zhenghe Zhang, Guodong Chen, et al. Phase-shifted quadrature-phase demodulation based on a multi-longitudinal mode laser self-mixing sensor for displacement measurement. *Measurement*, 206:112323, 2023.

[113] Alan E Willner and Cong Liu. Perspective on using multiple orbital-angular-momentum beams for enhanced capacity in free-space optical communication links. *Nanophotonics*, 10(1):225–233, 2020.

[114] Jianghao Li, Qi Yang, Xiaoxiao Dai, Christina Lim, and Ampalavanapillai Nirmalathas. Joint beam-and-probabilistic shaping scheme based on orbital angular momentum mode for indoor optical wireless communications. *Journal of Lightwave Technology*, 2023.

[115] Hui Cao, Allard Pieter Mosk, and Stefan Rotter. Shaping the propagation of light in complex media. *Nature Physics*, 18(9):994–1007, 2022.

[116] Zixuan Xu, Guanjun Xu, and Zhengqi Zheng. Ber and channel capacity performance of an fso communication system over atmospheric turbulence with different types of noise. *Sensors*, 21(10):3454, 2021.

[117] Hao Song, Runzhou Zhang, Huibin Zhou, Xinzhou Su, Kaiheng Zou, Yuxiang Duan, Narek Karapetyan, Haoqian Song, Kai Pang, Nanzhe Hu, et al. Turbulence-resilient pilot-assisted self-coherent free-space optical communications using a photodetector array for bandwidth enhancement. *Optics Letters*, 47(21):5723–5726, 2022.

[118] Masoud Ghalaii and Stefano Pirandola. Quantum communications in a moderate-to-strong turbulent space. *Communications Physics*, 5(1):38, 2022.

[119] Huibin Zhou, Xinzhou Su, Yuxiang Duan, Hao Song, Kaiheng Zou, Runzhou Zhang, Haoqian Song, Nanzhe Hu, Moshe Tur, and Alan E Willner. Atmospheric turbulence strength distribution along a propagation path probed by longitudinally structured optical beams. *Nature Communications*, 14(1):4701, 2023.

[120] Yijie Shen, Shankar Pidishety, Isaac Nape, and Angela Dudley. Self-healing of structured light: a review. *Journal of Optics*, 24(10):103001, 2022.

[121] Sergey A Ponomarenko and Emil Wolf. The spectral degree of coherence of fully spatially coherent electromagnetic beams. *Optics Communications*, 227(1-3):73–74, 2003.

[122] Wenwei Liu, Dina Ma, Zhancheng Li, Hua Cheng, Duk-Yong Choi, Jianguo Tian, and Shuqi Chen. Aberration-corrected three-dimensional positioning with a single-shot metalens array. *Optica*, 7(12):1706–1713, 2020.

[123] Geoffrey Hinton, Li Deng, Dong Yu, George E Dahl, Abdel-rahman Mohamed, Navdeep Jaitly, Andrew Senior, Vincent Vanhoucke, Patrick Nguyen, Tara N Sainath, et al. Deep neural networks for acoustic modeling in speech recognition: The shared views of four research groups. *IEEE Signal Processing Magazine*, 29(6):82–97, 2012.

[124] David Silver, Aja Huang, Chris J Maddison, Arthur Guez, Laurent Sifre, George Van Den Driessche, Julian Schrittwieser, Ioannis Antonoglou, Veda Panneershelvam, Marc Lanctot, et al. Mastering the game of go with deep neural networks and tree search. *Nature*, 529(7587):484–489, 2016.

[125] Wei Ma, Feng Cheng, and Yongmin Liu. Deep-learning-enabled on-demand design of chiral metamaterials. *ACS Nano*, 12(6):6326–6334, 2018.

[126] Zhaocheng Liu, Dayu Zhu, Sean P Rodrigues, Kyu-Tae Lee, and Wenshan Cai. Generative model for the inverse design of metasurfaces. *Nano Letters*, 18(10):6570–6576, 2018.

[127] Zhanwei Liu, Shuo Yan, Haigang Liu, and Xianfeng Chen. Superhigh-resolution recognition of optical vortex modes assisted by a deep-learning method. *Physical Review Letters*, 123(18):183902, 2019.

[128] Qian Zhang, Che Liu, Xiang Wan, Lei Zhang, Shuo Liu, Yan Yang, and Tie Jun Cui. Machine-learning designs of anisotropic digital coding metasurfaces. *Advanced Theory and Simulations*, 2(2):1800132, 2019.

[129] Alex Krizhevsky, Ilya Sutskever, and Geoffrey E Hinton. Imagenet classification with deep convolutional neural networks. *Advances in Neural Information Processing Systems*, 25, 2012.

[130] Kaiming He, Xiangyu Zhang, Shaoqing Ren, and Jian Sun. Deep residual learning for image recognition. In *Proceedings of The IEEE Conference on Computer Vision and Pattern Recognition*, pages 770–778, 2016.

[131] Franco Gori and Massimo Santarsiero. Devising genuine spatial correlation functions. *Optics Letters*, 32(24):3531–3533, 2007.

[132] Olga Russakovsky, Jia Deng, Hao Su, Jonathan Krause, Sanjeev Satheesh, Sean Ma, Zhiheng Huang, Andrej Karpathy, Aditya Khosla, Michael Bernstein, et al. Imagenet large scale visual recognition challenge. *International Journal of Computer Vision*, 115:211–252, 2015.

[133] Yuhao Chen, Shen Zhang, and Renjie Song. Scoring your prediction on unseen data. In *Proceedings of the IEEE/CVF Conference on Computer Vision and Pattern Recognition*, pages 3278–3287, 2023.

[134] Diederik P Kingma and Jimmy Ba. Adam: A method for stochastic optimization. *arXiv preprint arXiv:1412.6980*, 2014.

[135] Carmelo Rosales-Guzmán and Andrew Forbes. How to shape light with spatial light modulators. Society of Photo-Optical Instrumentation Engineers (SPIE), 2017.

[136] Carmelo Rosales-Guzmán, Nkosiphile Bhebhe, Nyiku Mahonisi, and Andrew Forbes. Multiplexing 200 spatial modes with a single hologram. *Journal of Optics*, 19(11):113501, 2017.

[137] Marat Samuil Soskin and Mikhail V Vasnetsov. Singular optics. In *Progress in Optics*, volume 42, pages 219–276. Elseveier, 2001.

[138] Mark R Dennis, Kevin O'holleran, and Miles J Padgett. Singular optics: optical vortices and polarization singularities. In *Progress in Optics*, volume 53, pages 293–363. Elsevier, 2009.

[139] Les Allen, Marco W Beijersbergen, RJC Spreeuw, and JP Woerdman. Orbital angular momentum of light and the transformation of laguerre-gaussian laser modes. *Physical Review A*, 45(11):8185, 1992.

[140] Alison M Yao and Miles J Padgett. Orbital angular momentum: origins, behavior and applications. *Advances in Optics and Photonics*, 3(2):161–204, 2011.

[141] Jian Wang, Jeng-Yuan Yang, Irfan M Fazal, Nisar Ahmed, Yan Yan, Hao Huang, Yongxiong Ren, Yang Yue, Samuel Dolinar, Moshe Tur, and Alan E Willner. Terabit free-space data transmission employing orbital angular momentum multiplexing. *Nature Photonics*, 6(7):488–496, 2012.

[142] Kevin T Gahagan and Grover A Swartzlander. Optical vortex trapping of particles. *Optics Letters*, 21(11):827–829, 1996.

[143] Jian Chen, Chenhao Wan, and Qiwen Zhan. Vectorial optical fields: recent advances and future prospects. *Science Bulletin*, 63(1):54–74, 2018.

[144] Jae Hoon Lee, Gregory Foo, Eric G Johnson, and Grover A Swartzlander Jr. Experimental verification of an optical vortex coronagraph. *Physical Review Letters*, 97(5):053901, 2006.

[145] Xiaofei Li, Xin Liu, Quanying Wu, Jun Zeng, Yangjian Cai, Sergey A Ponomarenko, and Chunhao Liang. Prime number factorization with light beams carrying orbital angular momentum. *APL Photonics*, 9(4), 2024.

[146] Ebrahim Karimi, Gianluigi Zito, Bruno Piccirillo, Lorenzo Marrucci, and Enrico Santamato. Hypergeometric-gaussian modes. *Optics Letters*, 32(21):3053–3055, 2007.

[147] Andrey S Ostrovsky, Carolina Rickenstorff-Parrao, and Víctor Arrizón. Generation of the perfect optical vortex using a liquid-crystal spatial light modulator. *Optics Letters*, 38(4):534–536, 2013.

[148] Joaquín García-García, Carolina Rickenstorff-Parrao, Rubén Ramos-García, Víctor Arrizón, and Andrey S Ostrovsky. Simple technique for generating the perfect optical vortex. *Optics Letters*, 39(18):5305–5308, 2014.

[149] Pravin Vaity and Leslie Rusch. Perfect vortex beam: Fourier transformation of a bessel beam. *Optics Letters*, 40(4):597–600, 2015.

[150] Jonathan Pinnell, Valeria Rodríguez-Fajardo, and Andrew Forbes. How perfect are perfect vortex beams? *Optics Letters*, 44(22):5614–5617, 2019.

[151] Sergey A Ponomarenko. A class of partially coherent beams carrying optical vortices. *Journal of the Optical Society of America A*, 18(1):150–156, 2001.

[152] Ivan D Maleev, David M Palacios, Arvind S Marathay, and Grover A Swartzlander Jr. Spatial correlation vortices in partially coherent light: theory. *Journal of the Optical Society of America B*, 21(11):1895–1900, 2004.

[153] Greg Gbur, Taco D Visser, and E Wolf. 'hidden' singularities in partially coherent wavefields. *Journal of Optics A: Pure and Applied Optics*, 6(5):S239, 2004.

[154] Galina V Bogatyryova, Christina V Felde, Peter V Polyanskii, Sergey A Ponomarenko, Marat S Soskin, and Emil Wolf. Partially coherent vortex beams with a separable phase. *Optics Letters*, 28(11):878–880, 2003.

[155] David M Palacios, David M Maleev, Arvind S Marathay, and Grover A Swartzlander Jr. Spatial correlation singularity of a vortex field. *Physical Review Letters*, 92(14):143905, 2004.

[156] Yahong Chen, Andreas Norrman, Sergey A Ponomarenko, and Ari T Friberg. Partially coherent surface plasmon polariton vortex fields. *Physical Review A*, 100(5):053833, 2019.

[157] Xiaofei Li, Huazhe Wei, Taco D Visser, Yangjian Cai, and Xianlong Liu. Partially coherent perfect vortex beam generated by an axicon phase. *Applied Physics Letters*, 119(17), 2021.

[158] Xianlong Liu, Yilin Wu, Kaiqi Zhu, Xiaofei Li, Yangjian Cai, and Yaru Gao. Perfect vortex beams with periodic coherence properties. *Journal of Applied Physics*, 135(16), 2024.

[159] Izrail Solomonovich Gradshteyn and Iosif Moiseevich Ryzhik. *Table of integrals, series, and products*. Academic press, 2014.

[160] Zhiheng Xu, Xiaofei Li, Xin Liu, Sergey A Ponomarenko, Yangjian Cai, and Chunhao Liang. Vortex preserving statistical optical beams. *Optics Express*, 28(6):8475–8483, 2020.

[161] Morteza Hajati, Vincent Sieben, and Sergey A Ponomarenko. Airy beams on incoherent background. *Optics Letters*, 46(16):3961–3964, 2021.

[162] Larry C Andrews and Ronald L Phillips. Laser beam propagation through random media. *Laser Beam Propagation Through Random Media: Second Edition*, 2005.

[163] Shinichi Tatsumi, Keiji Yamaguchi, and Naoyuki Furuya. Forestscanner: A mobile application for measuring and mapping trees with lidar-equipped iphone and ipad. *Methods in Ecology and Evolution*, 14(7):1603–1609, 2023.

[164] Wenjie Shen, Yanping Wang, Yun Lin, Yang Li, Wen Jiang, and Wen Hong. Range-doppler based moving target image trace analysis method in circular sar. *Remote Sensing*, 15(8):2073, 2023.

[165] Mark E Weber, John YN Cho, and Henry G Thomas. Command and control for multifunction phased array radar. *IEEE Transactions on Geoscience and Remote Sensing*, 55(10):5899–5912, 2017.

[166] Urs Germann, Marco Boscacci, Lorenzo Clementi, Marco Gabella, Alessandro Hering, Maurizio Sartori, Ioannis V Sideris, and Bertrand Calpini. Weather radar in complex orography. *Remote Sensing*, 14(3):503, 2022.

[167] Xiaosheng Zhang, Kyungmok Kwon, Johannes Henriksson, Jianheng Luo, and Ming C Wu. A large-scale microelectromechanical-systems-based silicon photonics lidar. *Nature*, 603(7900):253–258, 2022.

[168] Abraham Aidoo Borsah, Majid Nazeer, and Man Sing Wong. Lidar-based forest biomass remote sensing: A review of metrics, methods, and assessment criteria for the selection of allometric equations. *Forests*, 14(10):2095, 2023.

[169] Ienkaran Arasaratnam, Simon Haykin, Thiagalingam Kirubarajan, and Fred A Dilkes. Tracking the mode of operation of multi-function radars. In *2006 IEEE Conference on Radar*, pages 6–pp. IEEE, 2006.

[170] Alexander Charlish, Folker Hoffmann, Christoph Degen, and Isabel Schlangen. The development from adaptive to cognitive radar resource management. *IEEE Aerospace and Electronic Systems Magazine*, 35(6):8–19, 2020.

[171] Judson E Stailey and Kurt D Hondl. Multifunction phased array radar for aircraft and weather surveillance. *Proceedings of the IEEE*, 104(3):649–659, 2016.

[172] Peter John-Baptiste, Aaron Brandewie, Joe Vinci, Kristine Bell, Joel T Johnson, Christopher F Neese, and Muralidhar Rangaswamy. Multi-task tracking and classification with an adaptive radar. *IET Radar, Sonar & Navigation*, 16(4):692–703, 2022.

[173] Peng Zhang, Junkun Yan, Wenqiang Pu, Hongwei Liu, and Maria S Greco. Multi-dimensional resource management scheme for multiple target tracking under dynamic electromagnetic environment. *IEEE Transactions on Signal Processing*, 2024.

[174] Junyu Lin, Jun Hu, Zhiyuan Xie, Yulan Zhang, Guangjia Huang, and Zengping Chen. A multitask network for people counting, motion recognition, and localization using through-wall radar. *Sensors*, 23(19):8147, 2023.

[175] Junxuan Zhao, Hao Xu, Hongchao Liu, Jianqing Wu, Yichen Zheng, and Dayong Wu. Detection and tracking of pedestrians and vehicles using roadside lidar sensors. *Transportation research part C: emerging technologies*, 100:68–87, 2019.

[176] Bo Tang and Petre Stoica. Mimo multifunction rf systems: Detection performance and waveform design. *IEEE Transactions on Signal Processing*, 70:4381–4394, 2022.

[177] Zishi Zhang, Ye Yuan, Wei Yi, and Junkun Yan. Quality of service-based multitask scheduling for cooperative multi-radar systems. In *2023 12th International Conference on Control, Automation and Information Sciences (ICCAIS)*, pages 477–482. IEEE, 2023.

[178] Rongrong Mao, Kang Liu, Hongyan Liu, Yang Yang, and Huaitie Xiao. Electromagnetic vortex imaging based on oam multiplexing beam with orthogonal polyphase coding. *IEEE Sensors Journal*, 2023.

[179] Caipin Li, Shengyuan Li, Dong You, Wencan Peng, Jinwei Li, Yu Li, Qiang Li, and Zhanye Chen. Targets'radial and tangential velocities estimation based on vortex electromagnetic waves. *Remote Sensing*, 14(16):3861, 2022.

[180] Jia Liang, Qun Zhang, Ying Luo, Hang Yuan, and Yijun Chen. Three-dimensional imaging with bistatic vortex electromagnetic wave radar. *Remote Sensing*, 14(13):2972, 2022.

[181] Ting Jiang, Jun Hu, Siqi Luo, Ying Wang, and Wen Wu. A fast and super-resolution method of vortex-based imaging. *IEEE Antennas and Wireless Propagation Letters*, 2023.

[182] Joseph W Goodman. *Introduction to Fourier optics*. Roberts and Company publishers, 2005.

[183] Pinliang Dong and Qi Chen. *LiDAR remote sensing and applications*. CRC Press, 2017.

[184] Zahra Gharineiat, Fayez Tarsha Kurdi, and Glenn Campbell. Review of automatic processing of topography and surface feature identification lidar data using machine learning techniques. *Remote Sensing*, 14(19):4685, 2022.

[185] Les Allen, Marco W Beijersbergen, RJC Spreeuw, and JP Woerdman. Orbital angular momentum of light and the transformation of laguerre-gaussian laser modes. *Physical Review A*, 45(11):8185, 1992.

[186] Yijie Shen, Xuejiao Wang, Zhenwei Xie, Changjun Min, Xing Fu, Qiang Liu, Mali Gong, and Xiaocong Yuan. Optical vortices 30 years on: Oam manipulation from topological charge to multiple singularities. *Light: Science & Applications*, 8(1):90, 2019.

[187] Hao He, Marlies EJ Friese, Norman R Heckenberg, and Halin Rubinsztein-Dunlop. Direct observation of transfer of angular momentum to absorptive particles from a laser beam with a phase singularity. *Physical Review Letters*, 75(5):826, 1995.

[188] Hugo Larocque, Alessio DErrico, Manuel F Ferrer-Garcia, Avishy Carmi, Eliahu Cohen, and Ebrahim Karimi. Optical framed knots as information carriers. *Nature Communications*, 11(1):5119, 2020.

[189] Ling-Jun Kong, Weixuan Zhang, Peng Li, Xuyue Guo, Jingfeng Zhang, Furong Zhang, Jianlin Zhao, and Xiangdong Zhang. High capacity topological coding based on nested vortex knots and links. *Nature Communications*, 13(1):2705, 2022.

[190] Jian Wang, Jeng-Yuan Yang, Irfan M Fazal, Nisar Ahmed, Yan Yan, Hao Huang, Yongxiong Ren, Yang Yue, Samuel Dolinar, Moshe Tur, et al. Terabit free-space data transmission employing orbital angular momentum multiplexing. *Nature Photonics*, 6(7):488–496, 2012.

[191] Julio T Barreiro, Tzu-Chieh Wei, and Paul G Kwiat. Beating the channel capacity limit for linear photonic superdense coding. *Nature Physics*, 4(4):282–286, 2008.

[192] Ling-Jun Kong, Yifan Sun, Furong Zhang, Jingfeng Zhang, and Xiangdong Zhang. High-dimensional entanglement-enabled holography. *Physical Review Letters*, 130(5):053602, 2023.

[193] Haoran Ren, Xinyuan Fang, Jaehyuck Jang, Johannes Bürger, Junsuk Rho, and Stefan A Maier. Complex-amplitude metasurface-based orbital angular momentum holography in momentum space. *Nature Nanotechnology*, 15(11):948–955, 2020.

[194] Giuseppe Mussardo, Andrea Trombettoni, and Zhao Zhang. Prime suspects in a quantum ladder. *Physical Review Letters*, 125(24):240603, 2020.

[195] Fabrizio Sgrignuoli, Sean Gorsky, Wesley A Britton, Ran Zhang, Francesco Riboli, and Luca Dal Negro. Multifractality of light in photonic arrays based on algebraic number theory. *Communications Physics*, 3(1):106, 2020.

[196] Han-Lin Li, Shu-Cherng Fang, Bertrand MT Lin, and Way Kuo. Unifying colors by primes. *Light: Science & Applications*, 12(1):32, 2023.

[197] Xing Lin, Yair Rivenson, Nezih T Yardimci, Muhammed Veli, Yi Luo, Mona Jarrahi, and Aydogan Ozcan. All-optical machine learning using diffractive deep neural networks. *Science*, 361(6406):1004–1008, 2018.

[198] Ronald L Rivest, Adi Shamir, and Leonard Adleman. A method for obtaining digital signatures and public-key cryptosystems. *Communications of the ACM*, 21(2):120–126, 1978.

[199] Lieven MK Vandersypen, Matthias Steffen, Gregory Breyta, Costantino S Yannoni, Mark H Sherwood, and Isaac L Chuang. Experimental realization of shor's quantum factoring algorithm using nuclear magnetic resonance. *Nature*, 414(6866):883–887, 2001.

[200] Karl Pelka, Jasmin Graf, Thomas Mehringer, and Joachim von Zanthier. Prime number decomposition using the talbot effect. *Optics Express*, 26(12):15009–15014, 2018.

[201] Martin Štefaňák, Wolfgang Merkel, Wolfgang P Schleich, Daniel Haase, and Helmut Maier. Factorization with gauss sums: scaling properties of ghost factors. *New Journal of Physics*, 9(10):370, 2007.

[202] Xin Liu, Yashar E Monfared, Ruixuan Pan, Pujuan Ma, Yangjian Cai, and Chunhao Liang. Experimental realization of scalar and vector perfect laguerre–gaussian beams. *Applied Physics Letters*, 119(2), 2021.

[203] Xin Liu, Qian Chen, Jun Zeng, Yangjian Cai, and Chunhao Liang. Measurement of optical coherence structures of random optical fields using generalized arago spot experiment. *Opto-Electronic Science*, 2(2):220024–1, 2023.

[204] Xiaofei Li, Liqi Ma, Jun Zeng, Zhen Dong, Lin Liu, Fei Wang, Bernhard J Hoenders, Yangjian Cai, and Xianlong Liu. Determining the topological charge of an obstructed vortex beam via reconstructed phase distribution. *Applied Physics Letters*, 117(25), 2020.

[205] Izrail Solomonovich Gradshteyn and Iosif Moiseevich Ryzhik. *Table of integrals, series, and products*. Academic press, 2014.